CHANGES IN ATMOSPHERIC CIRCULATION OVER GREENLAND, 1900–2014: EFFECTS ON SURFACE ENERGY BALANCE AND SURFACE MASS BALANCE

by

JOSHUA JOSEPH ROSEN

(Under the Direction of Thomas L. Mote)

ABSTRACT

The early 21st Century has been characterized by numerous climatic extremes on the Greenland Ice Sheet, with new records set for melt extent and negative surface mass balance. At the same time, the atmospheric circulation over Greenland during the melt season has been characterized by an anomalously high frequency of blocking patterns. Using data from the 20th Century Reanalysis (20CRv2c), and regional climate model Modèle Atmosphérique Régional, a summer 500 hPa geopotential height climatology is constructed for the years 1900–2014, using self-organizing maps to examine the linkage between atmospheric circulation and both surface energy and surface mass balance. Results show statistically significant increases in synoptic types that favor meltwater production when comparing the 20th and 21st centuries. The Arctic warm period of the early 20th Century is also examined, with results showing statistically significant increases in synoptic types favoring meltwater production when comparing the 1920s to the 1930s.

INDEX WORDS: Greenland, Climate change, Synoptic climatology, Regional climate modeling, Arctic climate, Self-organizing maps

CHANGES IN ATMOSPHERIC CIRCULATION OVER GREENLAND, 1900–2014: EFFECTS ON SURFACE ENERGY BALANCE AND SURFACE MASS BALANCE

by

JOSHUA JOSEPH ROSEN

B.S., Brevard College, 2007

A Thesis Submitted to the Graduate Faculty of The University of Georgia in Partial Fulfillment of the Requirements for the Degree

MASTER OF SCIENCE

ATHENS, GEORGIA

2017

CHANGES IN ATMOSPHERIC CIRCULATION OVER GREENLAND, 1900-2014: EFFECTS ON SURFACE ENERGY BALANCE AND SURFACE MASS BALANCE

by

JOSHUA JOSEPH ROSEN

Major Professor:	Thomas L. Mote
Committee:	Andrew J. Grundstein
	Åsa K. Rennermalm

Electronic Version Approved:

Suzanne Barbour
Dean of the Graduate School
The University of Georgia
May 2017

ACKNOWLEDGEMENTS

I would, first and foremost, like to thank Dr. Thomas Mote for his guidance and assistance during my time as a graduate student, and especially in the construction of this thesis. I would also like to thank Dr. Andrew Grundstein and Dr. Åsa Rennermalm for their very helpful feedback and assistance in the creation of this thesis. I am also grateful to Dr. Xavier Fettweis for providing both daily MAR output and guidance on how to utilize it. Thanks also to Dr. Craig Ramseyer, for his assistance with the self-organizing map methodology and MATLAB scripting, as well as Kyle Mattingly and Paul Miller, for their help with Python coding and reanalysis data. I am also grateful to Dr. Todd Rasmussen for teaching me MATLAB, as well as the staff of the Geography Department, for their help and encouragement. Thanks also to Dr. Richard Milligan, who encouraged me to pursue graduate education at UGA. Lastly, I would like to thank my parents, without whose help, encouragement, and love this thesis would not have been possible.

This project was funded by the NASA Interdisciplinary Research in Earth Science (IDS) program, Grant Number NNX14AD98G. Support for the Twentieth Century Reanalysis Project version 2c dataset is provided by the U.S. Department of Energy, Office of Science, Biological and Environmental Research (BER), and by the National Oceanic and Atmospheric Administration Climate Program Office.

TABLE OF CONTENTS

Page

LIST OF TABLES

Page

LIST OF FIGURES

Page

CHAPTER 1

INTRODUCTION

As knowledge of global climate change continues to advance, one of the most critical areas of research is the rapidly changing state of the Earth's cryosphere. Both the Greenland Ice Sheet (GrIS) and the Antarctic Ice Sheet are of paramount importance, as the fate of these ice sheets holds the key to both the rate and magnitude of future sea level rise. The GrIS alone holds approximately 2.96 million km^3 of ice, enough to raise global sea level by 7.36 m [*Bamber et al.*, 2013]. While sea level rise is perhaps the best known impact from climate change in Greenland, impacts from increasing GrIS melt extend to the strength of the thermohaline circulation and changes to the planet's radiation balance [*Schuenemann et al.*, 2009].

Perhaps nothing underscored the importance of the GrIS to the future of the global climate as the 2012 GrIS melt season, when the ice sheet experienced the most dramatic and important melting event since 1889 [*Nghiem et al., 2012*]. After the highest point on the GrIS, Summit, reached the unusually high temperature of 2.2°C on 11 July 2012 [*Hanna et al.*, 2014], melt was detected across 98.6% of the GrIS on 12 July 2012 [*Nghiem et al.*, 2012]. The melt extent and probable melt extent detected on 12 July 2012 is depicted in Figure 1.1. The melt season of 2012 went on to set numerous records for melt extent, melt length, negative surface mass balance (SMB), mass loss, runoff, low albedo values, and bare ice extent, as described by *Tedesco et al.* [2013].

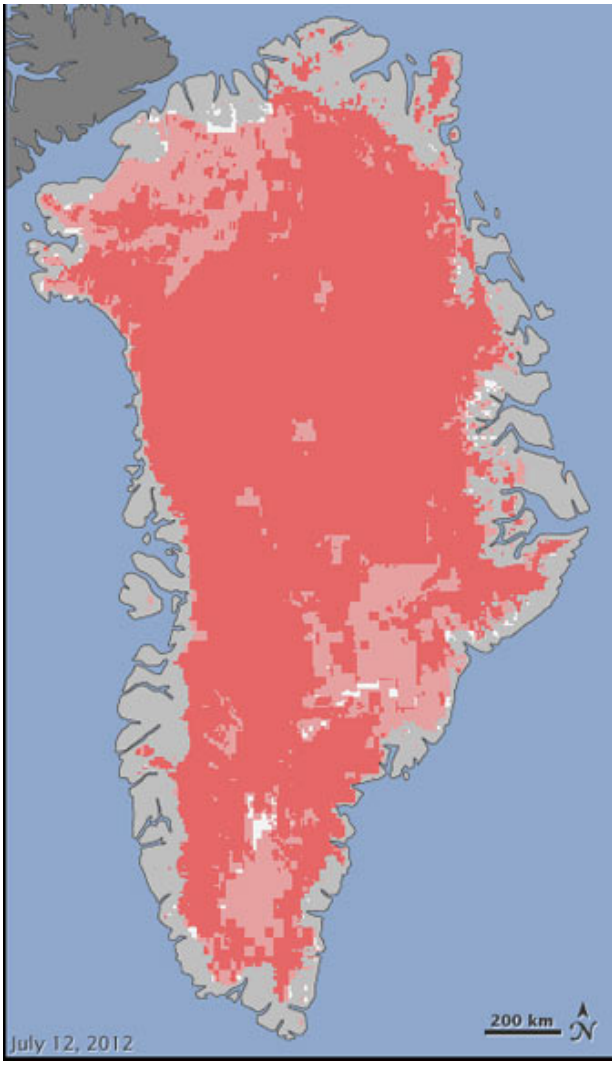

Figure 1.1. Areas of melt (pink) and probable melt (light pink) for 12 July 2012, modified from [*Nghiem et al.*, 2012].

However, the 2012 melt season was only the latest in a series of extremes, with 2007 and 2010 having previously set melt extent records [*Mote*, 2007; *Box et al.*, 2011]. While negative SMB and ice discharge previously contributed equally to the downward trend in GrIS mass balance [*van den Broeke et* al., 2009], more recent studies [*Rignot et al.*, 2011; *Andersen et al.*, 2014; *Enderlin et al.*, 2014; *Kjeldsen et al.*, 2015; *van den Broeke et al.*, 2016] have shown that negative SMB now accounts for most GrIS mass loss. At the same time, the atmospheric circulation over Greenland has seen drastic

changes since the 1990s, with greatly increased values of the Greenland Blocking Index (GBI) [*Hanna et al.*, 2016]. In addition, the early 21st Century has seen an increasing frequency of extended duration blocking events accompanied by anomalously high GBI values [*McLeod and Mote*, 2016].

Given the major climatic changes seen in Greenland during the 21st Century, as well as the importance of sea level rise to the future of both natural and human systems across the globe [*Hauer et al.*, 2016], it is critical to develop a better understanding of the linkage between atmospheric circulation and both the surface energy balance and surface mass balance of the Greenland Ice Sheet. The atmospheric circulation ultimately controls the surface energy balance of the ice sheet, which in turn determines the surface temperature and melt occurrence [*Rennermalm et al.*, 2013; *Tedesco et al.*, 2016a]. Such a linkage can be established using a synoptic climatological analysis, which seeks to classify atmospheric conditions into representative "types" and then examine the environmental conditions typical of each type, allowing the underlying principles governing the linked atmosphere-land surface system to emerge [*Cassano et al.*, 2007; *Sheridan and Lee*, 2011].

While numerous studies of Greenland synoptic climatology [*Mote*, 1998a; *Mote*, 1998b; *Schuenemann and Cassano*, 2009, 2010; *Schuenemann et al.*, 2009; *Fettweis et al.*, 2011a; *Fettweis et al.*, 2013; *Mattingly et al.*, 2016; *Mioduszewski et al.*, 2016] have examined the recent warm period and/or the latter half of the 20th Century, only one previous study [*Belleflamme et al*., 2015] has looked further back to the warm period of the early 20th Century. This period, described by *Bengtsson et al.* [2004] as "most spectacular climate events of the twentieth century", saw temperatures in southern

Greenland like those of the more recent warm period [*Hanna et al.*, 2007], with annual temperatures anomalies greater than two standard deviations above a 1951–1980 mean, similar to the more recent warm period [*Box et al.*, 2009]. While the forcing behind this warming is poorly understood [*Hanna et al.*, 2013], some have suggested this warming was the result of a "large but random climate excursion" [*Wood and Overland*, 2010]. While this period was previously difficult to study due to a lack of reanalysis datasets, two newer reanalysis datasets, the 20th Century Reanalysis, version 2 (20CRv2) [*Compo et al.*, 2011], with data back to 1871, and the ERA-20C Reanalysis [*Poli et al.,* 2016], with data back to 1900, have since been used by *Belleflamme et al.* [2015] to develop a summer (June, July, August, or JJA) circulation type classification for the Arctic Ocean, Greenland, and portions of the north Atlantic for the years 1871–2014.

This research seeks to build on the work of *Belleflamme et al.* [2015] by classifying the summer atmospheric circulation near Greenland, from the early 20th Century to the present, into representative synoptic types, and subsequently examining how each identified synoptic type affects the surface energy and mass balance variables of the GrIS. In doing so, it seeks to answer the following:

- What are the different synoptic types seen over the Greenland Ice Sheet and the surrounding oceans in the summer months (JJA) for 1900–2014?
- Does the atmospheric circulation associated with certain synoptic types modify the surface energy balance of the GrIS in such a way that results in greater mass losses with these synoptic types than others?
- Are there statistically significant changes in synoptic type frequency during 1900–2014?

To answer these questions, a synoptic climatology of 500 hPa geopotential heights was constructed for a spatial domain centered on Greenland using data from the 20th Century Reanalysis, version 2c (20CRv2c) [*Compo et al.*, 2011, 2015]. The climatology was constructed using self-organizing maps (SOMs), a machine learning method that has been used previously in Greenland [*Schuenemann and Cassano*, 2009, 2010; *Schuenemann et al.*, 2009; *Mattingly et al.*, 2016; *Mioduszewski et al.*, 2016]. The SOM methodology has advantages over more traditional methods, such as Principal Component Analysis (PCA)/Empirical Orthogonal Function (EOF), in pattern extraction accuracy, frequency assignment accuracy, and physical interpretability [*Reusch et al.*, 2005; *Liu et al.*, 2006]. Data from the regional climate model Modèle Atmosphérique Régional (MAR), forced by data from 20CRv2c, were used to examine values of key surface energy balance and surface mass balance variables associated with each synoptic type. Finally, a statistical analysis was performed to examine whether changes in the frequency of each synoptic type were statistically significant. This research should improve understanding of variability in summer atmospheric circulation over Greenland, as well as provide a better understanding of the relations between different circulation patterns and the resulting conditions observed on the GrIS. Lastly, this research should also provide a better understanding of the circulation patterns associated with the early 20th Century warm period.

CHAPTER 2

BACKGROUND

This chapter examines previous research into Greenland's climate during the 19th, 20th and early 21st centuries. It first puts the current climate in perspective by examining Greenland temperature reconstructions and the insight they give on past climate fluctuations. The discussion then shifts to examine trends in summer melt extent, GrIS mass balance, and the surface mass balance component of the mass budget. The surface energy budget of the GrIS and its crucial role in controlling the surface mass balance is discussed, with the following sections examining atmospheric circulation, synoptic climatology, and lastly, the use of the SOM in synoptic climatology.

2.1 Greenland Temperature Records

The Greenland temperature record can be reconstructed from meteorological station records and reanalysis datasets, as done by *Hanna et al.* [2007] for the summer season (JJA) for the period 1958–2006. No correlation was found between northern hemisphere summer temperature and southern Greenland coastal temperatures from the 1960s to the early 1990s [*Hanna et al.*, 2007]. The mid 1990s onward, however, saw a positive correlation between these two temperature records [*Hanna et al.*, 2007]. At the same time, a negative correlation between the summer phase of the North Atlantic Oscillation (NAO) and southern Greenland temperatures is no longer present after the mid-1990s [*Hanna et al.*, 2007].

Along Greenland's southern coast, the warm temperatures found during the 1930s and 1940s were like those of the late 1990s forward, and, as *Hanna et al*. [2007] speculates, they may have produced similar amounts of melt and runoff. However, this early 20th Century warming was confined to higher latitudes of the northern hemisphere, while the more recent warming has been global, leading the authors to conclude the recent warming in Greenland is likely due to anthropogenic global warming [*Hanna et al.*, 2007].

A more complete reconstruction of near-surface air temperatures in Greenland, using a combination of regional climate modeling and records from meteorological stations, was performed by *Box et al.* [2009] for the period 1840–2007. Warming during the period 1919–32 was found to be 33% greater than the warming that took place from 1994–2007. This study was later expanded upon by *Box* [2013] for the period 1840–2010. Over the course of the study period, surface meltwater production increased by 59%, along with increases in melt rate and bare ice area, in concert with increasing surface temperature. A comparison of temperatures between the *Box et al.* [2009] and *Box* [2013] reconstructions can be seen in Figure 2.1.

While Greenland air temperatures have risen in recent years, records from several coastal Greenland meteorological stations show a period of raising mean annual air temperatures (MAAT) spanning the 1890s to the mid 1930s, along with an increasing rate of warm extreme events over this same period [*Mernild et al.*, 2014]. This trend reversed from the mid 1930s to the mid 1980s, with decreasing MAAT and an increasing number

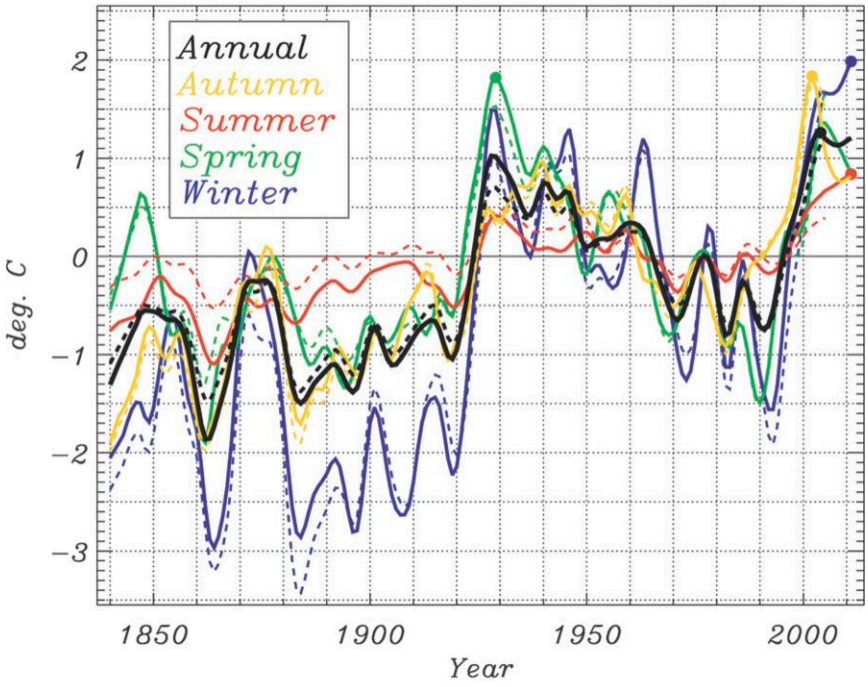

Figure 2.1. Greenland Ice Sheet surface air temperature anomalies for annual and seasonal periods, 1840–2010. All anomalies are relative to a 1951–1980 base period. Solid lines are data from *Box* [2013]; dashed lines are data from *Box et al.* [2009]. Circles indicate the warmest 13-year Gaussian-averaged year in each respective time series. Figure from *Box* [2013].

of cold extremes, before reversing yet again in the mid 1980s, with a return to the warm conditions of the early 20th Century [*Mernild et al.*, 2014]. A negative correlation was seen between the NAO and extreme MAAT values; negative NAO values were linked to periods of warm extremes, while positive NAO values were linked to cold extremes [*Mernild et al.*, 2014]. More warm extremes were found in the 2000s than any other decade, with the 1940s having the second highest number of warm extremes [*Mernild et al.*, 2014].

2.2 Melt Extent

Changes in the surface energy balance of the GrIS over the past 20 years have led to higher temperatures and a drastic increase in surface melt extent; *Fettweis et al.* [2011b] found that the surface melt extent in the years 1998, 2003, 2005, and 2007 was "unprecedented in the last 50 years"; these extreme years saw a melt area twice as extensive as that observed during the 1980s. The year 2007, in particular, showed extensive melt extent, eclipsing the previous melt extent record set in 1998, with several locations in southern Greenland showing much earlier melt onset and duration [*Mote*, 2007]. The record melt of 2007, however, was soon eclipsed by 2010 [*Box et al.*, 2011] and 2012 [*Tedesco et al.*, 2013].

To examine melt extent changes over a longer time period, *Mernild et al.* [2011] used SnowModel, a spatially-distributed snow evolution modeling system forced with observed meteorological data, to simulate Greenland ice sheet melt extent during the pre-satellite era from 1960–1979. The simulated melt extent was found to have decreased by an average of 6% over the period 1960–1972, with three fewer days, on average, of a melt extent > 10% of the area of the ice sheet. The year with the lowest melt extent during 1960–2010, 1972, had a maximum simulated surface melt extent, of only 17%, with an average simulated melt extent of 7% [*Mernild et al.*, 2011]. In contrast, melt extent from 1979–2010, (from satellite microwave brightness measurements) increased by 27% over the period 1979 to 2010 [*Mernild et al.*, 2011].

More recently, the 2015 melt season was also notable, as the observed melt extent (52%) was the largest since the record 2012 season, exceeding the 39% melt extent observed in 2014; the 2015 melt extent was also more than two standard deviations above

the 1981–2010 mean [*Tedesco et al.*, 2016b]. In addition, the 2015 melt extent was also notable in that the southwestern and southeastern regions of the ice sheet saw a normal or below-normal number of days with melt, while northwestern, western, and northeastern regions saw an above-normal number of days with melt [*Tedesco et al.*, 2016b]. The circulation anomalies associated with the above-normal melt in the north are discussed further in section 2.6

2.3 Greenland Mass Balance

While increasing Greenland near-surface air temperatures and record surface melt extents provide valuable information about the changing state of the GrIS, a more complete understanding of the changes in the GrIS can be found by assessing changes in the ice sheet's mass balance. Mass balance (MB) is the change in ice sheet mass over time (dM/dt), which itself is determined by the difference between surface mass balance (SMB), and ice discharge (D) [*Van den Broeke et al*., 2016]:

$$MB = \frac{dM}{dt} = SMB - D \tag{2.1}$$

The SMB term may be either positive or negative, depending on its input terms [*Khan et al.*, 2015]. The input terms are total precipitative flux (a combination of rainfall and snowfall, P_{tot}), total sublimation (SU_{tot}), snow erosion by divergence of drifting snow transport (ER_{ds}), and meltwater runoff (RU) [*Van den Broeke et al*., 2016]:

$$SMB = P_{tot} - SU_{tot} - ER_{ds} - RU \tag{2.2}$$

In determining GrIS mass balance, SMB is usually reconstructed via the use of regional climate models [*Khan et al.*, 2015], while ice discharge requires measurements of both ice sheet thickness and velocity, which are obtained using such tools as airborne radar sounders (thickness) and synthetic aperture radars (SARs) (velocity) [*Bamber et al.*, 2013; *Khan et al.*, 2015].

Changes in the mass balance of the GrIS, due to both ice discharge and surface processes, can be measured with data from the Gravity Recovery and Climate Experiment (GRACE) satellites [*Khan et al.*, 2015]. This pair of satellites, flying approximately 220 km apart in a near-polar orbit, detects changes in the terrestrial gravity field (and thus mass) by measuring changes in the range between the two satellites. Because GRACE data is a measure of total mass loss, a regional climate model (RCM), such as MAR, is needed to help partition mass loss into its surface and discharge components [*Rennermalm et al.*, 2013].

While the SMB component and the dynamic component of mass balance are often considered separately, it is important to note that the surface runoff component of SMB can affect the dynamic mass loss component. Based on measurements performed at the Swiss Camp meteorological station (located in west-central Greenland, near the equilibrium line), *Zwally et al.* [2002] found that increases in meltwater production were correlated with faster ice velocity, as measured, likely due to increased basal lubrication as meltwater reaches the interface between the ice sheet and the underlying bedrock, resulting in increased basal sliding. However, more recent work has shown that over the course of the melt season a channelized subglacial drainage system may develop,

resulting in more efficient transport of meltwater and decreased basal sliding, as discussed by *Rennermalm et al*. [2013] and *Chu* [2014].

In addition, *Box and Colgan* [2013], in a study of the relation between surface meltwater runoff and marine ice loss (a combination of underwater glacial melting and iceberg calving), find that that the majority (>80%) of variability in marine ice loss can be explained by variability in meltwater runoff, with a doubling of meltwater runoff estimated to produce a fivefold increase in marine ice loss [*Box and Colgan*, 2013]. Thus, increasing mass loss from one of the components of surface mass balance (meltwater runoff) may in turn lead to increased mass loss from dynamic processes [*Mernild et al.*, 2011].

The mass balance of the GrIS has also seen drastic changes in recent years, with a downward trend since the year 2000 [*van den Broeke et al.*, 2009]. Combining ice flux data with surface mass balance output from the Regional Atmospheric Climate Model (RACMO2/GR) regional climate model, *van den Broeke et al.* [2009] constructed a GRACE-validated time series of GrIS mass balance, finding that atmospheric warming had resulted in both increased runoff and increased ice discharge. Ice dynamics and surface mass balance contributed equally to the resulting negative mass balance trend, with a total mass loss of ~1500 Gt (0.46 mm sea level rise/year) from 2000–2008 [*van den Broeke et al.*, 2009]. From 2006-2008, the melt rate increased to 273 Gt per year (0.75 mm sea level rise/year) [*van den Broeke et al.*, 2009].

Further evidence of the negative trend in GrIS mass balance was demonstrated by *Rignot et al.* [2011], who modeled surface mass balance with regional climate model RACMO2 (forced at the lateral boundaries by ERA-Interim, [*Dee et al*., 2011]), and

estimated ice discharge from synthetic aperture radar (SAR) (ice velocity) and radar sounder measurements (ice thickness). *Rignot et al.* [2011] found an acceleration in mass loss of 21.9 ± 1 Gt yr^{-2} over the 1992–2009 period; this figure was then validated with monthly GRACE data for the period common between the two data sets (2002–2009); the estimated mass losses from each independent method were found to be comparable [*Rignot et al.*, 2011]. Most importantly, *Rignot et al*. [2011] demonstrated that increasing runoff in the early 21st Century now results in most GrIS mass loss coming from surface processes.

The increasing dominance of the surface mass balance term in the GrIS mass balance is further demonstrated by *Enderlin et al.* [2014]. Combining a discharge time series with output from the RACMO2/GR regional climate model, *Enderlin et al.* [2014] found that ice discharge's contribution to mass loss diminished from 58% (pre-2005) to only 32% in the years 2009–2012. Most notably, increased mass loss since the year 2009 is dominated by the surface mass balance component; surface runoff was responsible for 84% of the increase [*Enderlin et al.*, 2014]. Total mass loss in the period 2000–2012 was estimated at 2963 ± 335 Gt [*Enderlin et al.*, 2014]. These trends are depicted in Figure 2.2.

The growing importance of surface runoff was also shown by *Andersen et al.* [2014], who used InSAR ice velocity measurements, aerial ice thickness measurements, and regional climate model MAR (forced with data from both ERA-40 [*Uppala et al.*, 2005] and ERA-Interim) to examine changes in ice sheet mass balance over the period 2007–2011, finding a total mass balance of -262 ± 21 Gt yr^{-1}. Interestingly, the majority of the mass loss (61%) was found to come from western Greenland, with loss from

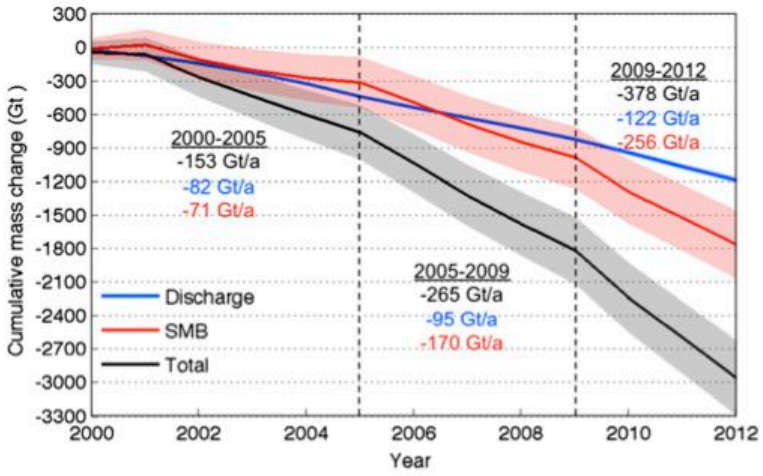

Figure 2.2. Changes in components of GrIS mass balance since the year 2000. Changes in discharge are relative to 1996, while SMB is relative to the 1961–1990 mean. Shading indicates uncertainty in the measurement. Figure from *Enderlin et al.* [2014].

marine-terminating glaciers dominant in the northwest, and runoff losses dominating in the southwest [*Andersen et al.*, 2014]. *Andersen et al.* [2014] also partitioned the mass loss from major GrIS drainage basins into surface mass balance loss and discharge components for 12 of 18 major drainage basins, finding that surface mass balance accounted for the majority (61%) of mass loss.

Further evidence of an accelerating trend in GrIS mass loss comes from *Kjeldsen et al.* [2015], who found that the mass loss rate for 2003–2010, 186.4 (±18.9) Gt yr^{-1}, was much greater than both 1900–1983 (75.1 (±29.5) Gt yr^{-1}) or 1983–2003 (73.8 (±40.5) Gt yr^{-1}). Like the studies mentioned previously, *Kjeldsen et al.* [2015] finds that the SMB term has recently become the dominant form of mass loss, with a steep drop since 2003, while finding a more constant dynamic ice loss term over the period of the study.

Lastly, a recent study of GrIS mass balance by *van den Broeke et al.* [2016] finds much of the same trend as those studies mentioned previously. Using updated discharge

data from *Enderlin et al.* [2014] (GRACE-validated for the common period 2002–2015), and SMB simulations from the regional climate model RACMO2.3 (forced with a combination of ERA-40 and ERA-Interim), *van den Broeke et al.* [2016] find surface mass balance for the period 1961–1990 to be near balance, with major changes during the period 1991–2015; the trend in meltwater production rises from 433 (±68) Gt yr^{-1} for 1961–1990 to 581 (±145) Gt yr^{-1} for 1991–2015. Similarly, runoff rises from 256 (±51) Gt yr^{-1} (1961–1990) to 363 (±102) Gt yr^{-1} (1991–2015) [*van den Broeke et al.*, 2016]. However, SMB itself displays much interannual variability due to variation in its various sub-components [*van den Broeke et al.*, 2016]. More broadly, mass balance was found to be increasingly negative since the mid-1990s, with a mass loss trend of -16.8 (±2.8) Gt yr^{-1} for the period 1991–2015 [*van den Broeke et al.*, 2016]. Like previous studies, surface mass balance was found to be the dominant mass loss term accounting for 61% of total mass loss since 1991 [*van den Broeke et al.*, 2016].

2.4 Greenland Surface Mass Balance

Given that several studies [*Rignot et al.*, 2011; *Enderlin et al.*, 2014; *Andersen et al.*, 2014; *Kjeldsen et al.*, 2015; *van den Broeke et al.*, 2016], show the dominance of the SMB term in the mass balance equation, a better understanding of SMB, which has been increasingly negative in recent years [*Shepherd et al.*, 2012; *Csatho et al.*, 2014], is critical. As described above and in the following section, use of a regional climate model to model SMB allows one to see how the individual components of SMB have changed over time and contribute to mass loss.

Hanna et al. [2005], using a combination of the ERA-40 reanalysis, European Centre for Medium-Range Weather Forecasts (ECMWF) operational forecast data, and the positive degree-day runoff/retention model of *Janssens and Huybrechts* [2000], found that changes in surface air temperature and precipitation caused a change in SMB, with runoff increasing from 264 (±26) km^3 (1961–1990) to 372 (±37) km^3 (1998–2003). Further work by *Fettweis* [2007] using regional climate model MAR (forced by ERA-40 and ECMWF operational analyses) for the period 1979–2006 showed an increase in both meltwater runoff and snow accumulation, along with a warming of 2.4°C over the period of study. The increase in accumulation, however, was not sufficient to balance the increased meltwater production, resulting in a net loss of 7.2 ± 5.1 km^3 of ice per year [*Fettweis*, 2007].

A longer reconstruction of GrIS SMB (1870–2010), performed by *Hanna et al.* [2011], again used the runoff/retention model of *Janssens and Huybrechts* [2000]. *Hanna et al.* [2011] combined gridded near-surface air temperature (SAT) data, precipitation, and surface latent heat flux from several different reanalysis data sets (20CRv1 [*Compo et al.*, 2011], ERA-40, and ECMWF operational analysis) with detailed SAT data from weather stations (Danish Meteorological Institute (DMI), Greenland Climate Network (GC-Net), Thule Airbase) to serve as model input. *Hanna et al.* [2011] showed that a combination of low runoff and high precipitation resulted in high GrIS SMB during the early portion of the 1920s. However, a subsequent decrease in precipitation and an increase in runoff, caused by higher temperatures, resulted in a major decrease in GrIS SMB from the mid-1920s to the mid-1930s, a period co-incident with the 1930s "Greenland warm spell" [*Box et al.*, 2002, *Hanna et al.*, 2011]. Temperature data from

this reconstruction is depicted in Figure 2.3. More recently, *Hanna et al.* [2011] noted a decrease in GrIS SMB, beginning in the 1990s and accelerating after the year 2000. The SMB trends found by *Hanna et al.* [2011] are depicted in Figure 2.4.

The *Hanna et al.* [2011] SMB reconstruction was later incorporated by *Box* [2013] into one of the longest SMB reconstructions yet performed, spanning the years 1840–2010 [*Box*, 2013]. In addition to the *Hanna et al.* [2011] reconstruction, *Box* incorporated the temperature reconstruction of *Box et al.* [2009], meteorological station records, and ice core data [*Box et al.*, 2013]. Accumulation records came from ice core data and the RACMO2 regional climate model; a positive degree day (PDD) approach was utilized for meltwater production. Over the period 1840–2010, *Box* [2013] found a 1.6°C increase in summer (JJA) temperatures, and an even larger 2.0°C increase in winter (DJF).

This warming climate resulted in a substantial increase (59%) in meltwater production over the 1840–2010 study period. However, due to both increasing melt and increasing accumulation over the GrIS, retention of meltwater in firn also increased by 51% [*Box*, 2013]. However, the increase in runoff was larger, at 63% [*Box*, 2013]. Although the amount of meltwater and runoff produced on the GrIS has increased dramatically since the mid-1800s, *Box* [2013] also showed that the surface mass balance is highly variable at decadal timescales, depending on anomalies in melt, accumulation,

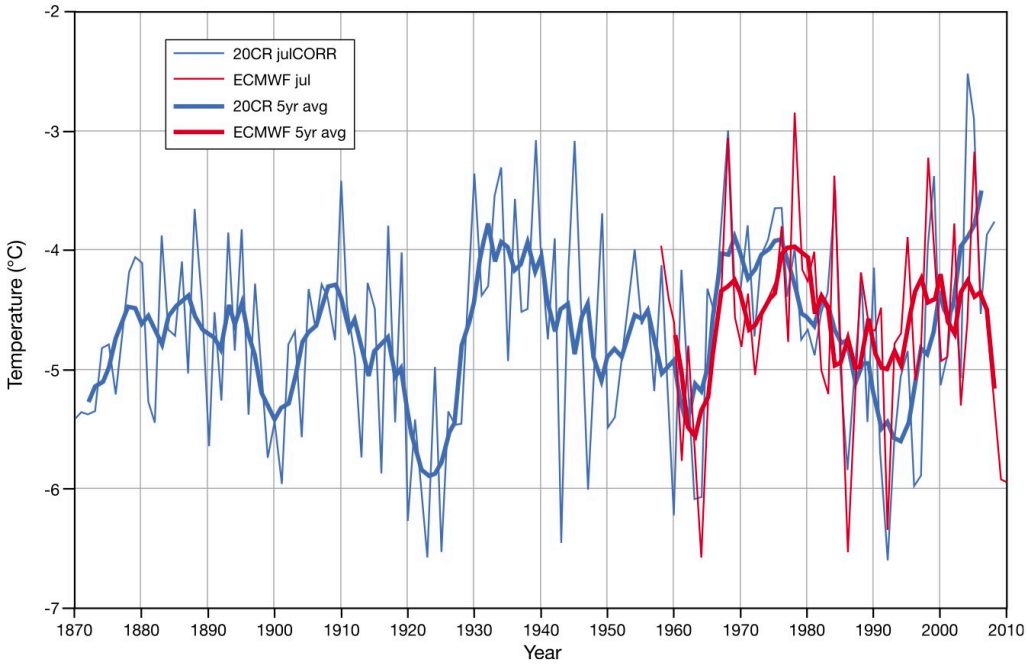

Figure 2.3. Time series of July 2-m temperatures and 5-year running means for the GrIS. Blue lines are data from the 20CR, while red lines are data from ERA-40 and ECMWF operational analyses. Thick lines represent 5-year running means, while thin lines represent data for the month of July. Temperatures were calibrated based on lapse rates derived from meteorological station data. Figure from *Hanna et al.* [2011].

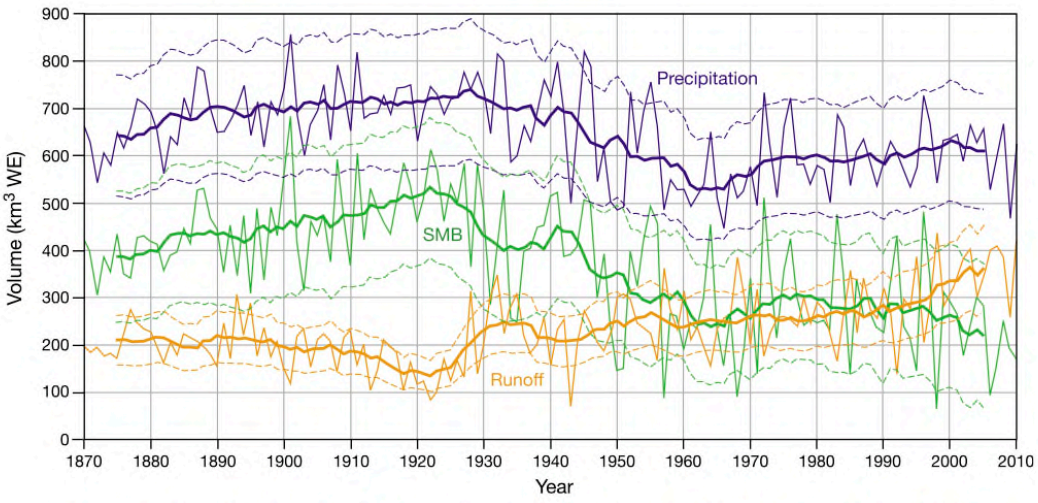

Figure 2.4. Changes in GrIS SMB, as well as changes in the accumulation (precipitation) and runoff terms for the period 1870–2010. Dashed lines indicate uncertainty, while bold lines are 11-year running means. Figure from *Hanna et al.* [2011].

or both [*Box*, 2013]. For example, the 1960s and 2000s were both periods characterized by negative SMB anomalies, but for different reasons (low accumulation and high melt, respectively), while the 1970s saw a combination of low melt and high accumulation that resulted in positive SMB anomalies [*Box*, 2013].

2.5 Surface Energy Balance

While the increasing meltwater production observed in recent years covaries with increasing surface air temperature on the GrIS [*Box*, 2013], the surface air temperature itself is determined by the surface energy balance (SEB), which consists of both radiative (net shortwave and net longwave radiation) and non-radiative (latent heat flux, sensible heat flux) terms [*Hartmann*, 1994]. Both the radiative and non-radiative terms are important to GrIS SEB, as demonstrated by the studies described below.

Neff et al. [2014], in an examination of the melt event of 11 July 2012, found that that the air mass over Summit Station on 11 July 2012 originated over the central and eastern portions of North America, which were experiencing record heat at the time. In addition, an examination of Special Sensor Microwave Imager (SSM/I) satellite data, combined with the ERA-Interim reanalysis, showed a long narrow band of high integrated water vapor (IWV) values, consistent with an atmospheric river (AR), approaching the western coast of Greenland prior to the 11 July 2012 [*Neff et al.*, 2014]. As this AR was traversing an anomalously warm north Atlantic, this likely has the effect of further enhancing the positive moisture anomalies in the air mass [*Neff et al.*, 2014]. The advection of this warm, moist airmass over the GrIS also took place during a shift in

the Arctic Oscillation (AO) from negative to positive values, which, as *Neff et al.* [2014] suggest, may allow for short-lived warm air advection events into the Arctic.

The warm, moist airmass described by *Neff et al.* [2014] likely had important effects on the surface energy budget; according to *Bennartz et al.* [2013], low-level liquid clouds present in this air mass were of sufficient optical thickness to enhance downwelling longwave radiation, but not so optically thick as to block downwelling shortwave radiation and prevent the surface temperature from rising. This balance between cloud reflectivity in the shortwave band and the amount of radiation emitted in the longwave band depends strongly on liquid water path (g m^{-2}), with values lower than 10 g m^{-2} or higher than 40 g m^{-2} resulting in surface temperatures staying below 0°C, with no surface melt as a result [*Bennartz et al.*, 2013].

In addition to the role of radiative fluxes discussed by *Bennartz et al.* [2013], non-radiative fluxes (latent heat, sensible heat, rain, and subsurface fluxes) also play an important role in the GrIS surface energy balance and thus the magnitude of melt that occurs. *Fausto et al.* [2016] examined two separate multi-day episodes of extreme melt during July 2012, the first being 8–11 July (termed "Episode 1") and 27–28 July (termed "Episode 2") using a one-dimensional surface energy balance model (driven by meteorological observations from automated weather stations utilized by the Programme for Monitoring of the Greenland Ice Sheet (PROMICE), as well as the regional climate model HIRHAM5).

Interestingly, both models showed that most of the energy available for melt in southeastern Greenland and eastern Greenland came from radiative fluxes, while non-radiative fluxes dominated in western and southern portions of Greenland, which the

authors attribute to the western portion of the ice sheet being the main recipient of the warm, moist advection described by *Neff et al.* [2014] [*Fausto et al.*, 2016]. Thus, on a single day, a weather pattern may result in the SEB in one region of the GrIS being quite different than another region. Importantly, the authors also note that both models used underestimate ablation due to an underestimation of non-radiative fluxes, with important consequences, such as producing artificially low estimates of melt for extreme events, with subsequent error in sea-level rise projections [*Fausto et al.*, 2016].

A better understanding of Greenland surface energy balance is important, as increasing temperatures expected during the 21st Century from anthropogenic climate forcing will lead to higher concentrations of lower tropospheric water vapor due to a rise in saturation vapor pressure, per the Clausis-Clapeyron relation [*Held and Soden*, 2006]. With this increase in atmospheric moisture, an increase in poleward moisture transport, and by extension, poleward latent heat flux should be expected [*Held and Soden*, 2006].

Indeed, studies of horizontal water vapor transport over the course of the 21st Century performed by *Lavers et al.* [2015], found that two different emissions scenarios or representative concentration pathways (RCP), RCP 4.5 and RCP 8.5, both show statistically significant increases in integrated vapor transport (IVT) across the seas and oceans surrounding Greenland during the summer months (JJA), with the more extreme scenario (RCP 8.5) also showing statistically significant increases across Greenland itself [*Lavers et al.*, 2015]. Most notably, the Arctic had the greatest increases in mean IVT of any region on Earth [*Lavers et al.*, 2015].

Moisture transport into the Arctic has already been shown to have important implications for surface energy budget over the Arctic Ocean, according to a recent study

of Arctic sea ice melt onset timing performed by *Mortin et al.* [2016]. Years with an early spring melt onset were found to have positive downward longwave radiation anomalies caused by positive anomalies in total column water vapor, cloud water, and atmospheric temperature, resulting in a stronger greenhouse effect; years with stronger anomalies had earlier melt onsets [*Mortin et al.*, 2016]. In contrast, years with a late melt onset exhibit clearer skies and negative anomalies in total column water vapor, cloud water, and atmospheric temperature, leading to enhanced radiative cooling [*Mortin et al.*, 2016]. The moisture present in the atmosphere before or at the time of an early melt onset is not local, but instead is transported into the area by passing extratropical cyclones [*Mortin et al.*, 2016]. Interestingly, *Mortin et al.* [2016] also found that repeated moisture transport events that do not result in the onset of melt can nonetheless "precondition" the sea ice for melt by raising air and surface temperatures. As atmospheric moisture transport towards the GrIS has increased in recent years (2000–2015), as demonstrated by *Mattingly et al.* [2016] compared to earlier years (1979–1994), a similar mechanism may be important for preconditioning the GrIS for melt, as described by *Mattingly et al.* [2016]. The work of *Mattingly et al.* [2016] is discussed further in section 2.9.

2.6 Atmospheric Circulation

While a changing surface energy balance has led to higher temperatures and decreased GrIS SMB, the surface energy balance itself is largely controlled by the atmospheric circulation over the GrIS [*Tedesco et al.*, 2016a]. Circulation patterns near Greenland vary greatly by season, with summer patterns being characterized by a weaker general circulation and less active north Atlantic storm track when compared to their

winter counterparts, due to weaker latitudinal temperature gradients [*Schuenemann et al.*, 2009; *Serreze and Barry* 2014]. The result is more cyclonic activity over Baffin Bay and Greenland itself, compared to the winter pattern of more southerly storm tracks across the north Atlantic [*Schuenemann et al.*, 2009].

Also, important in examining atmospheric circulation over Greenland is the role of atmospheric teleconnections, specifically the North Atlantic Oscillation (NAO) and the Atlantic Multidecadal Oscillation (AMO), as well as a Greenland-centric measure of atmospheric blocking, the Greenland Blocking Index (GBI), a measure of the mean 500 hPa geopotential height over the spatial domain 60°N–80°N, 20°W–80°W [*Hanna et al.*, 2013; *McLeod and Mote*, 2016]. Examining the relationship between NAO and Greenland summer temperatures, *Hanna et al.* [2013] found a non-stationary relationship, with 20-year moving windows beginning in the early 20th Century until the mid 1920s showing a statistically significant negative correlation, while those starting between 1925–1945 are insignificant. The relationship becomes significant again for most meteorological stations for moving windows post-1966 [*Hanna et al.*, 2013]. Examining the relationship between AMO and Greenland summer temperatures, insignificant correlations were found for a similar early 20th Century time period, which as *Hanna et al.* [2013] note, includes the 1930s–1940s warm period. Given this, *Hanna et al.* [2013] suggest that other climatic forcings, such as solar forcing or a lack of volcanic activity, previously noted by *Box* [2002], may have played a role in this warm period.

In contrast, GBI, calculated from the NCEP/NCAR reanalysis [*Kalnay et al.*, 1996], showed significant positive correlations at most meteorological stations for the period 1948–2010, and was found to be the best predictor of Greenland coastal

temperatures [*Hanna et al*., 2013]. *Hanna et al*. [2013] suggest a strong link between the positive geopotential height anomalies indicated by the GBI and increasing Greenland temperatures, as one might expect from the hypsometric relationship [*Hanna et al*., 2013].

The GBI is especially useful given the changes seen in atmospheric circulation over Greenland during the 21st Century, with an increasing frequency in persistent high-pressure anomalies [*McLeod and Mote*, 2015; *Hanna et al.*, 2016; *McLeod and Mote*, 2016]. Indeed, its usefulness was shown by *McLeod and Mote* [2016], who conducted a detailed examination of extreme atmospheric blocking episodes over Greenland using a combination of the ERA-40 (1958–1978) and the ERA-Interim (1979–2013) reanalyses.

Using GBI, *McLeod and Mote* [2016] defined an "extreme Greenland blocking episode" (GBE) as 5 or more consecutive days in which the GBI is greater than or equal to the 97th percentile of all the GBI values (1958–2013) in a 7-day window centered on the day in question. Results showed an increase in extreme GBEs since the 1990s, with the number of days per year with an extreme blocking pattern having increased by a factor of two since 1958; the number of GBEs in the 2007 to 2013 alone is close to two standard deviations above the mean for the 1958–2013 period of record [*McLeod and Mote*, 2016]. Although the summer (JJA) blocking episodes were found to be the least intense (in terms of the magnitude of the geopotential height anomalies), this is not surprising given the weaker, more poleward jet stream characteristic of the Arctic summer [*McLeod and Mote*, 2016]. Perhaps most notably, however, is the finding that half of the summer GBEs have occurred from 2000–2013 [*McLeod and Mote*, 2016].

Other work by *McLeod and Mote* [2015] focused on an extended summer season (May–September) and showed that extreme GBEs occurring during the period 1979–2008, were intensified via upper level amplification by so-called "precursor cyclones," or extratropical cyclones that "originated upstream or to the west, of a block's meridional axis at or prior to the peak of blocking intensity" [*McLeod and Mote*, 2015]. GBEs associated with a precursor cyclone resembled omega blocks and led to greater meltwater production (simulated with regional climate model MAR, forced by the ERA-Interim reanalysis) than extreme GBEs not associated with a precursor cyclone, which resembled Rex blocks [*McLeod and Mote*, 2015]. The extreme GBEs associated with precursor cyclones likely enhance meltwater production due to a combination of adiabatic warming under strong high pressure and advection of warm, moist air from the south by the precursor cyclone [*McLeod and Mote*, 2015].

Recent work by *Hanna et al.* [2016] has extended the record of Greenland blocking back into the 19th Century by homogenizing and splicing together the NCEP/NCAR GBI time series with one derived from the 20th Century Reanalysis, version 2c. Like *McLeod and Mote* [2016], *Hanna et al.* [2016] found a rapid increase in GBI values since the 1990s, with the most pronounced increase occurring during meteorological summer (JJA); of the 11 summers with the highest average GBI value, 7 have occurred since 2007 [*Hanna et al.*, 2016]. Also of interest is a sharp drop in JJA GBI in the early 1920s, followed by a sharp rise in the late 1920s and early 1930s [*Hanna et al.*, 2016]. A time series of normalized GBI for the summer months (JJA) can be seen in Figure 2.5. Both July and August saw statistically significant increases in monthly average GBI for the periods 1981–2010 and 1991–2015. The upward trend for the

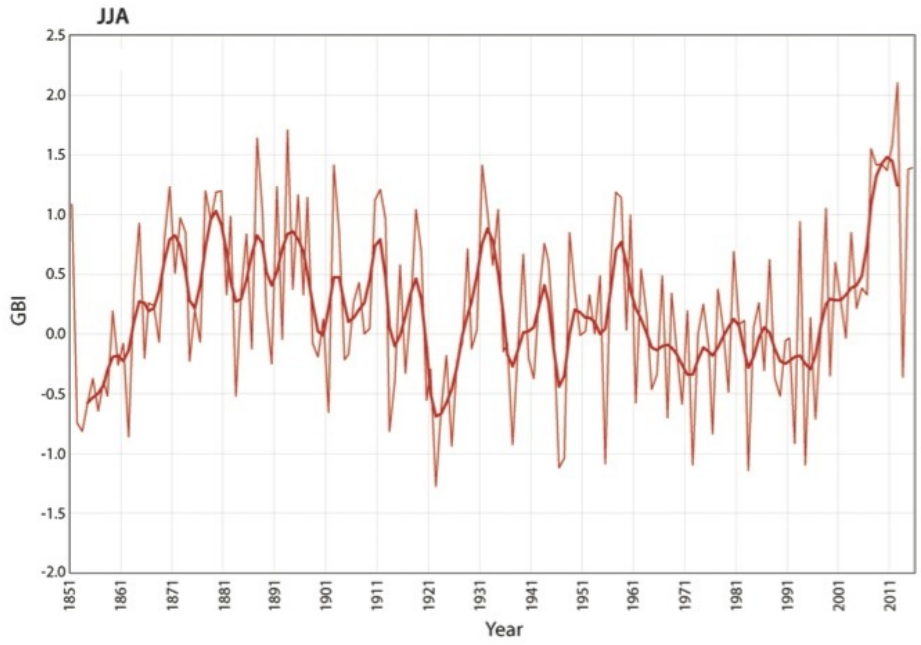

Figure 2.5. Time series of summer (JJA) GBI for the years 1851–2015. Values calculated by normalizing the mean monthly GBI anomaly to the period 1951–2000. Bold line is a 7-point binomial filter. Figure modified from *Hanna et al.* [2016].

summer season was also statistically significant for these two periods. GBI was also found to be negatively correlated with values of the summer NAO (SNAO) index; detrended correlation coefficients show the strongest relation between monthly GBI and Summer NAO is found in June, followed by July and August, respectively.

To examine differences in meteorological conditions between high-GBI summers and low-GBI summers, *Hanna et al.* [2016] averaged the 10 highest GBI summers and 10 lowest GBI summers in the study period and subtracted the low-GBI average from the high GBI average. Difference plots for this analysis can be seen in Figure 2.6. This analysis revealed that high GBI summers are characterized by a positive 500 hPa geopotential height anomaly centered over southwestern Greenland, with a positive 850 hPa temperature anomaly centered slightly to the west of the 500 hPa geopotential height anomaly, over the Labrador Sea. Also of note is a strong negative precipitation anomaly

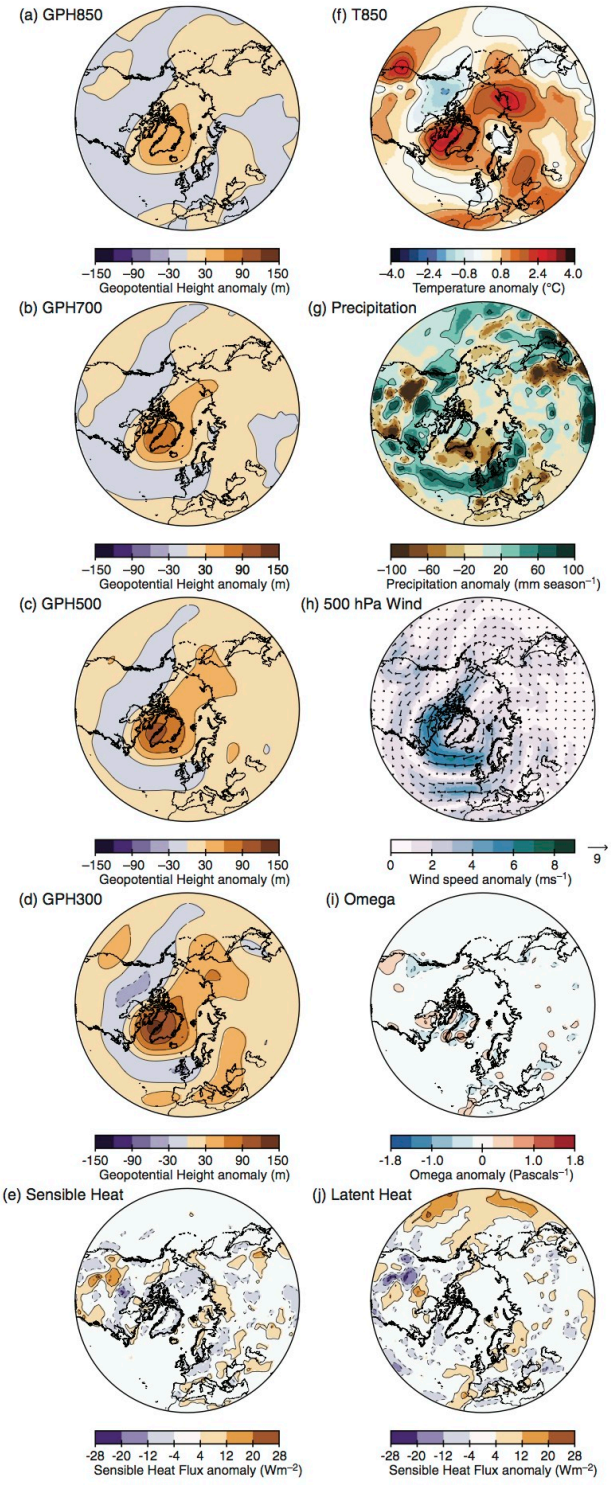

Figure 2.6. Difference plots for summer (JJA) meteorological variables, calculated by subtracting the mean values for the 10 lowest GBI summers from the mean for the 10 highest GBI summers. Figure from *Hanna et al.* [2016].

over southern Greenland, with a much weaker positive precipitation anomaly over northwestern Greenland. The 500 hPa winds around Greenland are characterized by anomalous anticyclonic flow around Greenland, from the Greenland Sea into the Norwegian Sea, around Cape Farewell, and up the western side of Davis Strait [*Hanna et al.*, 2016]. In addition, eastern Greenland also sees a negative sensible heat flux anomaly [*Hanna et al.*, 2016].

While the greatest melt in recent years has been observed in southern Greenland, shifts in atmospheric circulation may dramatically alter the region of the ice sheet experiencing the greatest melt [*Tedesco et al.*, 2016a]. For example, much of July 2015 saw an unusually persistent cut-off high centered over the Lincoln Sea, with 500 hPa geopotential heights nearly four standard deviations above a 1981–2010 mean [*Tedesco et al.*, 2016a]. Simulations of this unusual pattern with regional climate model MAR (forced by the NCEP/NCAR reanalysis) show northwestern Greenland experienced new records for low albedo (due to reduced snowfall and increased melting) and high surface temperatures, along with runoff as high as three standard deviations above a 1950–2015 mean [*Tedesco et al.*, 2016a]. However, this same abnormal circulation pattern also led to easterly winds in southern Greenland, bringing lower temperatures and enhanced snowfall [*Tedesco et al.*, 2016a].

2.7 Synoptic Climatology

Given the large interannual variability in SMB shown by numerous reconstructions and modeling studies, the crucial nature of the SEB in controlling surface temperature and melt, and the many changes seen in atmospheric circulation over the 20th

and 21st centuries, determining the linkages between these processes is critical, both to understand what has happened in the past and to better predict what the future of Greenland may hold. Luckily, the discipline of synoptic climatology provides an answer, as it seeks to determine "the relationship between the atmospheric circulation and the surface environment of a region" [*Yarnal*, 1993]. This relationship may be determined by first developing an atmospheric classification, and then relating this classification to the surface variable of interest; this is termed the "circulation-to-environment" approach by *Yarnal* [1993]. On the other hand, the researcher might employ an alternate "environment-to-circulation" approach that first selects surface environmental data based on a pre-defined threshold, and then relates the selected surface data to the circulation [*Yarnal*, 1993].

Synoptic climatological analysis is used to classify the continuum of different atmospheric conditions into different classes or "types", based on a variable of the researcher's choosing, producing an easily interpretable, physically realistic classification of a given climate [*Cassano et al.*, 2007; *Sheridan and Lee*, 2011]. In seeking to understand the synoptic climatology of a certain variable (e.g., 500 hPa geopotential height), one must find a way to relate the atmospheric circulation to conditions at the surface. Given the spatial and temporal complexity of both reanalysis datasets and regional climate model output, a useful method to extract a pattern or "signal" from these vast reservoirs of information is needed. This can be accomplished by first using a statistical technique such as PCA to identify the principal modes of variability within the data, followed by a clustering technique (such as *k*-means) to group the modes of variability into different classes [*Sheridan and Lee*, 2011].

A pioneering work in Greenland synoptic climatology was the work of *Mote* [1998a], who examined which atmospheric teleconnections were most important in explaining the variability of GrIS surface melt. Using normalized and standardized melt extent data from satellite microwave brightness observations, in combination with 12Z 700 hPa geopotential height fields from the National Meteorological Center's (NMC, now called the National Centers for Environmental Prediction or NCEP) octagonal grid product, Mote performed a rotated principal components analysis (RPCA) to determine the most important modes of variability, or principal components in explaining melt variability over the GrIS for the period May 1979–June 1989, [*Mote*, 1998a]. Notably, the first principal component, which strongly resembled the North Atlantic Oscillation (NAO), showed the strongest correlation to melt extent, exerting an influence in all regions except those on the eastern side of the ice sheet [*Mote*, 1998a]. Overall, 55% of the interannual melt extent trend was due to atmospheric circulation variability [*Mote*, 1998a].

The principal components found in *Mote* [1998a] were subsequently used by *Mote* [1998b] to construct a synoptic climatology of 700 hPa geopotential heights over Greenland, using cluster analysis to group similar events into nine synoptic types. These synoptic types were then used to understand how synoptic variability affects melt extent over the ice sheet as well as over topographic subregions of the GrIS delineated by *Mote* [1998a] [*Mote*, 1998b]. Different synoptic types were found to favor melt in different regions; one type, for example, produced high melt extent in western, southwestern, and southeastern Greenland due to warm air advection onto the ice sheet, while another type

produced the highest melt extent in the northern, eastern and northeastern regions due to onshore flow [*Mote*, 1998b].

Following the work of *Mote* [1998a, 1998b], *Fettweis et al*. [2011a] developed a 1958–2009 summer (JJA) circulation type classification (CTC) using a combination of several different reanalysis products (ERA-40, ERA-Interim, NCEP/NCAR). A similarity index/correlation approach was used to relate 500 hPa geopotential heights to surface melt as modeled by the regional climate model MAR [*Fettweis et al.*, 2011a]. Results showed a shift in synoptic frequencies beginning around 1998, leading to more frequent occurrence of "warm" synoptic types that bring warm air advection and positive 500 hPa anomalies to the region, and less frequent occurrence of "cold" synoptic types associated with negative 500 hPa geopotential height anomalies and below normal temperatures [*Fettweis et al.*, 2011a]. The year 2007, (third highest melt extent on record, see section 2.2) was characterized by very high frequencies of the two synoptic types that favored warm air advection over Greenland [*Fettweis et al.*, 2011a]. Lastly, the NAO, whose negative phase favors warm air advection over Greenland was found to be positively correlated with synoptic types favoring abnormally warm conditions over the GrIS [*Fettweis et al.*, 2011a].

Further work on synoptic type frequency over Greenland was performed by *Fettweis et al.* [2013], who examined the frequency of anticyclonic circulation over Greenland and its relation to the observed increase in days with a negative NAO since the early 1990s. Utilizing the same CTC approach as *Fettweis et al.* [2011a], daily 500 hPa heights for the period 1958–2012 from the NCEP/NCAR Reanalysis were grouped into three broad synoptic types, anticyclonic (associated with negative NAO values), cyclonic

(associated with positive NAO values), and neutral (associated with near-zero NAO values) [*Fettweis et al.*, 2013]. Results show a large increase in the frequency of the anticyclonic type, from 15% to 40%, since the early 1990s [*Fettweis et al.*, 2013]. The increased frequency of anticyclonic circulations leads to increased warm air advection over Greenland, providing favorable conditions for meltwater production. Regional climate modeling with MAR, driven by the NCEP/NCAR Reanalysis, shows increasing meltwater production since the mid-1990s, with the volume of meltwater produced during 1993–2012 being twice that of the period 1961–1990 [*Fettweis et al.*, 2013]. Given the strong links between the NAO changes and the increased melt in Greenland, *Fettweis et al.* [2013] proposes that most of the warming seen over Greenland since the 1990s is a result of the NAO altering atmospheric heat transport, as the same anticyclonic circulation that causes southerly flow over Greenland results in northerly flow over Svalbard, which has not experienced a similar warming.

Building on previous work by *Fettweis et al.* [2011a, 2013], *Belleflamme et al.* [2015], used the CTC methodology to develop a summer (JJA) synoptic climatology of both sea level pressure (SLP) and 500 hPa geopotential heights over a region spanning the Arctic Ocean, Greenland, and the far north Atlantic Ocean for the years 1871–2014, using a combination of five different reanalysis datasets (NCEP/NCAR, ERA-40, ERA-Interim, 20CRv2, and ERA-20C). While this analysis used the CTC methodology of *Fettweis et al.* [2011a, 2013], it differed from these previous studies by using Spearman rank correlation to gauge similarity between circulation patterns, rather than the Euclidean distance metric used previously [*Belleflamme et al.*, 2015]. Classifying the circulation into six representative types, *Belleflamme et al.* [2015] found that a type with

strong high pressure anomalies over Greenland, as well as a type with strong high pressure anomalies over the Beaufort Sea and Arctic Ocean, were both twice as frequent during 2007-2012 when compared with the 1871–2014 average. Similar results were found with the 500 hPa geopotential height climatology; two types with positive geopotential height anomalies co-located with the SLP anomalies were both found to be twice as frequent during 2007–2012 when compared with the 1871–2014 average.

When examining SLP type frequencies during the warm period of the 1920s and 1930s, results from ERA-20C showed a very high frequency of the Beaufort Sea - Arctic Ocean high pressure anomaly during the period 1923–1931, which could be a possible explanation for the warmer temperatures associated with these years; however, no similar trend in type frequency was seen for 1923–1931 when examining the 20CRv2 results [*Belleflamme et al.*, 2015]. The 500 hPa analysis showed no anomalies for the 1923–1931 period with either ERA-20C or 20CRv2 [*Belleflamme et al.*, 2015].

Belleflamme et al. [2015] also examined the effect of uncertainty in the 20CRv2 data (itself the mean of 56 ensemble members) on the classification process by comparing classification results derived from the 20CRv2 ensemble mean (i.e., "reference run") with results obtained by taking the daily ensemble mean values and adding the daily "spread" values (standard deviation of ensemble mean) multiplied by a random value from -1 to +1. This process of adding a scaled spread value to the daily ensemble means was repeated 20,000 times (i.e., "classification runs") to assess whether changes in the SLP or 500 hPa geopotential height resulted in a change in type classification [*Belleflamme et al.*, 2015]. Results showed that the "classification runs" overestimated the frequency of the Beaufort Sea-Arctic Ocean high pressure anomaly

type, as well as a type defined by a strong low-pressure anomaly centered near the North Pole when compared with the "reference run" before 1940 [*Belleflamme et al.*, 2015]. This is attributed to a relatively low number of surface observations assimilated into the reanalysis before 1940, resulting in a large amount of spread in the region of the Arctic Ocean where the type frequency anomalies were observed [*Belleflamme et al.*, 2015]. As more pressure observations are assimilated, uncertainty in the frequency of each type declines, doing so rapidly from 1930-1950 and becoming insignificant in more recent decades; similar results are seen for the 500 hPa geopotential height analysis [*Belleflamme et al.*, 2015]. The ensemble nature of the 20CRv2c dataset and associated uncertainty is discussed further in section 3.1.2.

2.8. The Self-Organizing Map (SOM)

While the previous techniques described (PCA, cluster analysis, circulation type classification, similarity index) have all produced valuable climatological data, the expanding field of machine learning, specifically artificial neural network technology, has recently brought a new tool to the synoptic climatologist: the self-organizing map or SOM [*Sheridan and Lee*, 2011].

The self-organizing map is an "unsupervised, iterative, machine learning method" [*Mattingly et al.*, 2016] that allows one to perform two different tasks; "mine" the data set to find patterns within, while also clustering the data into groups based on similarity of a given variable [*Liu and Weisberg*, 2011]. The SOM methodology is especially useful in synoptic climatology, as it allows one to easily relate the atmospheric circulation (sea-

level pressure and/or geopotential heights) to other variables such as air temperature and precipitation [*Liu and Weisberg*, 2011].

The person who introduced the self-organizing map, Teuvo Kohonen, describes the method as a "data-analysis method that visualizes similarity relations in a set of data items" [*Kohonen*, 2014]. It does so by, in the words of Kohonen, producing "low-dimensional projection images of high-dimensional data distributions" [*Kohonen*, 2014]. The high-dimensional input to the computational software used to build the self-organizing map is often data from a reanalysis, such as the ERA-40 or ERA-Interim reanalyses [*Schuenemann and Cassano*, 2009, 2010; *Schuenemann et al.*, 2009]. Unlike more traditional synoptic climatological analysis methods that first determine the primary modes of variability in the data set (with PCA or a similar technique) and then group the resulting components of variability into a number of discrete categories, the SOM technique first places a pre-specified number of nodes into the data space, and then adjusts the position of these nodes through an iterative process to find the distribution most representative of the data set [*Hewitson and Crane*, 2002; *Sheridan and Lee*, 2011].

The product, or low-dimensional output, of this process is usually "a two-dimensional array or "map" of nodes, that represents the continuum of variability within the data set" [*Mattingly et al*., 2016]. SOM output can be easily used to visualize the relationships between nodes/synoptic types, as similar nodes/types are in close proximity to one another, while very different nodes/types (such as positive anomalies vs. negative anomalies) are found at opposite sides or corners of the map [*Hewitson and Crane*, 2002; *Liu et al.*, 2006; *Sheridan and Lee*, 2011; *Skific and Francis*, 2012; *Mattingly et al.,* 2016]. This allows the researcher to easily visualize extremes and the transitional states in

between these extremes [*Hewitson and Crane*, 2002; *Sheridan and Lee*, 2011; *Mattingly et al.*, 2016].

SOMs have been compared with other methods of pattern extraction, such as principal component analysis (PCA), by testing their ability to extract known patterns from synthetic data sets. *Reusch et al.* [2005] used idealized North Atlantic sea level pressure fields to compare the ability of PCA and SOMs to extract known patterns. While the PCA-based method (with and without rotation) showed numerous problems (extraction of non-existent patterns, pattern mixing, incorrect variance assignment, known patterns not extracted), the SOM technique was able to extract the known patterns and assign the correct frequency of occurrence to each pattern [*Reusch et al*., 2005]. The SOM technique also has the advantage of producing output that is easy to interpret, with each node being representative of a generalized physical state [*Reusch et al.*, 2005]. Furthermore, the SOM technique, in contrast to PCA, makes no assumptions about the data structure or distribution; instead, the successive iterations extend the nodes over the entire data set [*Hewitson and Crane*, 2002; *Sheridan and Lee*, 2011]. As a result, information that may be lost with a traditional clustering algorithm is preserved, and areas of low data density can be effectively interpolated [*Hewitson and Crane*, 2002]. In addition, the SOM algorithm utilizes a distance decay calculation; when the position of one node is adjusted based on input data, it also adjusts the position of nearby nodes, thus allowing input data to contribute to multiple nodes, and more closely reflecting the continuous nature of the data [*Hewitson and Crane*, 2002; *Sheridan and Lee*, 2011].

When using the SOM algorithm, the choice of the number of nodes is a subjective decision left to the researcher. The number of nodes is a compromise between simplicity

and accuracy, similar to other clustering methods [*Liu et al.*, 2006]. Fewer nodes leads to greater interpretability, but can result in excessive averaging, resulting in large amounts of intranode variability and unphysical patterns, and thus reducing the power of the classification. In contrast, the use of an excessive number of nodes makes the classification more difficult to interpret, and risks over splitting representative patterns. [*Schuenemann et al.*, 2009; *Skific and Francis*, 2012]. Thus, SOM studies often evaluate numerous map sizes to determine which is most suitable [*Schuenemann et al.*, 2009; *Bezeau et al.*, 2015].

2.9 Self-Organizing Maps (SOMs) in Arctic and Greenland Research

SOMs have previously been used in investigating pan-Arctic climate and how it may change in the future due to anthropogenic forcing. *Cassano et al.* [2007] investigated the synoptic forcing of precipitation in the Arctic in both reanalysis datasets and the output of global climate system model simulations (GCSMs) for the middle and late 21st Century. Using data for the years 1991–2000, 2046–2055, and 2091–2100, *Cassano et al.* [2007] created a synoptic climatology of sea level pressure for the pan-Arctic region. The use of GCSM data allowed for the prediction of changes in net precipitation over the Arctic during the 21st Century, with results showing increased net precipitation, although it was found that most of this change is likely to be from thermodynamic forcing (changes in precipitation within a given type), rather than circulation-driven, dynamic forcing [*Cassano et al.*, 2007].

SOMs were used in a similar matter to *Cassano et al.* [2007] by *Skific et al.* [2009] to examine changes in atmospheric moisture transport into the Arctic region

during the 21st Century. Combining sea-level pressure data from the ERA-40 reanalysis with Community Climate System Model (CCSM3) simulations of the period 1960–1999, 2010–2030, and 2070–2089, *Skific et al.* [2009] created a SOM to examine the continuum of sea-level pressure fields, observed and predicted, over the Arctic north of 60°N. By associating each circulation type with a representative pattern of atmospheric moisture transport into the Arctic, future trends in the frequency of occurrence of each circulation type and associated moisture transport pattern were assessed. Like the work by *Cassano et al.* [2007], *Skific et al.* [2009] found an increasing amount of moisture transport into the Arctic by the late 21st Century, with most of the change attributed to thermodynamic factors rather than dynamic factors/circulation changes [*Skific et al.*, 2009]. Notably, the biggest changes in moisture transport are predicted to occur during the summer, with major ramifications for Arctic cloud cover, precipitation, and by extension, the surface energy balance, due to increased longwave radiation emissions and latent heat transport [*Skific et al.*, 2009].

SOMs have also been utilized to examine smaller sub-regions of the Arctic; *Bezeau et al.* [2015] used data from the NCEP/NCAR Reanalysis (1948–2012) as well as five Coupled Model Intercomparison Project Phase 5 (CMIP5) models (1950–2025), to construct a SOM and examine changes in summer (JJA) atmospheric circulation using 500 hPa geopotential heights over a domain centered on Baffin Bay and extending across much of the eastern Canadian Arctic Archipelago (CAA) and western Greenland. Over the period 1948–2006, nodes featuring strong positive 500 hPa height anomalies (termed "nodes of interest") over the study domain occurred at a frequency of 13.6%, but this frequency rose to 36.2% for the period 2007–2012, a statistically significant increase. In

addition, the frequency of persistent anticyclones over the study domain showed dramatic increases since 2007 [*Bezeau et al.*, 2015]. Using the number of times per summer that the circulation stayed in a "node of interest" for 6 or more days as an indicator of a persistent anticyclonic circulation, *Bezeau et al.* [2015] found that since 2007, this type of pattern occurs two to three times per summer, compared to years before 2007, most of which have either zero or one occurrence of the is type of persistent anticyclone.

Similar work on past and future climate, albeit with a focus on Greenland rather than the entire Arctic, was performed by *Schuenemann et al.* [2009], who examined synoptic forcing of precipitation over Greenland to better understand a key input to GrIS surface mass balance [*Schuenemann et al.*, 2009]. Using the ERA-40 reanalysis, *Schuenemann et al.* [2009] examined representative sea-level pressure patterns near Greenland, along with the precipitation pattern associated with each circulation pattern. This work was later expanded on by *Schuenemann and Cassano* [2009], who used SOMs to construct a synoptic climatology similar to that of *Schuenemann et al.* [2009], using data from both ERA-40 and 15 global climate models (GCMs) used to generate data for the Intergovernmental Panel on Climate Change Fourth Assessment Report (IPCC AR4). The SOM produced can be seen in Figure 2.7.

Average daily precipitation for each synoptic type was found to correspond strongly with the surface pressure pattern; for example, a Baffin Bay cyclone leads to precipitation over the southern GrIS, while a North Atlantic cyclone leads to relatively sparse precipitation, mainly along the southeastern coast. The three GCMs that best reproduced the ERA-40 climatology were then used by *Schuenemann and Cassano* [2010] to simulate the future climate of Greenland for the periods 2046–2065 and

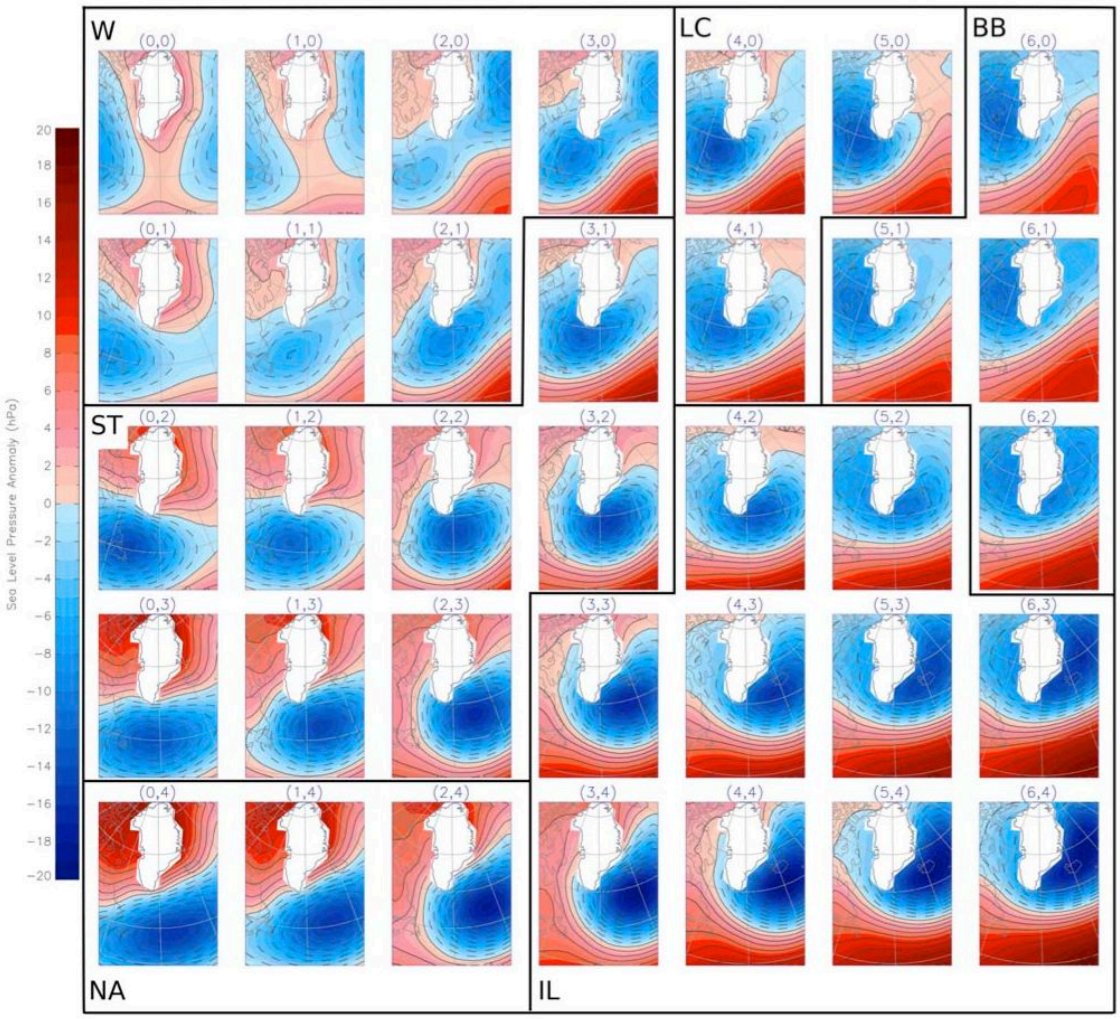

Figure 2.7. Master SOM produced by *Schuenemann and Cassano* [2009]. SOM depicts continuum of SLP anomalies based on training data from ERA-40 and IPCC AR4 GCMs. Abbreviations for grouping of nodes are as follows: W=Weak, LC=Labrador Cyclone, BB=Baffin Bay Cyclone, ST=Southern Tip Cyclone, NA=North Atlantic Cyclone, IL=Icelandic Low Cyclone. Figure from *Schuenemann and Cassano* [2009].

2081–2100. The results indicated that precipitation over Greenland would increase by 10 cm yr^{-1} (equivalent to 200 km^3 of ice) due to the North Atlantic storm track shifting northwards, as well as increased precipitable water values due to increased air temperatures and hence higher saturation vapor pressures [*Schuenemann and Cassano*, 2010]. The changes in Greenland precipitation were due to both changes in synoptic

frequencies and intrapattern variability, but intrapattern variability was by far the dominant effect, as it accounted for 82.5% of the observed changes [*Schuenemann and Cassano*, 2010].

In addition to predicting future precipitation over Greenland, the SOM methodology has recently been used by *Mioduszewski et al.* [2016] to examine summer (JJA) synoptic patterns over the high latitudes of the northern hemisphere (60°N and poleward) and their effects on surface melt on the GrIS. Using data from NASA's MERRA reanalysis [*Rienecker et al.*, 2011] for the period 1979–2014, *Mioduszewski et al.* [2016] examined daily 500 hPa geopotential height patterns and, when comparing the period 1979–1988 to 2005–2014, found a statistically significant increase in several patterns characterized by positive 500 hPa geopotential height anomalies over Greenland, while patterns characterized by negative 500 hPa geopotential height anomalies over Greenland showed statistically significant decreases [*Mioduszewksi et al.*, 2016]. The master SOM produced by *Mioduszewksi et al.* [2016] can be seen in Figure 2.8.

Data from the regional climate model MAR (forced by the NCEP/NCAR reanalysis) was then used to develop composites of meltwater production and surface energy balance parameters (cloud cover, shortwave radiation, longwave radiation, latent heat flux, sensible heat flux) for each SOM node [*Mioduszewski et al.*, 2016]. Positive height anomalies were generally associated with positive anomalies in meltwater production, positive anomalies in downwelling shortwave and longwave radiation, but negative anomalies in cloud fraction and sensible heat flux (negative numbers indicate a sensible heat flux directed downward); the signs of these anomalies were reversed for

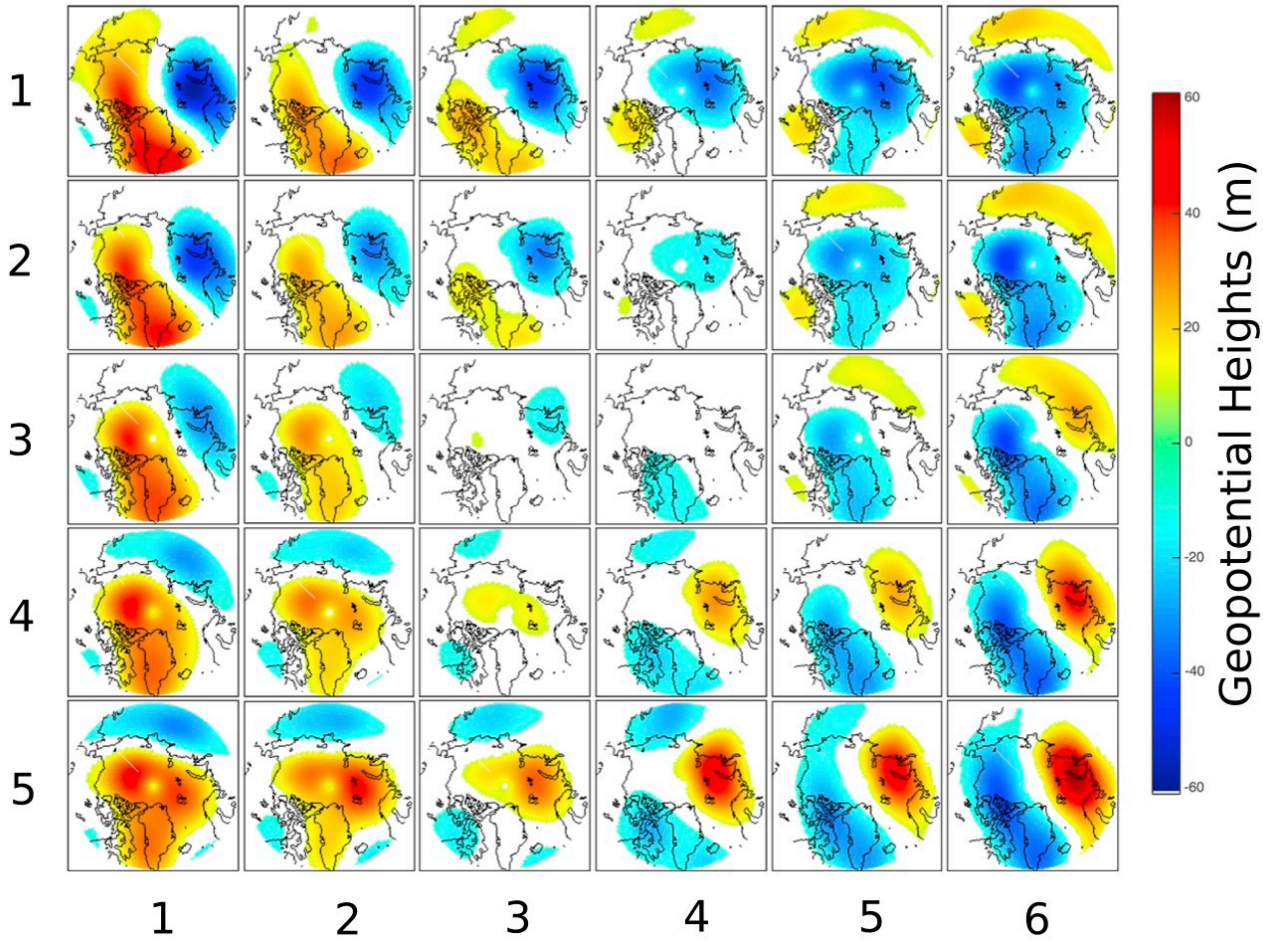

Figure 2.8. Master SOM produced by *Mioduszewski et al.* [2016]. SOM depicts continuum of 500 hPa geopotential height anomalies for JJA days, 1979–2014. Figure from *Mioduszewski et al.* [2016].

negative height anomalies [*Mioduszewski et al.*, 2016]. In addition, *Mioduszewski et al.* [2016] also examined whether the acceleration in GrIS mass loss in recent decades was due mostly to thermodynamic factors (changes in mass loss within a single synoptic type), dynamic factors (changes in type frequency), or a combination of both; results showed that thermodynamic factors were mainly responsible for the increased mass loss, with more melt occurring in a given synoptic type between 2005–2014 than 1979–1988,

likely due to a surface energy balance that is more favorable for melt [*Mioduszewski et al.*, 2016].

While SOM analysis in the Arctic region has traditionally been used for analyses of atmospheric variables such as sea level pressure (SLP) and geopotential height [*Cassano et al.*, 2007; *Mioduszewski et al.*, 2016], the technique has also been with integrated vapor transport (IVT), a vertically-integrated metric of atmospheric moisture transport often used in the study of atmospheric rivers. Examining trends in IVT near Greenland using the ERA-Interim reanalysis, *Mattingly et al.* [2016], comparing the periods 1979–1994 and 2000–2015, found statistically significant increases in so-called "wet" and "neutral" nodes (nodes having anomalously high IVT values over Greenland and nodes having near-median values of IVT over Greenland, respectively), while finding statistically significant decreases in "dry" nodes (nodes having anomalously low IVT values over Greenland) [*Mattingly et al.*, 2016].

2.10 Summary

Greenland has seen record numbers of warm extremes in the first decade of the 21st Century, more than any other decade in the 20th Century or the 1890s [*Mernild et al.,* 2014]. However, portions of the early 20th Century also saw warm temperatures, with temperatures in the 1930s and 1940s in coastal southern Greenland being similar to those of the late 1990s forward [*Hanna et* al., 2007], while a period of warming between 1919–1932 was 33% greater in magnitude than that experienced between 1994–2007 [*Box et al.*, 2009].

In addition, melt extent has seen a drastic increase in the early years of the 21st Century as compared to the 20th Century, with new records being set every few years

(2003, 2005, 2007, 2010, 2012) [*Fettweis et al*., 2011b; *Box et al.*, 2011; *Tedesco et al.*, 2013]. GrIS mass loss is increasingly dominated by the SMB term, as evidenced by numerous studies [*Rignot et al.*, 2011; *Enderlin et al.*, 2014; *Andersen et al.*, 2014; *Kjeldsen et al.*, 2015; *van den Broeke et al.*, 2016]. The SMB term itself is becoming increasingly negative [*Shepherd et al.*, 2012; *Csatho et al.*, 2014], but displays great interannual variability, due to changes in its respective terms [*Box*, 2013].

The surface energy balance is key to determining the surface temperature and thus whether melt will occur. Surface energy balance depends not only on albedo, but also on other factors such as air mass advection [*Neff et al.*, 2014] and cloud optical depth [*Bennartz et al.*, 2013]. Both radiative and non-radiative fluxes may play a part in providing energy for melt, depending on local weather conditions [*Fausto et al.*, 2016]. Moisture transport into the Arctic, projected to increase in the future [*Skific et al.*, 2009; *Lavers et al.*, 2015], may also have important implications for GrIS surface energy balance [*Mattingly et al.*, 2016; *Mortin et al.*, 2016].

The atmospheric circulation over Greenland, which controls the surface energy balance of the GrIS [*Tedesco et al.*, 2016a], is increasingly characterized by extreme blocking events; 50% of the summer extreme blocking events over the period 1958–2013 have occurred since the years 2000 [*McLeod and Mote*, 2016]. In addition, values of the GBI, used to assess the strength of blocking, have increased since the 1990s, with the biggest increase during meteorological summer (JJA) [*Hanna et al.*, 2016]. These findings are also supported by numerous synoptic climatological analyses, which have also shown an increasing frequency of positive 500 hPa geopotential height anomalies

over Greenland during the summer [*Fettweis et al.*, 2011a; *Fettweis et al.*, 2013; *Belleflamme et al., 2015*; *Mioduszewski et al.*, 2016].

CHAPTER 3

DATA AND METHODS

The purpose of this study is to classify the atmospheric circulation over Greenland during meteorological summer (JJA) into representative synoptic types, determine whether the atmospheric circulation associated with certain synoptic types modifies the surface energy balance of the GrIS such that greater mass losses are observed in these types than others, and finally, to determine if there are statistically significant changes in synoptic type frequency during the period 1900–2014.

The synoptic climatology of summer 500 hPa geopotential heights were created using data from the 20CRv2c reanalysis. Daily 500 hPa data was classified using self-organizing maps, with a final result of 24 synoptic types or "nodes" representing the continuum of variability in the 500 hPa circulation above Greenland and the surrounding oceans. Subsequently, output from regional climate model MAR (v3.5.2), forced by 20CRv2c, was used to examine key surface energy balance and surface mass balance variables in each of the 24 nodes. Finally, the statistical significance of both decadal and multi-decadal changes in node frequency was tested by using the binomial distribution method of *Cassano et al.* [2007] and *Mioduszewski et al.* [2016].

3.1 Data

3.1.1 Choice of Reanalysis Datasets

In order to reconstruct the state of the atmosphere over the study domain for the period 1900–2014, a source of data is needed that is both spatially and temporally homogeneous. As has been the case in previous SOM studies of Greenland climate [e.g., *Schuenemann and Cassano*, 2009, 2010; *Schuenemann et al.*, 2009; *Mattingly et al.*, 2016; *Mioduszewski et al.*, 2016] atmospheric data used in training the SOM in this study came from an atmospheric reanalysis product. Reanalysis products have the advantage over other data sources (such as operational forecasting output) of using an unchanging data assimilation scheme for the entire modeling period, ensuring that any signals in the data are due to actual changes in the modeled system rather than an artifact of a change in the data assimilation scheme [*Cassano et al.*, 2007].

Given that the period for this study includes the early decades of the 20th Century, the choice of reanalysis product is limited, given that the vast majority of these products cover either only the satellite era (1979–present) or in the case of the NCEP/NCAR reanalysis, extend back to only 1948. However, there are two reanalysis products covering this era: the 20th Century Reanalysis, version 2c (20CRv2C), produced by the National Oceanic and Atmospheric Administration (NOAA), and the ERA-20C, produced by the European Centre for Medium-Range Weather Forecasts (ECMWF). While the ERA-20C reanalysis does have the advantage of a finer spatial resolution than 20CRv2c (210 km vs. 125 km horizontal distance, 91 vs. 28 vertical levels), and thus the ability to resolve smaller-scale details of the atmospheric circulation, it only covers the

years 1900–2010. However, the most recent version of the 20CRv2c, extends to the end of 2014, allowing for the examination of a larger portion of the 21st Century, including the extreme 2012 melt season. The 20CRv2c also has the advantage of providing estimates of the uncertainty of each analysis [*Compo et al.*, 2011]. Based on the value of additional years of data, as well as the uncertainty estimates, 20CRv2c was selected for use in this study.

This study follows *Bezeau et al.* [2015] and *Mioduszewski et al.* [2016] in using 500 hPa geopotential height as the atmospheric variable for use in SOM training. The 500 hPa level allows for analysis of the motion of cyclones and anticyclones that determine atmospheric conditions over Greenland, while also being located high enough in the troposphere to be above ground for all parts of Greenland. While previous Greenland SOM studies [*Schuenemann and Cassano* 2009, 2010; *Schuenemann et al.*, 2009] have used mean sea level pressure (MSLP) as the variable of interest, data over the high elevations (>500 m) of Greenland was excluded from the SOM training process due to concerns about the accuracy of this variable over elevated terrain. Given prior precedent, as well as the need to include atmospheric data over all of Greenland, 500 hPa geopotential height was chosen as the variable of interest.

3.1.2 20th Century Reanalysis, version 2c

The 20CRv2c atmospheric reanalysis dataset (available online at http://www.esrl.noaa.gov/psd/data/20thC_Rean) depicts the state of the global troposphere every six hours at 2° spatial resolution, while also giving an estimate of the uncertainty in the analysis [*Compo et al.*, 2011]. Surface pressure is the only variable

assimilated; while the lateral boundaries are forced using monthly sea-ice extent and sea surface temperature data [*Compo et al.*, 2011]. Version 2c of 20CR spans the years 1851–2014, a record of 164 years. The output of the 20CRv2c includes numerous analyzed variables useful for climate reconstruction, such as air temperature, geopotential height, and wind, as well as numerous forecast parameters (cloud cover, albedo, snowcover, etc.); a full listing is available online at http://www.esrl.noaa.gov/psd/data/gridded/data.20thC_ReanV2c.html.

The 20CRv2c reanalysis uses an ensemble Kalman filter data assimilation method, with the output being the mean of a 56-member ensemble [*Compo et al.*, 2011; *Belleflamme et al.*, 2015]. An estimate of uncertainty ("spread") is provided by taking the standard deviation of the ensemble mean [*Compo et al.*, 2011; *Belleflamme et al.*, 2015]. As previously discussed in section 2.7, the amount of spread is dependent on the number of pressure observations assimilated; the spread decreases during the period 1930–1950 as more pressure observations are assimilated [*Belleflamme et al.*, 2015]. This is illustrated in Figure 3.1 for 20CRv2 500 hPa geopotential height data, and in Figure 3.2 for 20CRv2c sea level pressure data.

The 20CRv2 reanalysis was tested for forecast skill by *Compo et al.* [2015], comparing a 24-hour forecast of surface pressure with a persistence forecast (the assumption that conditions in 24 hours will be the same as at the present time). For the northern hemisphere, the 20CRv2 forecasts easily outperformed a persistence forecast for the 1900–2014 period, with the performance improving in later years as additional

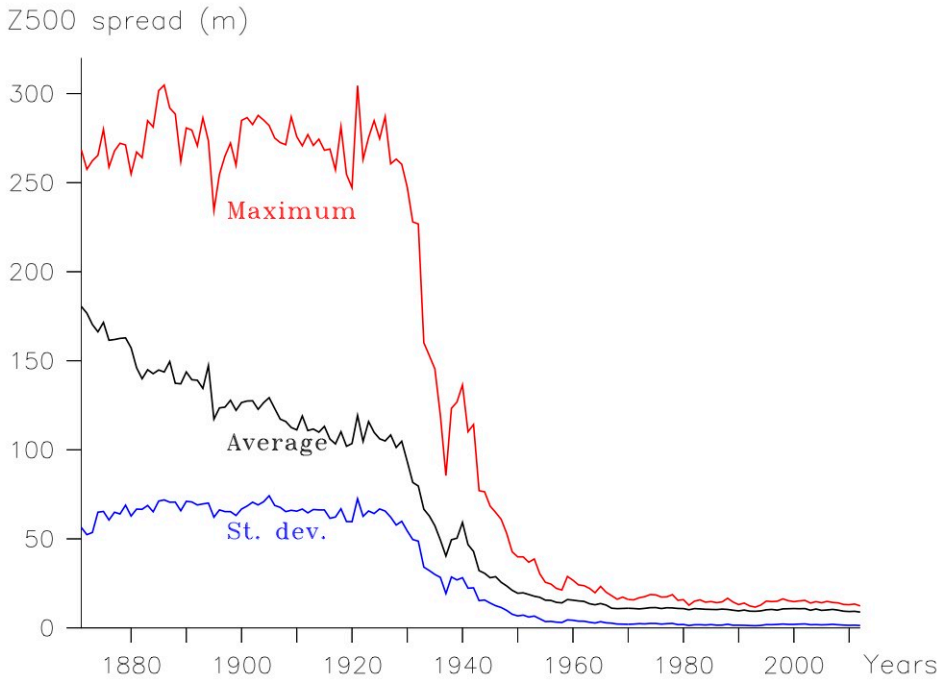

Figure 3.1. Depicted are the maximum spread (red), average spread (black) and the standard deviation of the average spread (blue) from the 500 hPa geopotential height synoptic climatology of *Belleflamme et al.* [2015]. Spread decreases rapidly as more observations are assimilated. Figure modified from *Belleflamme et al.* [2015].

observations were available for assimilation into the reanalysis dataset [*Compo et al.*, 2015.

3.1.3 Regional Climate Model MAR, version 3.5.2

While the 20CRv2c provides the needed geopotential height data for training the SOM and establishing the circulation component of the synoptic climatology, it does not provide high-resolution data regarding the surface mass balance and surface energy balance of the GrIS. Thus, like previous studies of Greenland climate [e.g.,

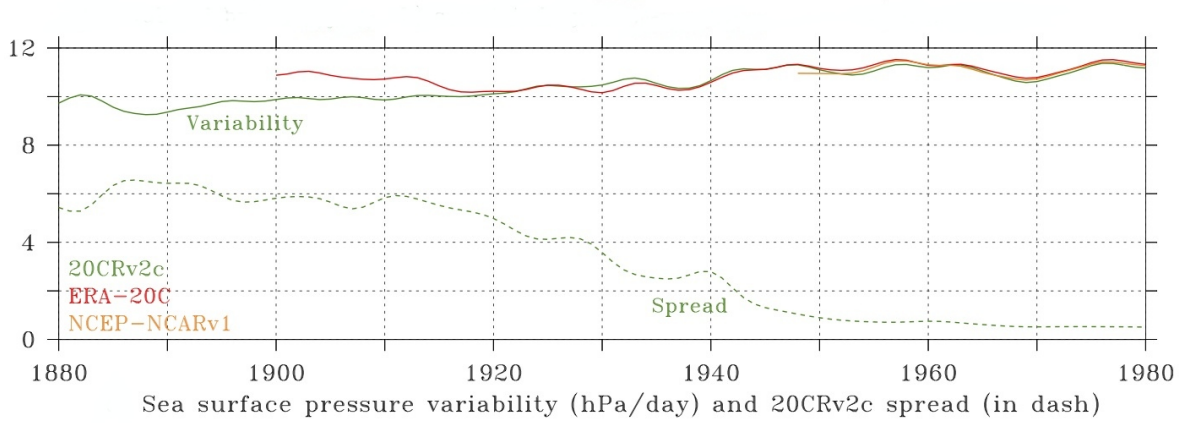

Figure 3.2. Depicted are the 10-year running means of annual mean daily variability in sea level pressure in a spatial domain centered on Greenland for three different climate reanalysis products. The ensemble mean spread for 20CRv2c is also shown (dashed line). Spread decreases as more observations are assimilated. Figure modified from *Fettweis et al.* [in press].

Mioduszewski et al., 2016] this work utilizes a regional climate model to provide the key environmental information needed to construct the "circulation to environment" link described by *Yarnal* [1993].

Following previous work by *Fettweis et al.* [2011a, 2013] and *Mioduszewski et al.* [2016], this work utilized the regional climate model MAR. MAR is composed of a hydrostatic, sigma-coordinate atmospheric model [*Gallée and Schayes*, 1994], coupled to the surface scheme SISVAT (Soil Ice Snow Vegetation Atmosphere Transfer) [*DeRidder and Gallée*, 1998] as well as a multiple-level snow model, CROCUS [*Brun et al.*, 1992]. CROCUS is used to model snowpack processes important for both mass and energy balance, such as firn compaction and meltwater retention/refreezing [*Vernon et al.*, 2013].

It is important to note that when MAR is forced by 20CRv2c, the relative lack of assimilated pressure observations in the early 20th Century results in modeled pressure fields that are too smooth, producing artificially low estimates of precipitation rate

[*Fettweis et al.*, in press]. In addition, *Fettweis et al.* [in press] compared MAR simulations forced by 20CRv2c with those forced by ERA-Interim during the period 1980–1999, finding several biases in the 20CRv2c-forced simulation when compared with the ERA-Interim simulation. These include a warm bias in northern Greenland and a cold bias in southwestern Greenland, as well as a slight overestimation of runoff for most of the ice sheet compared with simulations forced by ERA-Interim, although this is not true in the southwest due to the cold bias [*Fettweis et al.*, in press]. Lastly, artificially low 500 hPa wind speeds in 20CRv2c result in 20CRv2c-forced MAR simulations that produce too much precipitation in northeastern Greenland and too little precipitation in northwestern Greenland [*Fettweis et al.*, in press].

MAR output data for this study were provided by Dr. Xavier Fettweis, Department of Geography, University of Liège, Belgium. Modeling was performed with MAR version 3.5.2, with 20CRv2c providing forcing at the model's lateral boundaries. MAR output used in this study is daily resolution, spanning the years 1900–2014, with a spatial resolution of 20 km. Data are on a stereographic projection, with a spatial extent of 83.9°N–59.2°N, 88.4°W–5.1°E.

3.2 Methods

3.2.1 SOM Data Pre-Processing

Daily-resolution 20CRv2c 500 hPa geopotential height data was obtained from the 20CRv2c website (http://www.esrl.noaa.gov/gridded/data.20thC_ReanV2c.html) for the years 1900–2014. While the reanalysis data is available back to the year 1851, the

years 1851–1899 were not included in the SOM analysis, as the MAR output used for constructing the synoptic climatology only extends back to the year 1900. The data was then processed to include only summer (JJA) days for each year, as well as to include only 500 hPa geopotential height data from within a spatial domain centered on Greenland. This spatial domain extends from 50°N–86°N, 100°W–10°E. A map of this domain can be found in Figure 3.3. The product is a series of 10,580 (92 days per summer x 115 years) 500 hPa geopotential height maps.

While the raw 500 hPa geopotential height data can be used for training the SOM, this work follows *Mioduszewski et al.* [2016] by instead using daily 500 hPa geopotential height anomalies for training. Use of daily anomalies rather than raw data is common in synoptic climatological work conducted in the Arctic (see section 2.9) and allows for a better examination of extreme states [*Mattingly et al.*, 2016]. For a given day of the year, data from all 115 years in the record was averaged on a gridpoint basis to calculate a climatological mean for that day. This mean was then subtracted from each of the 115 days in the record to calculate their deviation from the mean state. The result of this process was 10,580 500 hPa geopotential height anomaly maps, which served as the input data for the training process.

3.2.2 SOM Training

Construction and training of the SOM was performed using SOM Toolbox, a package of functions and algorithms for the MATLAB scientific computing environment [*Vatanen et al.*, 2015]. The toolbox, developed by the former Laboratory of Computer and Information Science, Helsinki University of Technology (now a part of Aalto

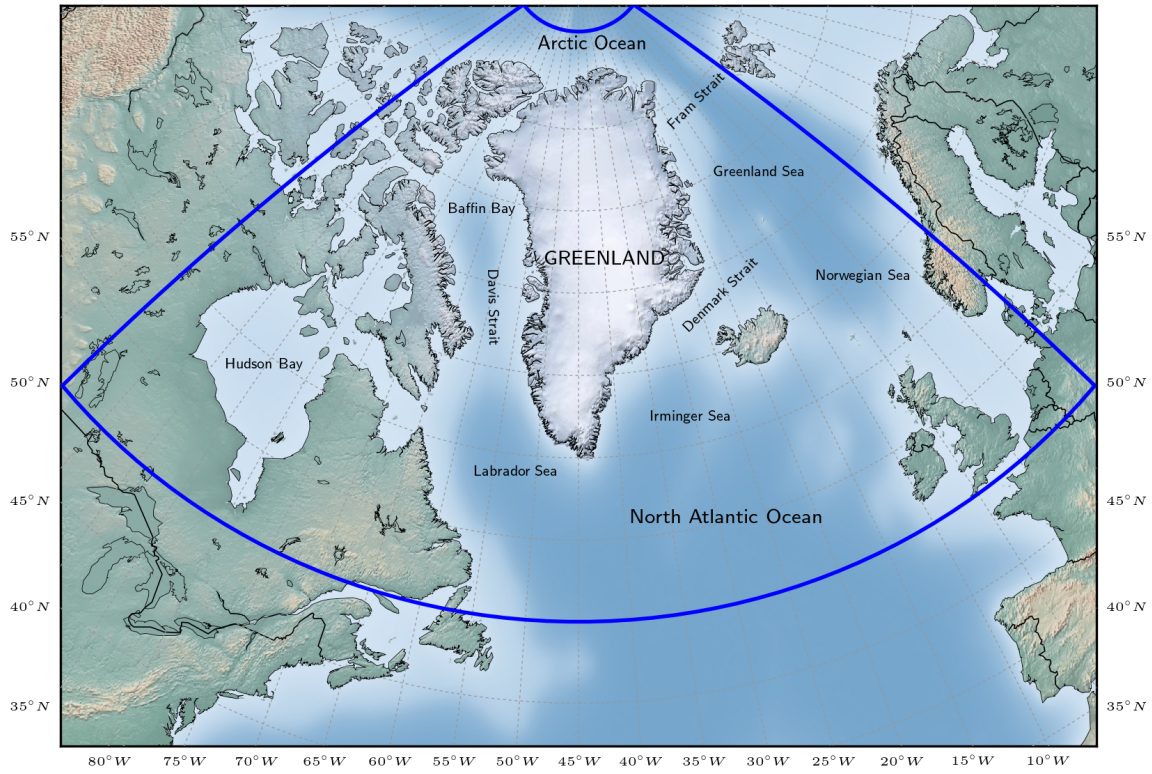

Figure 3.3. Spatial domain used for SOM training. The domain covers 50°N–86°N, 100°W–10°E, with gridpoints at 2° spatial resolution.

University), is open-source and is freely available online at http://research.ics.aalto.fi/software/somtoolbox.

Given that the researcher must choose the number of nodes to be used when constructing the SOM, as well as the fact that the choice of map size is critical to the success of the classification (see section 2.8), several different map sizes were evaluated: 35 nodes (7 columns x 5 rows), 30 nodes (6 columns x 5 rows), 24 nodes (6 columns x 4 rows), and 20 nodes (5 columns x 4 rows). All SOM grid sizes used were "asymmetrical"; that is, the number of rows and the number of columns were not equal (a square grid). Instead, rectangular grids were used for ensuring stability during the training

process [*Reusch et al.*, 2005]. The training and post-processing process described below was repeated for each of the four map sizes.

Before training, the SOM input data was normalized to ensure that no data point(s) had disproportionate influence on the training results [*Vesanto et al.*, 2000]. Next, the SOM was initialized by placing the chosen number of nodes into the data space using a linear initialization process. Linear initialization, which places the nodes in the data space based on the first two eigenvectors of the training data's covariance matrix, is preferred over initializing the SOM randomly (nodes are spaced evenly within the data space) as it results in a faster training process [*Vesanto et al.*, 2000; *Reusch et al.*, 2005; *Skific et al.*, 2009; *Skific and Francis*, 2012]. In initializing the SOM, a "sheet" map shape (global topology) was selected, following *Liu et al.* [2006], as well as a hexagonal lattice shape (local topology). In choosing the lattice shape, which describes the spatial relation between a node and its neighbors, a hexagonal lattice is preferred over the alternative rectangular lattice, as it results in greater connectivity between nodes [*Bezeau et al.*, 2015].

Once initialized, the SOM was trained using a batch training algorithm. This algorithm takes all input vectors (each vector being an ordered list of 500 hPa geopotential height anomaly values across the domain on a specific day) and groups the data based on distance from a given node, represented by a weight vector; the process is similar to the creation of a Voronoi diagram [*Vesanto et al.*, 2000; *Skific and Francis*, 2012]. Each input vector is then assigned a "best matching unit" (BMU), which is the weight vector that it lies closest to in the data space, as measured by Euclidean distance [*Reusch et al.*, 2005; *Cassano et al.*, 2007; *Skific et al.*, 2009; *Skific and Francis*, 2012].

The values of the weight vectors are then updated based on a weighted mean of the input data, and the process repeated for a pre-specified number of iterations. This method is preferred over a sequential training algorithm, where each input vector is processed one at a time, as it is more computationally efficient [*Liu et al.*, 2006; *Bezeau et al.*, 2015].

Like the choice of the number of nodes, the number of iterations to be used is also a choice left to the user. In the process of training, it was found that 1000 iterations produced an acceptable result; smaller values resulted in maps that did not display a smooth progression from one 500 hPa geopotential height anomaly pattern to another, likely showing that the SOM algorithm had not yet reached a "stable" state, while larger values delivered nearly identical results, indicating the algorithm has converged on a stable solution.

3.2.3 SOM Post-Processing

After training, the finalized BMUs were computed, allowing each daily input to be assigned to a specific node. With this information, a list of days mapping to each of the nodes was generated. Subsequently, the 500 hPa geopotential height anomaly pattern for all the days in a particular node were averaged (gridpoint to gridpoint) to form a composite 500 hPa anomaly pattern, which were then plotted and compared with the other map sizes.

The four map sizes (20, 24, 30, and 35 nodes) were then compared both quantitatively and qualitatively. For each map, quantization error (QE), a measure of the average distance between an input vector and its respective node, as well as topographic error (TE), a measure of the percentage of input vectors whose BMU and "second-best"

BMU are not neighbors, as defined by the local topology [*Vesanto et al.*, 2000]. In addition, the maps were compared subjectively for similarity between nodes, progression between nodes, and physical realism. The QE differences between the four map sizes were very similar, with QE increasing slightly with increasing map size. TE differences between the map sizes were minimal. Results of these calculations can be found in Table 3.1.

Examining the maps qualitatively, the 20 node map, while having physically realistic patterns and a lack of excessive similarity between nodes (a sign of over-splitting), displayed poor progression between nodes; for example, positive or negative anomalies (associated with ridging or troughing, respectively) did not display a smooth progression that one would expect as a synoptic-scale weather system progressed eastward. This is likely caused by a lack of sufficient nodes to accommodate all patterns in the data, resulting in excessive intranode variability as dissimilar patterns are "shoehorned" into the available nodes. In contrast, the 30 and 35 node maps, while displaying excellent progression between nodes, both contain a number of nodes that appear very similar to each other, with the position and magnitude of 500 hPa geopotential height anomalies in adjoining nodes being near-identical. As mentioned previously, this is likely a sign of the SOM algorithm over-splitting representative patterns in the input data. The 24-node map, however, displays both a good progression between nodes and a lack of overly similar adjacent nodes. On this basis, the 24-node map was selected as the master SOM for all subsequent analyses. Although it has slightly higher QE than the 30-node or 35-node maps, the superior performance in the qualitative assessment more than makes up for this deficit.

Table 3.1. SOM Quality Analysis.

Map Size	Quantization Error (QE)	Topographic Error (TE)
20 nodes	25.6114	0.0420
24 nodes	25.2968	0.0422
30 nodes	24.9070	0.0470
35 nodes	24.6818	0.0436

3.2.4 Node Dynamics

While the 500 hPa geopotential height anomaly composite patterns associated with each node provide useful information about the continuum of atmospheric circulation patterns over Greenland, additional insight on the dynamics of each node was obtained by examining the composite mean sea level pressure (MSLP) pattern formed by the days mapping to a given node. Furthermore, both zonal and meridional wind anomalies, at both the $\sigma = 0.995$ level (the model surface at which air pressure is 99.5% of the surface pressure) and 500 hPa level, as well as the resultant wind anomalies were examined for each node to better understand any possible effects on surface mass balance or surface energy balance variables. All data for these analyses came from 20CRv2c.

3.2.5 Surface Energy Balance Analysis

Data for the surface energy balance analysis came from the output of regional climate model MARv3.5.2, as described in section 3.1.3. The entire spatial domain of the MAR output was used for this analysis, as it was believed that surface energy balance data for both the offshore waters would be valuable, given the findings of *Neff et al.* [2014]. The following variables were selected for analysis: cloud cover (CC), downward

shortwave radiation (SWD), downward longwave radiation (LWD), upward longwave radiation (LWU), albedo (AL), sensible heat flux (SHF) and latent heat flux (LHF). An upward shortwave radiation (SWU) variable was calculated by multiplying the SWD values by the AL values on a gridpoint basis. A net radiation (NR) variable was calculated using the following formula [*Hartmann*, 1994], also on a gridpoint basis:

$$NR = (SWD - SWU) + (LWD - LWU) \quad (3.1)$$

For each variable, a climatology was constructed in the same manner as was done for the 500 hPa geopotential height data (see section 3.2.1), with the result being daily anomalies for each variable. Each daily anomaly output was then grouped using the same list of nodes used to group the 500 hPa geopotential height data. Composite anomaly patterns were then constructed for each node using the procedure described in section 3.2.3.

3.2.6 Surface Mass Balance Analysis

Data for the surface mass balance analysis also came from output of regional climate model MARv3.5.2. The following variables were used: snowfall (SF), rainfall (RF), meltwater production (ME), sublimation/evaporation (SU), runoff (RU), refreezing (RZ), and surface mass balance (SMB). As this analysis was focused only on the ice sheet, the ice sheet mask (MSK) provided with the MAR data was used to mask the output of all of the above variables; grid cells containing less than 50% ice sheet by area were masked and excluded from the analysis. The 50% threshold was chosen based on previous work by *Fettweis et al.* [in press]. Following *Mioduszewski et al.* [2016], data points with a value of <1 millimeters water equivalent/day (mmWE/day) were recoded to

zero due to MAR's rounding of output from floating points to integers. Following these initial pre-processing steps, the same procedure used for the surface energy balance variables (section 3.2.6) was also used for the surface mass balance variables.

3.2.7 Node Persistence and Transition Analysis

To examine how the atmospheric circulation evolves over time, the SOM's BMUS output (a list of which days mapped to which node, listed in chronological order from 1 June 1900 to 31 August 2014) was analyzed to determine the node(s) that occur(s) the day after a given node. An analysis like this one was previously performed by *Schuenemann et al.* [2009]. For each node, the following was determined: percentage of days in which the circulation stayed in the same node (i.e., "persistent"), the percentage of days in which the circulation shifted to a neighboring node, that is, one located directly adjacent to the node in question, either vertically, horizontally, or diagonally (i.e., "neighbor"), and the percentage of days in which the circulation shifted to a non-neighboring node (i.e., "non-neighbor"). This allowed more persistent nodes to be identified and compared with more transient nodes. To further explore this topic, the most common transition patterns for each node were also determined. For a given node, the most common endpoint node(s) and the frequency of occurrence were determined. This analysis was performed to gain insight about how the circulation evolves over the course of the summer months.

3.2.8 Node Frequency Analysis

While examining the continuum of summer atmospheric circulation patterns over Greenland, the patterns in the values of the surface variables associated with each circulation pattern, and the evolution of the synoptic pattern over short time scales are informative, perhaps the most informative analysis is the change in frequency of each circulation pattern with time, as this allows long-term climatic changes to be detected. As such, the frequency of occurrence of each node over the entire period of the study (1900–2014) was analyzed using both raw data and a 5-year running mean. While this can help in visualizing trends over time, a more rigorous method was used to determine if these changes were statistically significant at the 95% confidence interval. To do so, a binomial distribution is constructed, following the methods of *Cassano et al.* [2007] and *Mioduszewski et al.* [2016], and a test statistic is used to determine whether to reject the null hypothesis (there is no significant difference between the frequencies of occurrence for the two periods being compared). This test statistic assumes the processes in question are random, binominal and independent [*Cassano et al.*, 2007; *Mioduszewski et al.*, 2016]. The test statistic is:

$$\left| \frac{(p_1 - p_2)}{\sqrt{\frac{p_1(1-p_1)}{\frac{n_1}{3}} + \frac{p_2(1-p_2)}{\frac{n_2}{3}}}} \right| \tag{3.2}$$

where p_1 and p_2 are the frequency of occurrence of a given node during the time periods of interest, while n_1 and n_2 are the number of records (days) in each time period. Each of the two addends below the radical are estimators of node frequency variance [*Cassano et al.*, 2007; *Mioduszewski et al.*, 2016]. If the value of the test statistic exceeds 1.96 (the critical value at the 95% confidence level), the difference in frequency between the two

data sets is statistically significant and the null hypothesis is rejected [*Cassano et al.*, 2007; *Mioduszewski et al.*, 2016].

In order to account for persistence of a given node (autocorrelation) in the time series (i.e., the circulation above Greenland remains in the same state for multiple days), the method of *Mioduszewski et al.* [2016] and *Mattingly et al.* [2016] was used, dividing the values of both n_1 and n_2 by 3 before computation of the test statistic, which reduces the degrees of freedom in the calculation while also raising the value needed to achieve statistical significance [*Mattingly et al.*, 2016; *Mioduszewski et al.*, 2016]. The value of 3 was empirically determined by identifying the length of every multi-day "run" (the occurrence of the same node over two or more consecutive days in the climatology) and then calculating the mean duration (in number of days) of such runs. The value obtained (2.9 days) was then rounded to 3 in order to ensure a conservative threshold for statistical significance, as described by *Mattingly et al.* [2016].

This statistical test was then used to determine if there were statistically significant changes in node frequency between the 20th Century (1900–2000) and the 21st Century (2001–2014). In addition, the following decadal periods were tested to determine if statistically significant changes in nodes frequency occurred during the early 20th Century warm period: 1910–1919 vs. 1920–1929, 1920–1929 vs. 1930–1939, 1930–1939 vs. 1940–1949.

3.3 Summary

Using 500 hPa geopotential height from the 20CRv2c reanalysis, this study classified the summer atmospheric circulation above Greenland and adjacent oceans for the years 1900–2014 into 24 synoptic types using self-organizing maps. Additional

insights on the dynamics of each type (node) were obtained by examining composite MSLP patterns, as well as composite zonal, meridional, and resultant winds (at both the $\sigma = 0.995$ model level and the 500 hPa pressure level). A surface energy balance analysis was then performed by examining composite patterns of cloud cover, albedo, and both radiative and non-radiative fluxes for each node using data from MARv3.5.2, forced by 20CRv2c. This process was then repeated for surface mass balance variables. The temporal evolution of the atmospheric circulation was then examined by comparing the percentage of time that the circulation remained in each node after one day vs. transitioning to another node; the most common endpoint nodes for a given node were also determined. Lastly, the frequency of each node during 1900–2014 was analyzed, and changes in node frequency over both decadal and multi-decadal periods were tested for statistical significance.

CHAPTER 4

RESULTS AND DISCUSSION

This chapter examines the results of the analyses described in Chapter 3. The composite 500 hPa geopotential height anomalies for each of the 24 synoptic types (nodes) are first examined, followed by an analysis of the composite MSLP, zonal, meridional, and resultant wind anomalies for each of the nodes. The physical implications of these anomalies for both surface energy balance and surface mass balance are also discussed. Composite anomalies of surface energy balance for each node are then examined, with discussion of the physical implications of these anomalies on GrIS surface mass balance. The composite anomalies for each surface mass balance variable are examined and compared both with each other and with the composite surface energy balance anomalies. Node persistence and transition patterns are then discussed, with insights on the temporal evolution of the 500 hPa circulation over a multi-day period. Lastly, changes in node frequency over the entire study period (1900–2014), as well as over several decadal periods, and statistically significant changes are noted.

4.1 Summer (JJA) 500 hPa Synoptic Climatology Overview

As described in Chapter 3, the 24-node map size was chosen as the master SOM after several quantitative and qualitative tests. The master SOM, used for all subsequent analyses, is shown in Figure 4.1. Examining the 500 hPa geopotential height anomaly

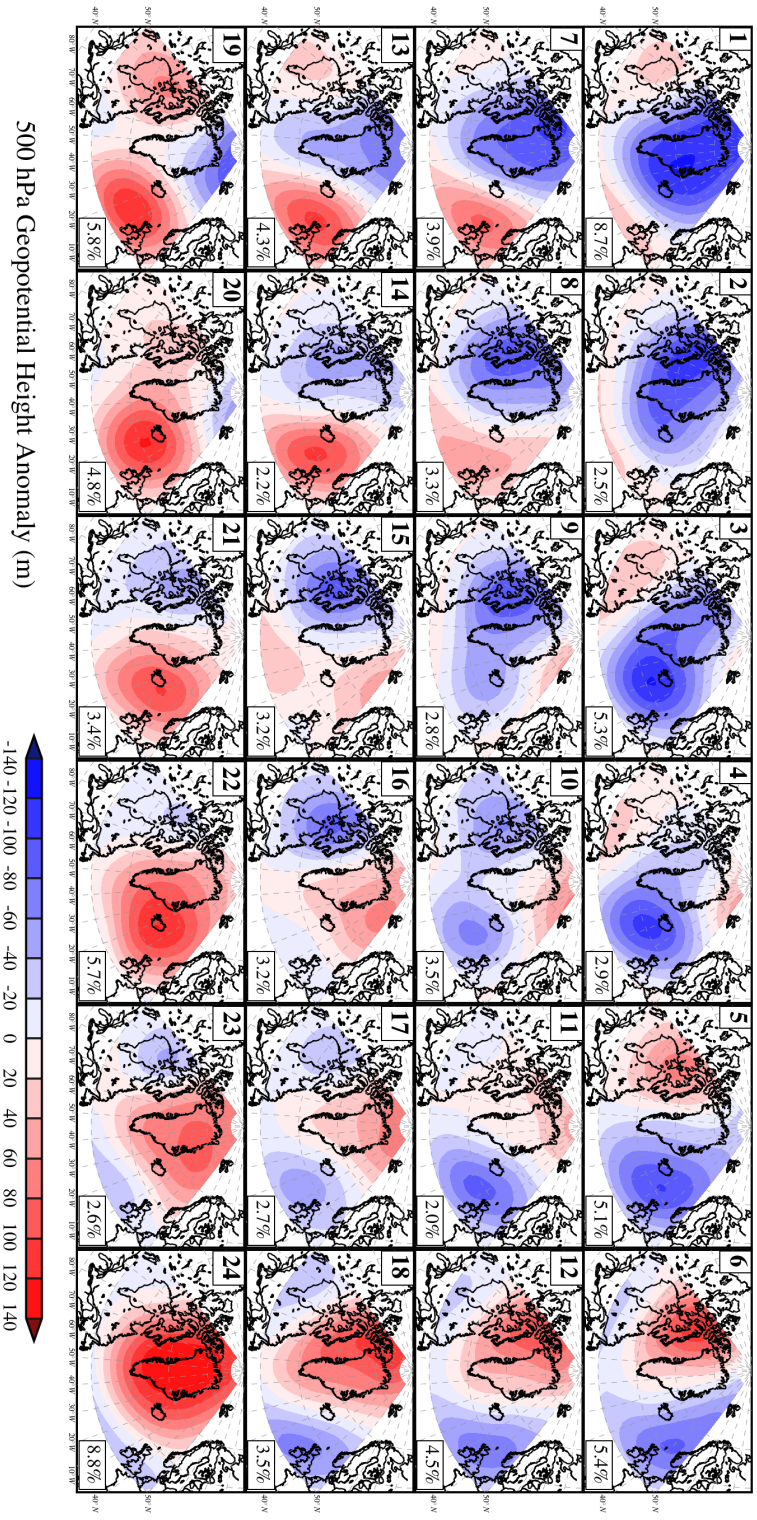

Figure 4.1. Master SOM of 1900–2014 summer (JJA) 500 hPa geopotential height anomalies (from the 20CRv2c reanalysis) over the study domain. The frequency of occurrence of each node during the study period 1900–2014 is indicated in the lower right-hand corner of each node composite.

patterns across the master SOM, one can see a wide range of conditions, from the strong negative anomalies over the GrIS in node 1, to the strong positive anomalies over the GrIS in node 24. As expected, these two opposing patterns are located at opposite corners of the map. Lining the edges of the map are other nodes characterized by strong anomalies (positive or negative). Interior nodes (8–11, 14–17) tend to feature less amplified patterns with generally weaker anomalies.

The first row of the SOM (nodes 1–6) is dominated by negative anomalies (especially node 1), except for node 6, which is nearly evenly divided between positive and negative anomalies. Moving from node 1 to node 6, the center of the negative anomaly moves from directly over Greenland (node 1) to directly south of Iceland (nodes 3–4) to the vicinity of the Norwegian Sea (node 6). Moving down the rightmost columns of the SOM, the magnitude of the negative anomalies is reduced and positive anomalies becomes increasingly dominant, with the positive anomalies in nodes 22–24 covering most of the domain. The bottom row of the SOM is also dominated by positive anomalies, although as one moves from right to left across the bottom row, the center of the positive anomaly shifts from directly over Greenland (node 24) to positions centered roughly near Iceland (nodes 20–22), to just offshore of Scotland (node 19). Moving up the three leftmost columns in the SOM, the positive anomalies are again gradually replaced by negative anomalies.

To illustrate the similarity between an individual daily 500 hPa geopotential height anomaly pattern and the node it maps to, the daily 500 hPa geopotential height anomaly map for 11 July 2012 (the day a temperature of 2.2 °C was recorded at Summit, see Chapter 1), as well as the composite 500 hPa geopotential anomaly for node 23 (the

node this day mapped to), are shown in Figure 4.2. The placement of positive and negative 500 hPa geopotential height anomalies are similar in both the node composite and the 11 July 2012 data, with positive height anomalies over Greenland, and negative height anomalies over eastern Canada and the British Isles. The magnitude of both positive and negative anomalies is smaller in the node composite than the 11 July 2012 daily data, as the node composite is the grid point average of the 283 days that mapped to the node, reducing the influence of extreme values.

To further examine the circulation patterns depicted in the SOM, the MSLP anomalies for all the days mapping to a given node of the master SOM were averaged to obtain the composite MSLP anomaly pattern associated with each node; these composites are shown in Figure 4.3. The MSLP anomalies correspond extremely well with the 500 hPa geopotential height anomalies, both in terms of magnitude and location within the domain. These results are like those of *Mioduszewski et al.* [2016], who found a similar correspondence between 500 hPa geopotential height anomalies and MSLP anomalies. This strong correspondence is not surprising however, as the movement of the high and low pressure systems depicted in Figure 4.3 are in part dependent on the mid-tropospheric flow.

4.2 SOM Nodes and Winds

To better understand the circulation associated with each of the SOM nodes, plots of both 500 hPa zonal and 500 hPa meridional wind anomalies were created; these can be

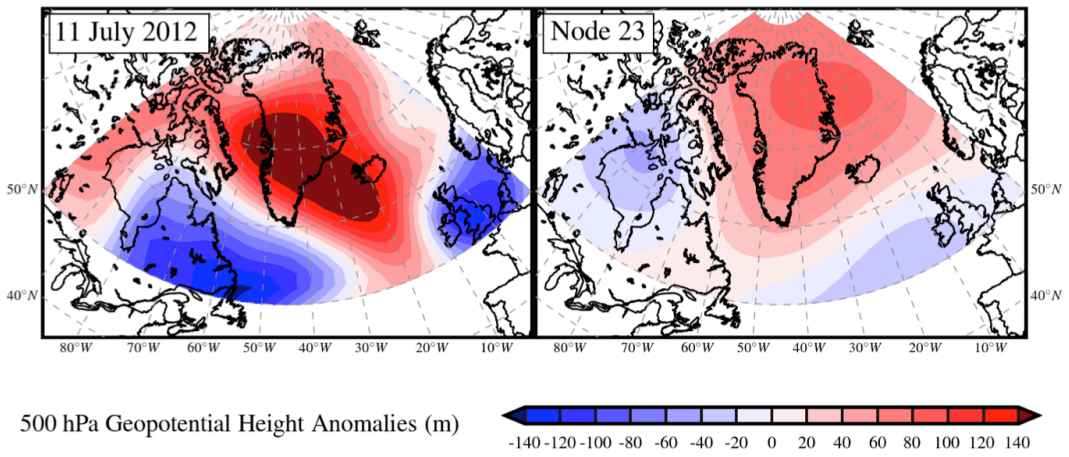

Figure 4.2. 500 hPa geopotential height anomalies for 11 July 2012 (left), composite 500 hPa geopotential height anomaly pattern for node 23 (right). 11 July 2012 is one of the 283 days composited to form the node 23 anomaly pattern.

seen in Figure 4.4 and 4.5, respectively. Examining the zonal wind anomalies, nodes 1–4 display strong positive anomalies across much of the north Atlantic, indicating abnormally strong westerly winds; as these nodes are also characterized by strong negative 500 hPa geopotential height anomalies, these winds are locally associated with the flow of the polar jet stream around the base of a trough near Greenland. As the negative 500 hPa geopotential height anomalies give way to positive 500 hPa geopotential height anomalies in nodes 5–6, the strong positive zonal wind anomalies are replaced by negative zonal wind anomalies, indicating much weaker westerlies. Next, moving down the three rightmost columns of Figure 4.4, the "interior" nodes, characterized by weaker 500 hPa geopotential height anomalies, also show generally weaker zonal wind anomalies, as one might expect with less amplified patterns. Negative zonal wind anomalies become much stronger moving from the first row (nodes 4–6) towards the bottom row (nodes 22–24). These strong negative anomalies are indicative

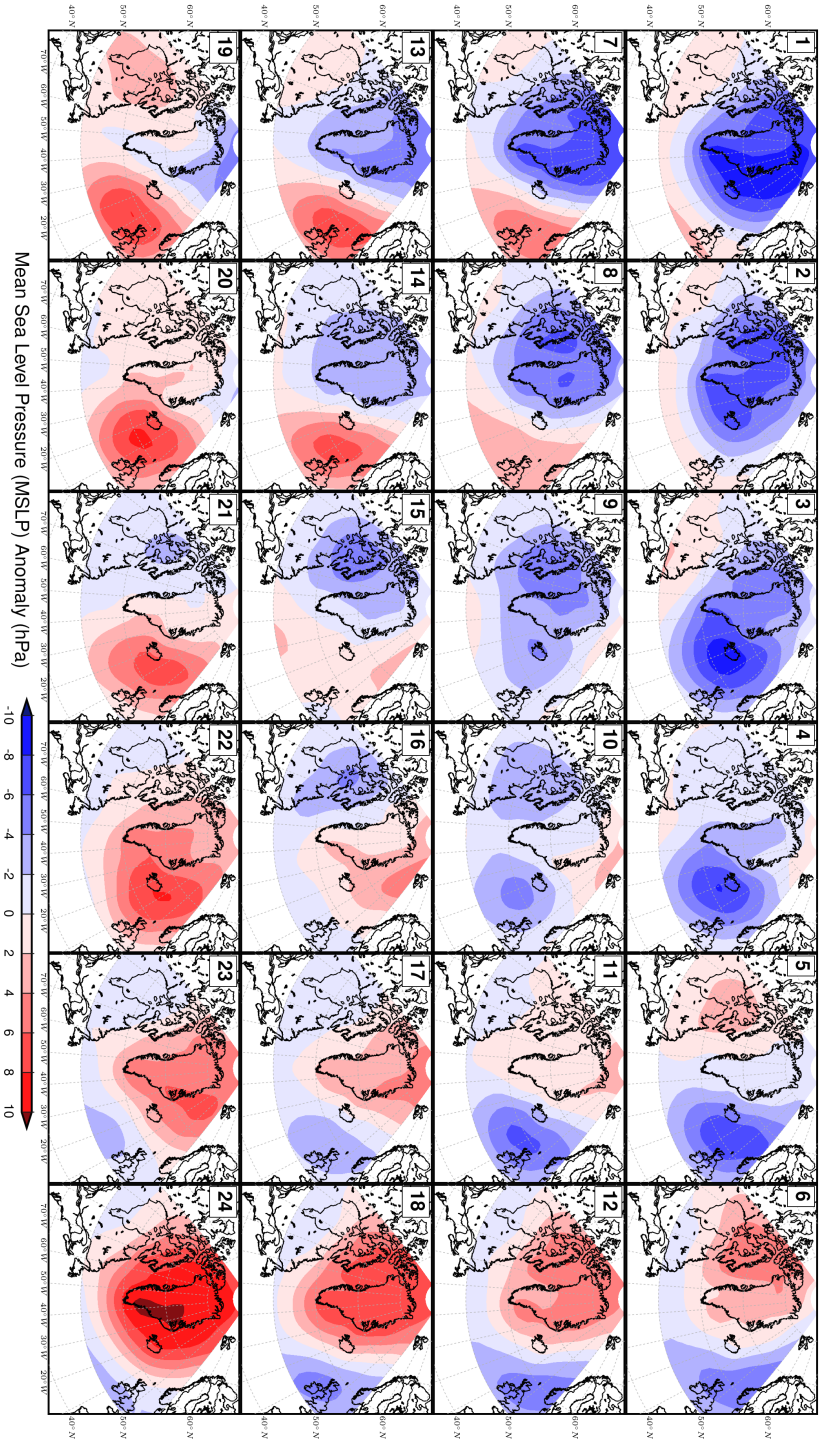

Figure 4.3. Composite MSLP anomalies from 20CRv2c for dates associated with each node of the master SOM.

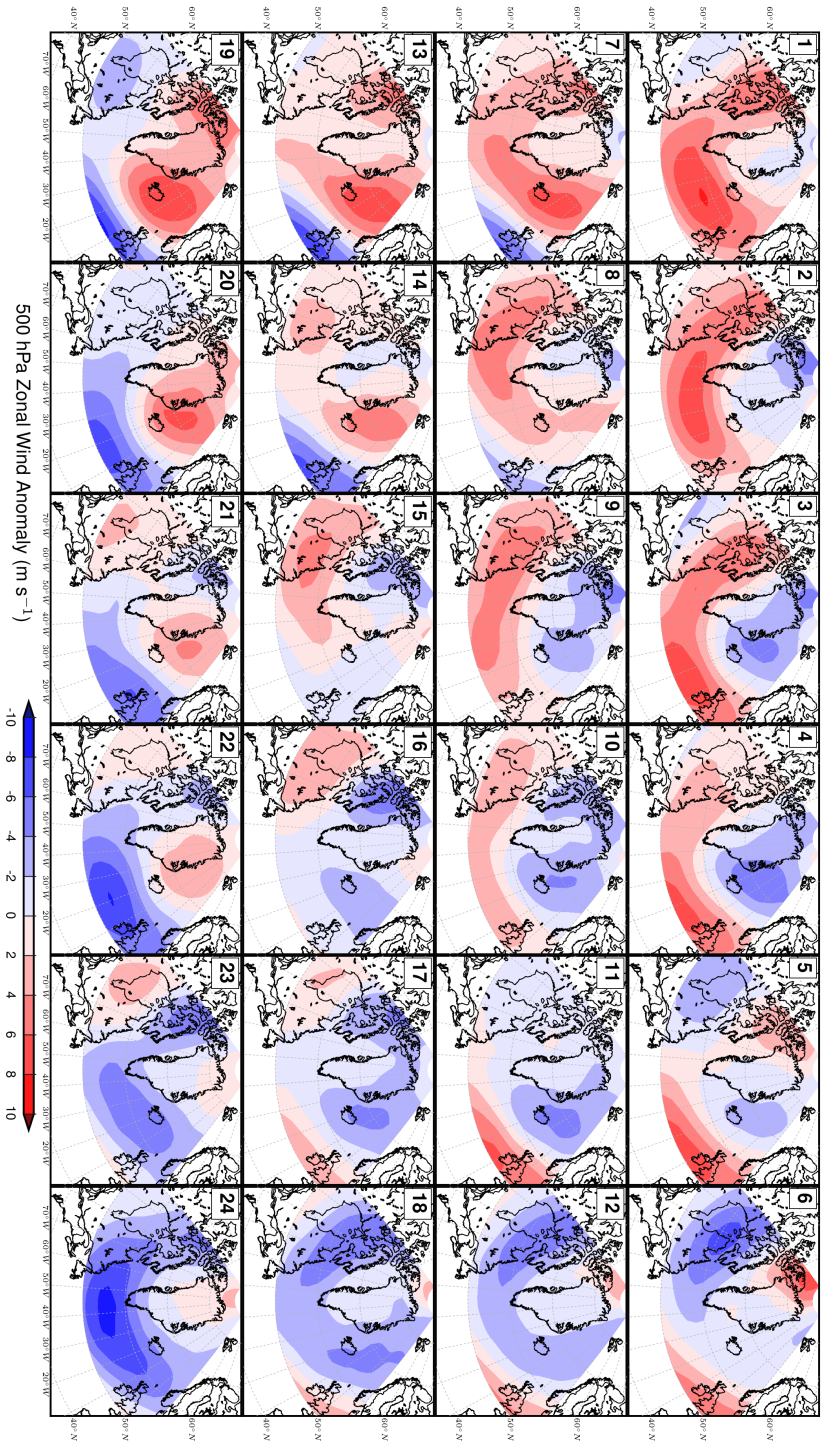

Figure 4.4. Composite 500 hPa zonal wind anomalies from 20CRv2c for dates associated with each node of the master SOM.

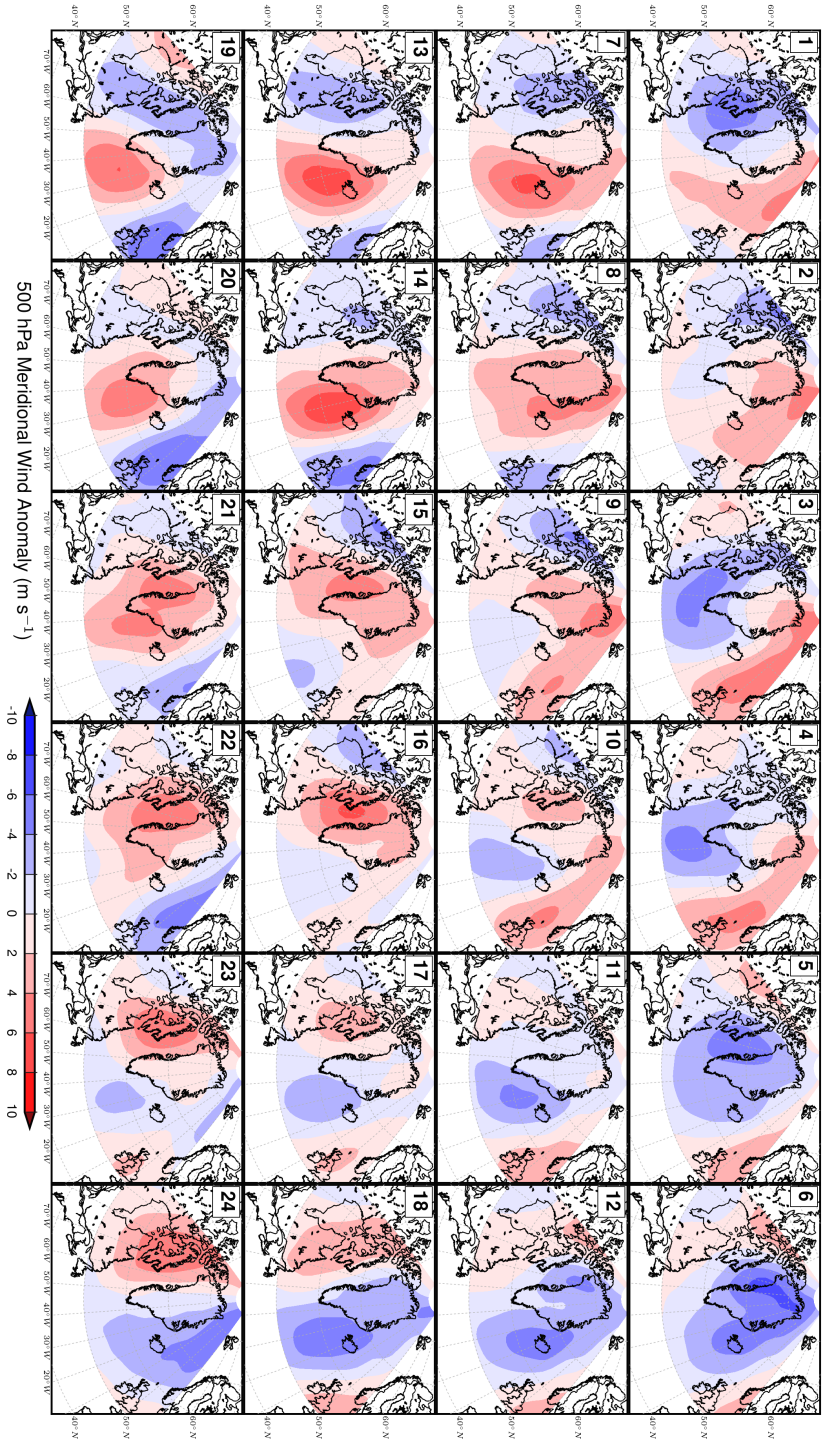

Figure 4.5. Composite 500 hPa meridional wind anomalies from 20CRv2c for dates associated with each node of the master SOM.

of weak westerlies, likely due to strong ridging over the domain and subsequent displacement of the polar jet. Moving along the bottom row from node 24 to node 19, the negative zonal wind anomalies become less dominant and are replaced by positive zonal wind anomalies near Greenland, likely due to increased troughing seen in nodes 19–21. Lastly, moving up the three leftmost columns of Figure 4.4, negative 500 hPa geopotential heights again becomes dominant, and positive zonal wind anomalies become stronger. In summary, strong negative (positive) 500 hPa geopotential height anomalies, indicative of troughing (ridging), lead to stronger (weaker) westerlies and a positive (negative) zonal wind anomaly.

The sign of the 500 hPa geopotential height anomalies is also very important in examining the meridional wind anomalies, seen in Figure 4.5. Nodes 1–4 show negative meridional wind anomalies west of Greenland, with positive meridional wind anomalies to the east, likely indicative of cyclonic flow through the base of a trough. Moving into nodes 5-6, negative meridional wind anomalies are found across much of Greenland. Moving down the three rightmost columns of Figure 4.5, positive 500 hPa geopotential height anomalies cover more of the domain, and positive meridional wind anomalies are now found west of Greenland, with the negative meridional wind anomalies to the east; this is a flow pattern opposite to that of the upper left corner, and is likely indicative of anticyclonic flow through a ridge. Moving from node 24 toward node 19, the positive 500 hPa geopotential height anomalies move eastward, with the region of positive meridional wind anomalies, signifying the ascending portion of the ridge, shifting eastward as well. Moving up the three leftmost columns to return to the top row, negative 500 hPa geopotential height anomalies become dominant, and negative meridional wind

anomalies are again seen west of Greenland, with positive meridional wind anomalies to the east. In summary, strong negative 500 hPa geopotential height anomalies, indicative of troughing, lead to cyclonic flow around Greenland, with air moving south from the Arctic Ocean over Baffin Bay and the Labrador Sea, before moving north again over the Norwegian Sea and Greenland Sea, while strong positive 500 hPa geopotential height anomalies, indicative of ridging, lead to anticyclonic flow around Greenland, with southerly flow to the west of Greenland and northerly flow to the east. The location of the geographic features mentioned above can be found in the domain map, Figure 3.3. Putting the zonal and meridional components together results to examine the resultant wind speed anomalies (shown in Figure 4.6), the cyclonic and anticyclonic flow can be seen in the nodes representing troughing and ridging, respectively.

Zonal and meridional wind anomalies were also calculated using data from 20CRv2c model sigma level 0.995 ($\sigma = 0.995$). While the 500 hPa wind anomalies allow for the examination of mid-tropospheric flow, the $\sigma = 0.995$ data has the advantage of following terrain, allowing for examination of near-surface (~42 m above ground level) circulation. Zonal and meridional wind speed anomalies at the $\sigma = 0.995$ level (not shown) are weaker in magnitude than those at the 500 hPa level, but have the same sign at most locations within the study domain. Resultant wind speed anomalies at the $\sigma = 0.995$ level are shown in Figure 4.7. Like the zonal and meridional wind speed anomalies, the resultant wind speed anomalies at the $\sigma = 0.995$ level are generally weaker than those at the 500 hPa level. Wind speed anomaly maxima at the 500 hPa level are similar in location to those at the $\sigma = 0.995$ level; the direction of the wind in these areas is also the same at both levels.

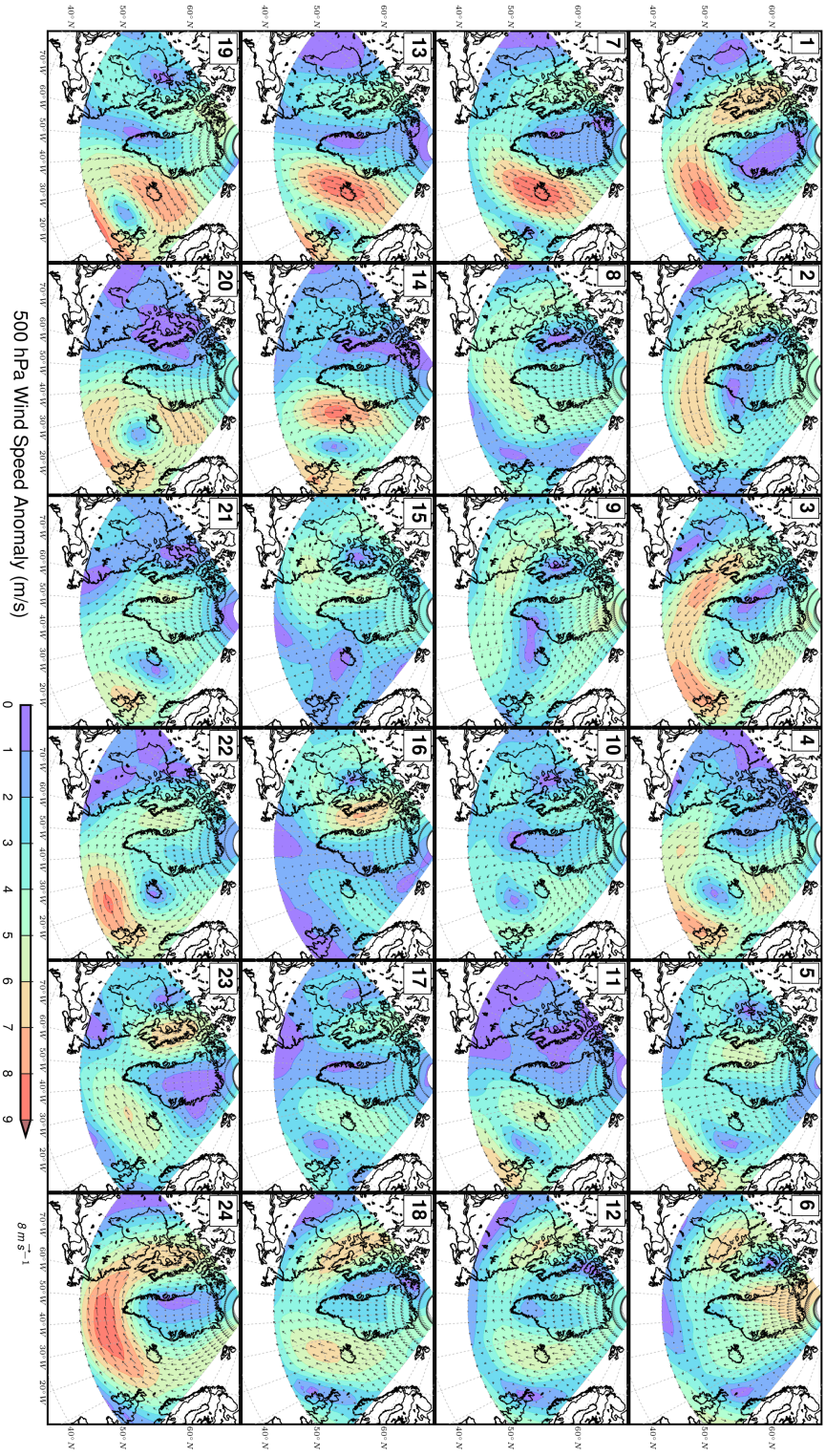

Figure 4.6. Resultant 500 hPa wind anomalies (shading) and vector anomaly, both from 20CRv2c, for dates associated with each node of the master SOM.

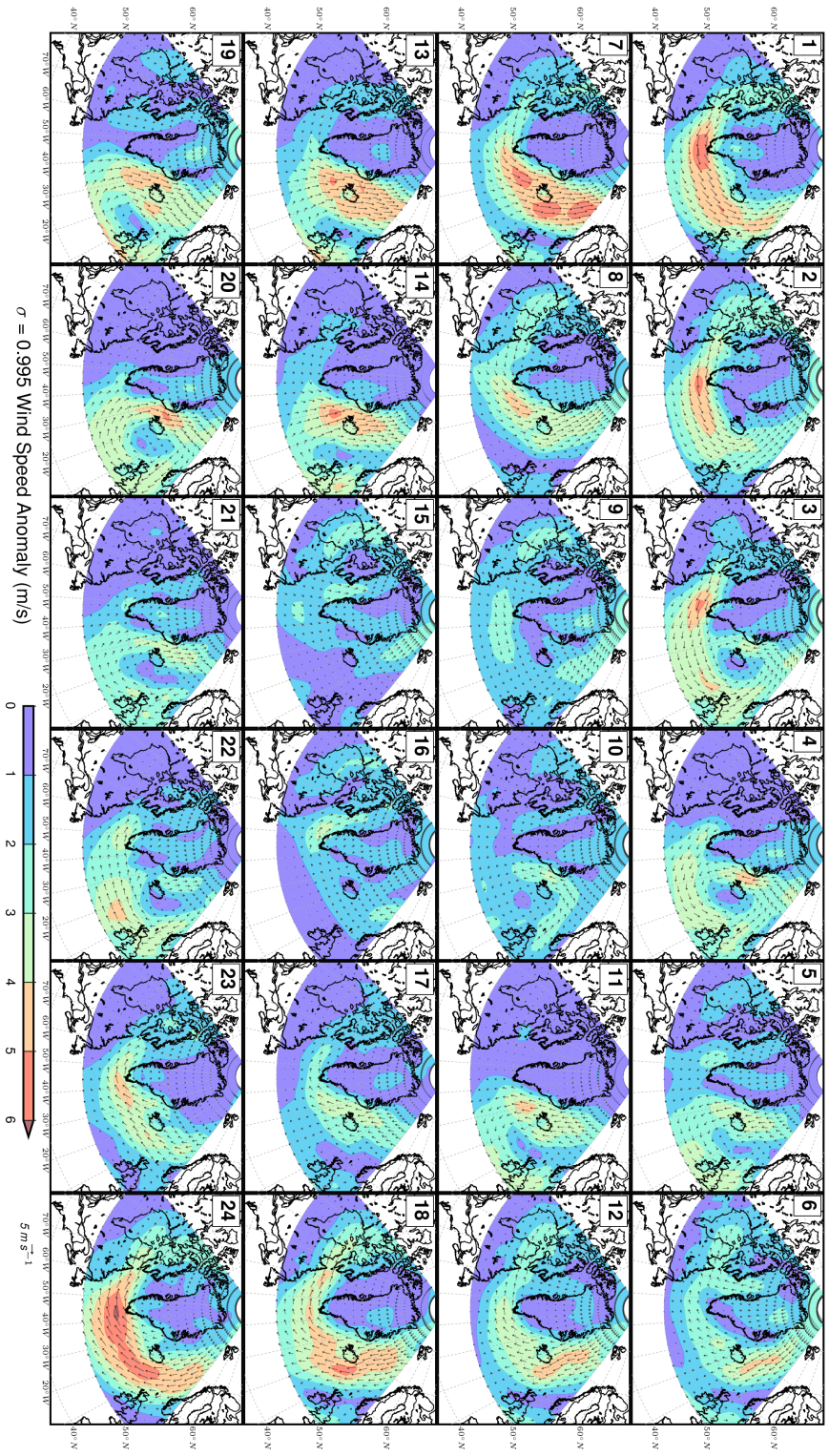

Figure 4.7. Resultant σ = 0.995 wind anomalies (shading) and vector anomaly, both from 20CRv2c, for dates associated with each node of the master SOM.

4.3 Surface Energy Balance Analysis

Having examined the continuum of summer 500 hPa geopotential height anomaly patterns near Greenland, as well as both the zonal and meridional winds associated with these patterns, the focus now turns to the "environment" portion of the synoptic climatology. In this section, anomalies related to surface energy balance are examined, including both radiative fluxes (shortwave and longwave radiation), non-radiative fluxes (sensible and latent heat flux), as well as other variables of interest (albedo, cloud cover).

4.3.1 Cloud Cover, Albedo, and Shortwave Fluxes

Cloud cover anomalies for each of the 24 nodes are depicted in Figure 4.8. Node 1, dominated by negative 500 hPa geopotential height anomalies, shows higher levels of cloud cover over the ice sheet, except for far southern Greenland, where clearer skies predominate. Moving from node 1 towards node 6, the negative 500 hPa geopotential height anomalies shift east, with the positive cloud cover anomalies shifting east as well (nodes 3–4), before becoming centered in northern Greenland (nodes 5–6), while more southern parts of the island experience clearer skies. The influence of positive 500 hPa geopotential height anomalies on cloud cover is clearly seen in nodes 23–24, where most of the study domain is dominated by ridging; this large-scale subsidence leads to negative cloud cover anomalies over most of Greenland. The sign and magnitude of the cloud cover anomaly is strongly related to vertical motion; areas of Greenland with positive cloud cover anomalies area also characterized by negative anomalies of 500 hPa omega (vertical velocity), signifying upward motion.

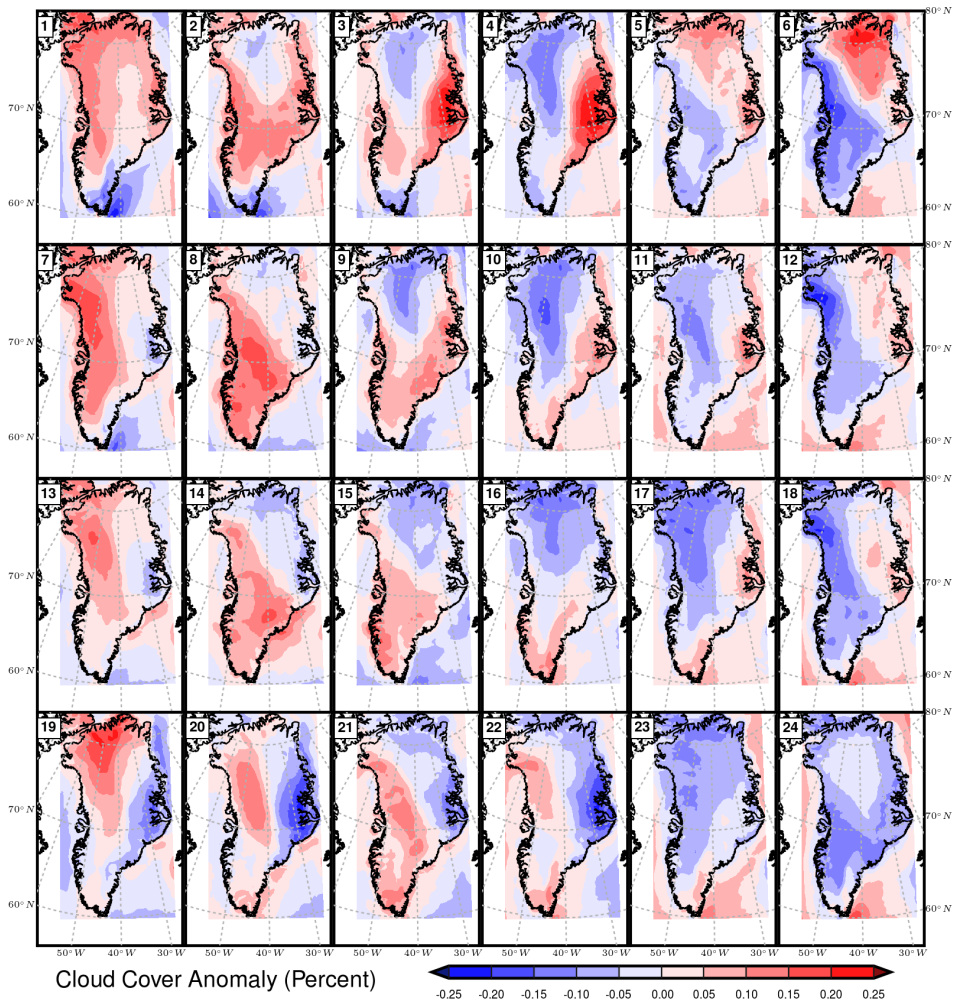

Figure 4.8. Composite cloud cover (CC) anomalies from MAR for dates mapped to each node.

In contrast, areas of Greenland with negative cloud cover anomalies are characterized by positive anomalies of 500 hPa omega, signifying downward motion. This is illustrated in Figure 4.9 for node 6. For most of the nodes in Figure 4.8, the cloud cover anomaly pattern is heterogeneous, with some areas of Greenland experiencing positive cloud cover anomalies while other areas experience negative cloud cover anomalies, showing that one circulation pattern does not create uniform conditions across the entire island.

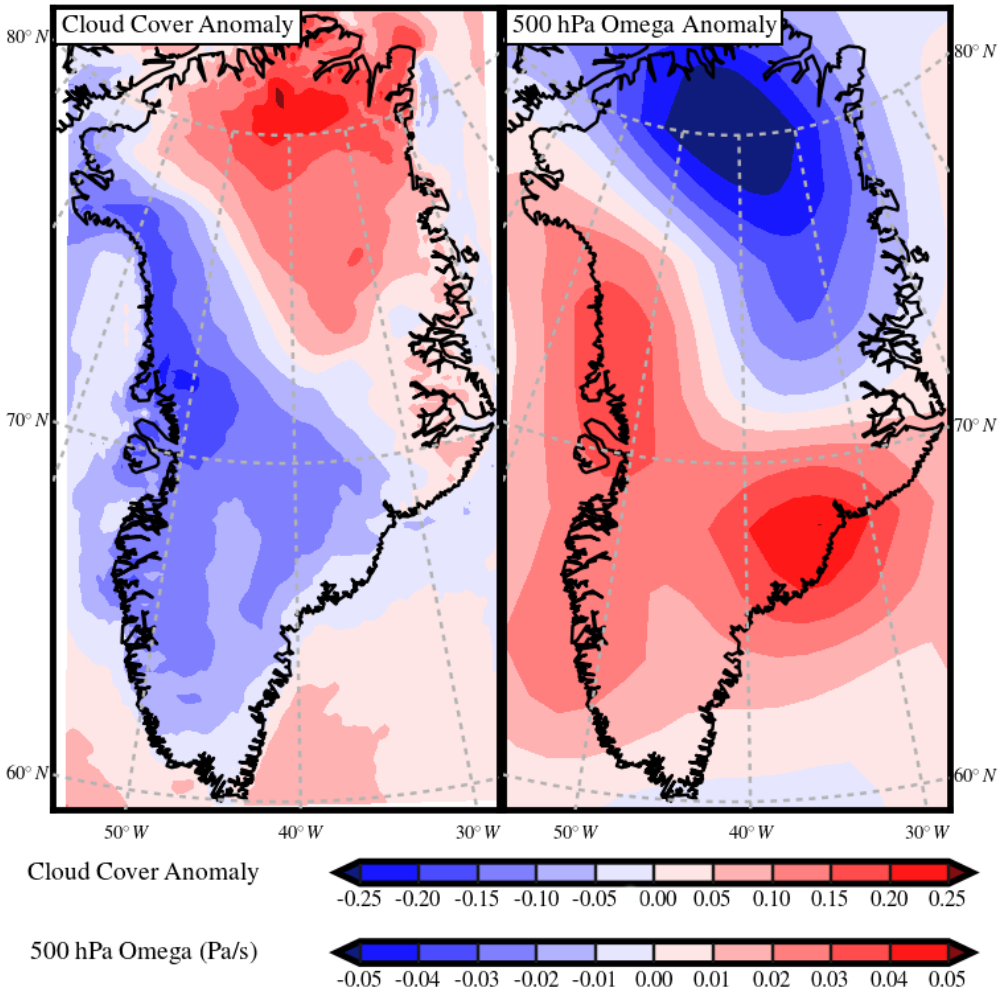

Figure 4.9. Cloud cover anomaly for node 6 from MAR (left), 500 hPa omega anomaly for node 6 from 20CRv2c (right). Negative omega values indicate upward motion.

For example, in nodes where the strongest ridging is located to the east of Greenland (nodes 19–22), only eastern portions of Greenland experience the subsidence associated with the ridge, leading to clearer skies in the east, while western Greenland experiences cloudier skies.

Cloud cover is of great importance in determining both how much shortwave radiation reaches the surface; which is key to determining surface energy balance and

thus surface temperature, as shown by *Bennartz et al.* [2013]. Focusing first on downward shortwave radiation (SWD) across the nodes (Figure 4.10), a close correspondence is seen with the cloud cover anomalies (Figure 4.8). Areas of the ice sheet with anomalously high cloud cover (such as east central Greenland in nodes 3 and 4, as well as far northern Greenland in nodes 6 and 19) display strong negative SWD anomalies, almost certainly due to optically thick clouds that greatly reduce surface insolation. The opposite effect is seen in areas with anomalously low cloud cover, such as extreme southern Greenland in nodes 1 and 2; the greatly reduced cloud cover leads to strong positive SWD anomalies. Also of note are nodes 17–18 and 23–24; with negative cloud cover anomalies present across much of Greenland; days which map to these nodes experience positive SWD anomalies across most of Greenland.

While SWD is important in surface energy balance calculations, the generally high albedo of the GrIS's snow- and ice-covered surface means much of this energy is reflected away and is not available for melt. However, the albedo of the GrIS varies seasonally; *Box et al.* [2012] found that for the years 2000–2011, GrIS albedo averaged 0.835 in April, and reached an annual minimum of 0.707 in July before rising again in August and September due to new snow accumulation. Areas in the lower elevation ablation zone, however, can sometimes have drastically lower albedos, such as the value of 0.259, measured at the JAR1 GC-Net site in July 2010 [*Box et al.*, 2012]. Albedo itself is quite variable across the nodes, as seen above in Figure 4.11. While many of the nodes only show weak anomalies, nodes with strongly negative 500 hPa geopotential height anomalies (nodes 1, 2, 7, 8) display strong positive albedo anomalies along Greenland's west coast, likely due to onshore flow of moist maritime air, with subsequent orographic

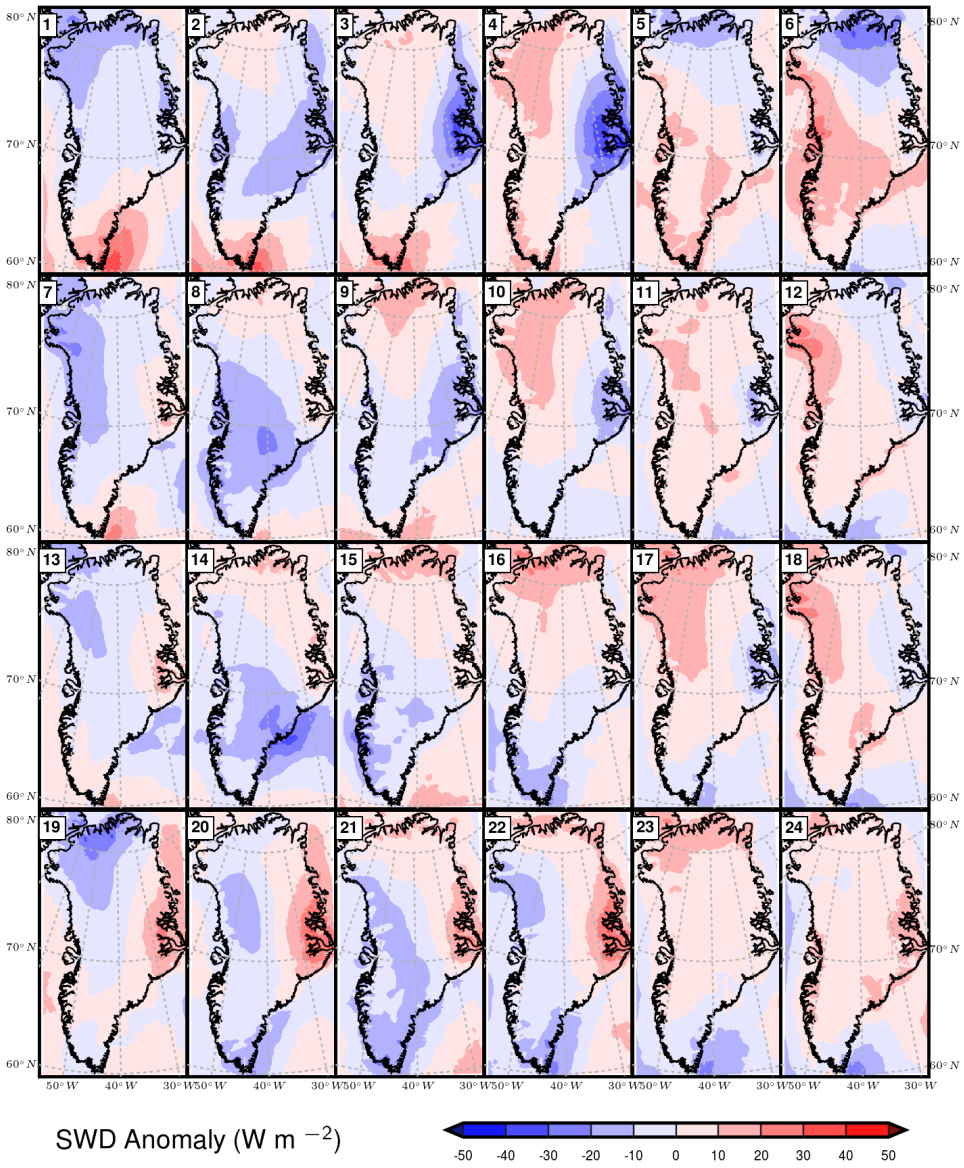

Figure 4.10. Downward shortwave radiation (SWD) anomalies from MAR for dates mapped to each node.

lift, adiabatic cooling, and finally precipitation, likely as snow. The high albedo of freshly-fallen snow, with values as high as 0.9 [*Hartmann*, 1994], likely leads to the positive albedo anomalies. The positive albedo anomalies in east central Greenland, seen in nodes 3 and 4, as well as far northern Greenland (node 19), are likely due to the same mechanism; strong MSLP anomalies just offshore (see Figure 4.3) likely represent

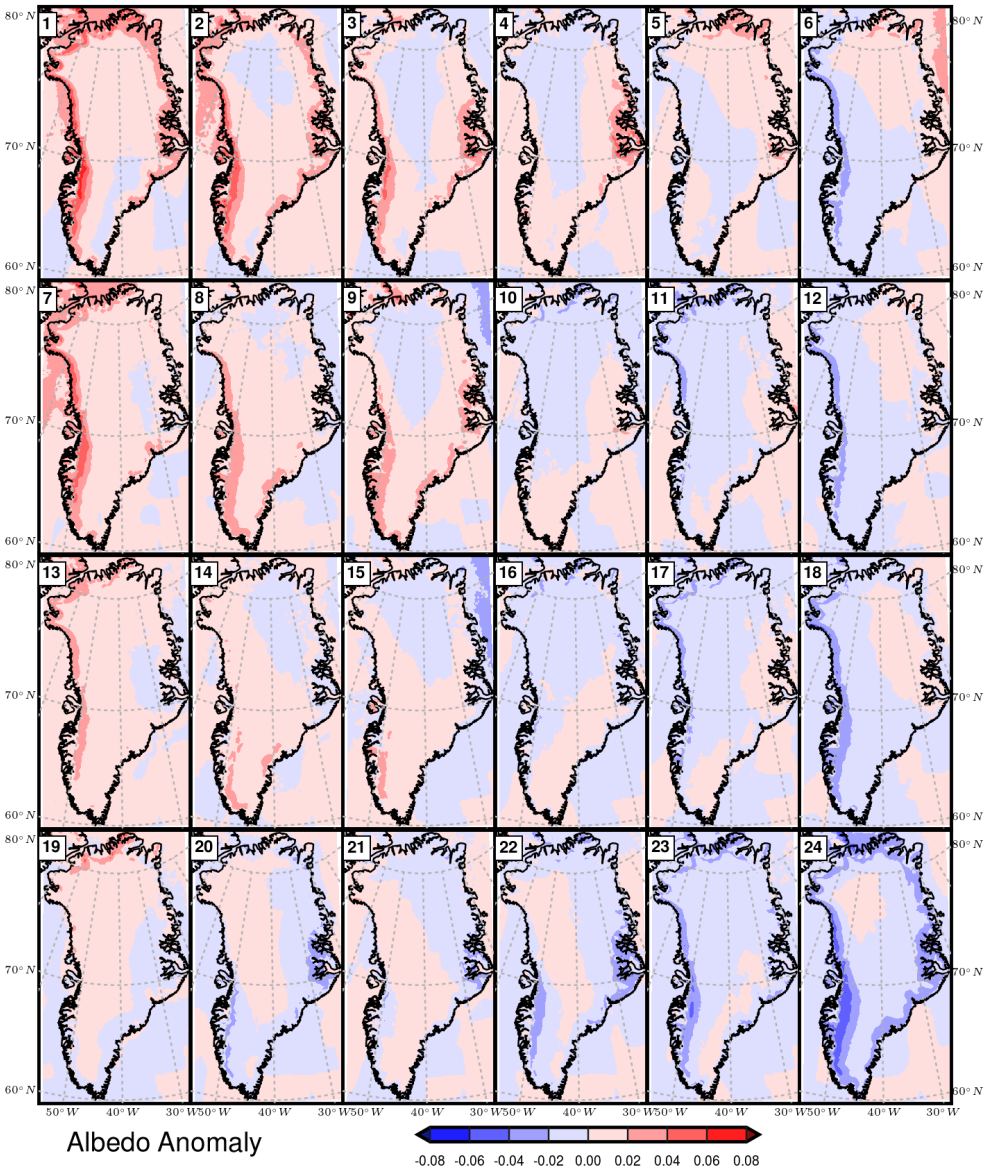

Figure 4.11. Composite albedo (AL) anomalies from MAR for dates mapped to each node.

passing cyclones that act to advect moisture onshore. On the other hand, nodes dominated by strong positive 500 hPa geopotential height anomalies, such as nodes 22–24, show strong negative albedo anomalies. As these nodes show reduced cloud cover, this negative albedo anomaly is likely caused by snowmelt and for areas in the ablation zone, exposure of bare ice, which may have a much lower albedo than the snow above it.

While freshly-fallen snow can result in a relatively quick increase in surface albedo in the region of Greenland where it falls, the circulation patterns associated with strong negative albedo anomalies (node 18, as well as nodes 22–24) would likely result in much slower changes to albedo. These anomalies may instead be due to long-term changes in albedo over the 1900–2014 study period, as well as more frequent occurrence of nodes that favor negative albedo anomalies. The average summer (JJA) albedo of the GrIS form 1900-2014, calculated from MARv3.5.2 (forced by 20CRv2c), is shown in Figure 4.12. A steady decline in albedo is seen from the mid-1990s onward, although 2013 showed albedo values more characteristic of the 20th Century compared to the more extreme years of 2010 and 2012. Also of note is the sharp decline in albedo from the mid-1920s to the mid-1930s, coincident with the early 20th Century warm period. This declining albedo trend in recent decades may also be due to a statistically significant increase in frequency of node 24 (from 8.1% to 14.6%) during the 21st Century (2001–2014) compared to the 20th Century (1900–2000), as discussed in section 4.5. Node 24 also has the greatest positive meltwater production anomalies of any node (discussed further in section 4.4). The increasing frequency of this high-melt node during the 21st Century is likely leading to the lower albedo values observed during this period (Figure 4.12). In addition, the period 2001–2014 contains 20.0% of all days mapping to node 24, despite accounting for only 12.2% of the 1900-2014 climatology. This results in a node average that contains a disproportionate number of days from the 2001-2014 period, when albedos were generally lower than the 1900–2014 average. This may lead to a node average with stronger negative anomalies than one would expect from short-term processes alone.

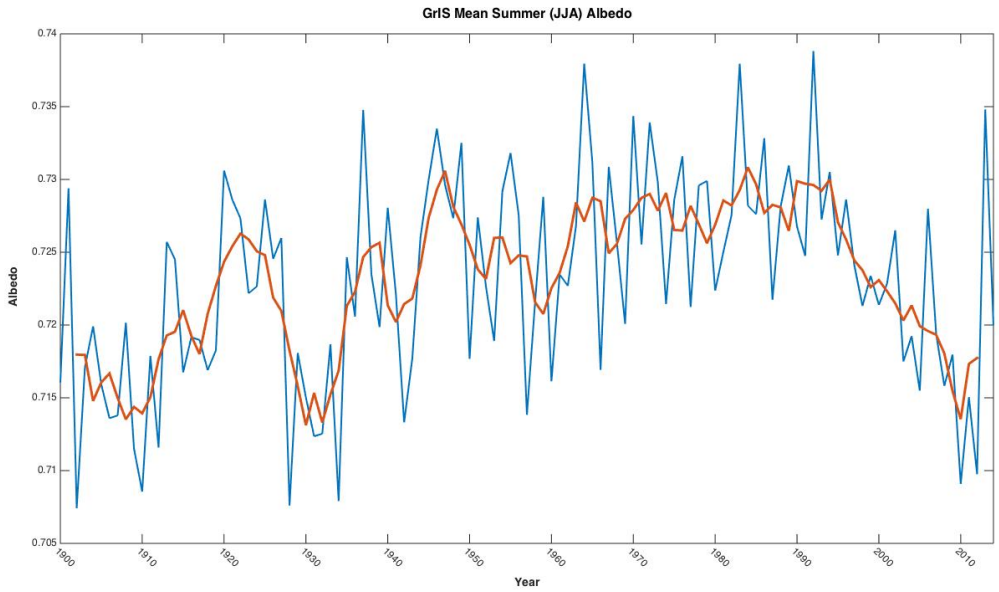

Figure 4.12. Mean summer (JJA) albedo from MAR for the GrIS from 1900–2014. Individual summer season means are depicted in blue; a 5-year running mean is depicted in red.

As described in Chapter 3, values for upward shortwave radiation (SWU) were calculated by multiplying each daily albedo value output from MAR (on a gridpoint basis) by the corresponding SWD value. SWU anomalies were then calculated as done previously for SWD and other surface energy balance variables. The distribution of SWU anomalies across the nodes is shown in Figure 4.13. The SWU anomalies broadly resemble the SWD anomalies, which is not surprising in that the SWU data is itself derived from the SWD data. Areas with negative SWD anomalies have a reduced incoming shortwave flux, and thus less outgoing shortwave flux, assuming constant albedo. For example, while nodes 3 and 4, where fresh snowfall is likely present along Greenland's east coast, one may expect a positive SWU anomaly due to the higher surface albedo, but optically thick clouds greatly reduce the incoming shortwave flux, resulting in anomalously low SWU despite the increase in albedo. However, this may not always be the case. Node 24, for example is characterized by positive SWD anomalies in

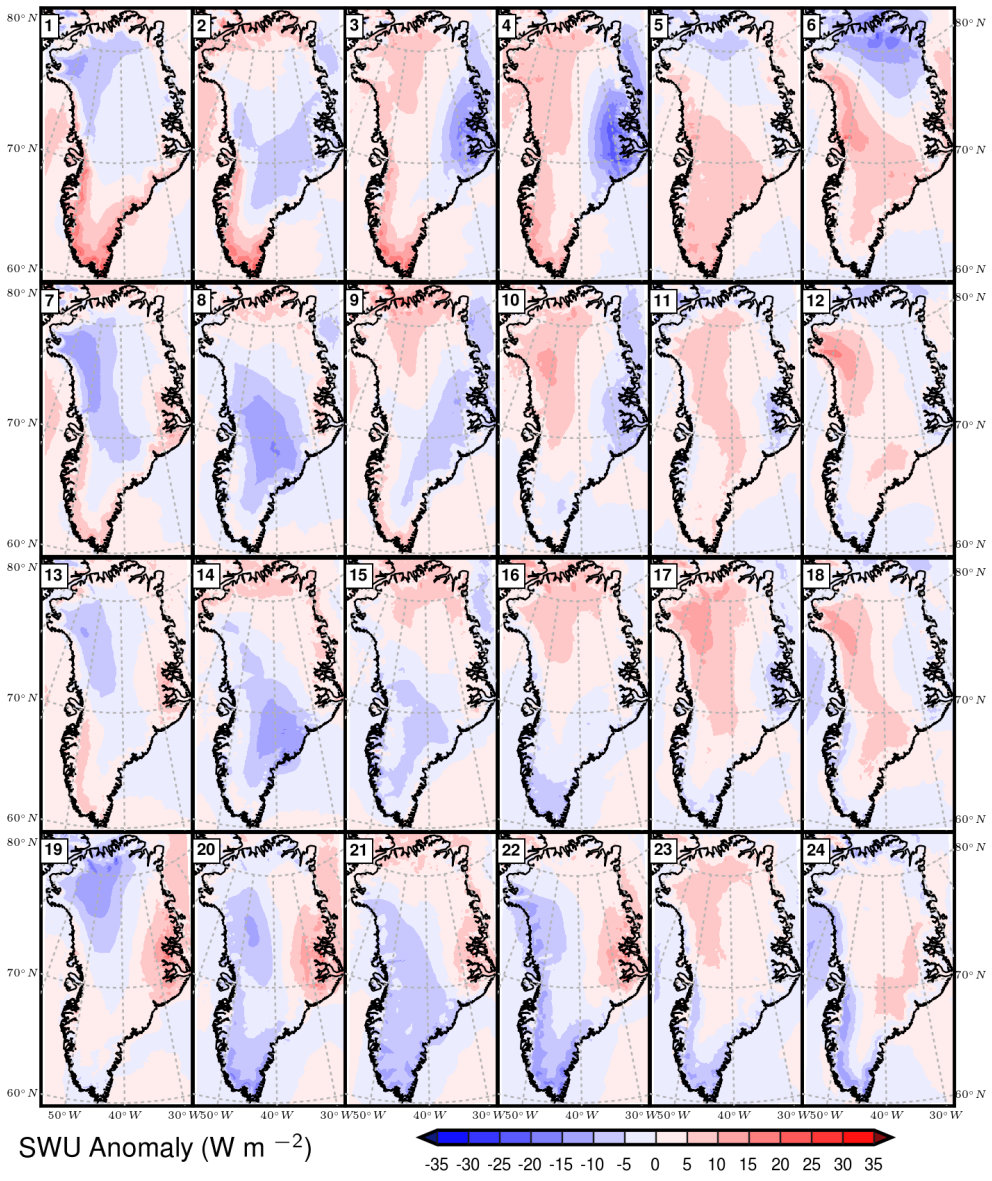

Figure 4.13. Composite upward shortwave radiation (SWU) anomalies, derived from AL and SWD data from MAR, for dates mapped to each node.

southwestern Greenland, but negative SWU anomalies in the same region. While one might expect the SWU anomalies to be positive as well given the increased SWD seen with this pattern, the albedo anomalies for node 24 are strongly negative in southwestern Greenland, likely due to melting snow and bare ice exposure. A similar effect occurs in node 2, which has negative SWD anomalies along the central western coast, but positive

SWU anomalies in the same region, likely due to sharply increased albedo from fresh snowfall. This suggests that a large enough change in albedo can alter the usual correspondence between SWU and SWD anomalies. If the magnitude of the SWD anomaly is rather small, a large change in albedo may be enough to change the sign of the SWU anomaly (such as in nodes 2 and 24). Conversely, stronger SWD anomalies with weaker albedo changes (such as nodes 3 and 4) result in the sign of the SWU anomaly remaining consistent with the sign of the SWD anomaly; the change in albedo is not enough to change the sign of the anomaly.

4.3.2 Longwave Fluxes

To fully examine the radiative portion of the surface energy budget, longwave fluxes were also examined. The downward longwave radiation flux (LWD) is dependent on multiple variables, including greenhouse gas concentration (water vapor and carbon dioxide), air temperature (through the Stefan-Boltzmann relation), as well as cloud cover and cloud type/height; a lower elevation stratus cloud is warmer than high elevation cirrus and thus will emit more longwave radiation [*Oke*, 1987]. Figure 4.14 shows the LWD anomaly patterns across the nodes. In some nodes, air temperature seems to have a stronger influence on the sign of the LWD anomaly than cloud cover, likely due to the presence of a strong air temperature anomaly. For example, node 1, while having strong positive cloud cover anomalies across much of Greenland, displays negative LWD anomalies, likely due to the anomalously cold 3-m temperatures present across most of Greenland in this node (not shown). Extreme southern Greenland, in contrast to the rest of the island, has negative cloud cover anomalies in node 1, which when combined with

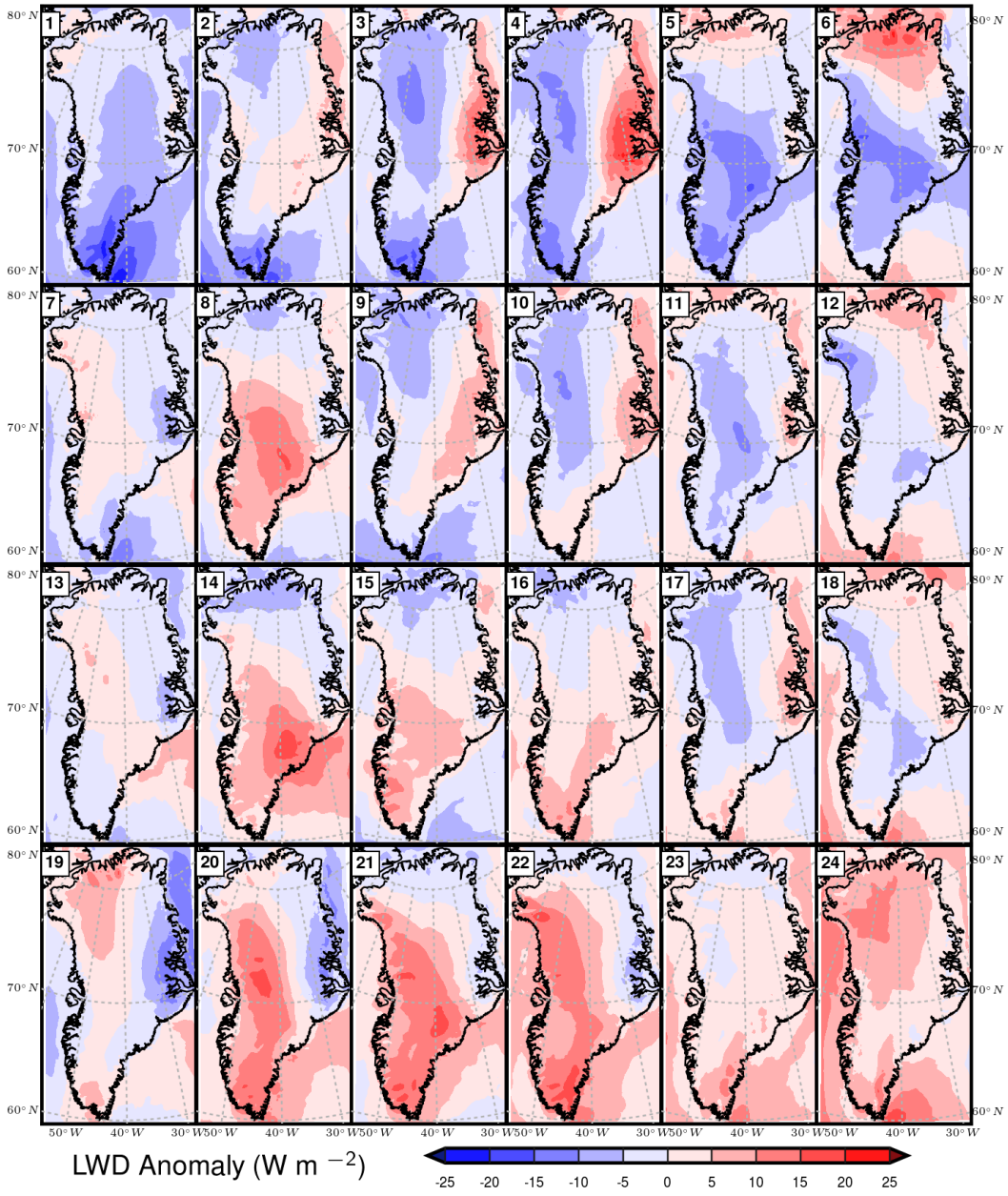

Figure 4.14. Composite downward longwave radiation (LWD) anomalies from MAR for dates mapped to each node.

cold temperatures, results in a stronger negative LWD anomaly than seen elsewhere. A similar effect can be seen with warmer temperatures as well. Node 24, with negative cloud cover anomalies across Greenland, nonetheless shows positive LWD anomalies,

likely due to the anomalously warm 3-m temps present across Greenland in this node (not shown). Other nodes, such as nodes 4, 6 and 10-12, where 3-m temperature anomalies are much weaker, show a much closer correspondence between cloud cover and LWD anomalies; areas with positive (negative) cloud cover anomalies also show positive (negative) LWD anomalies. Nodes that appear quite similar in both the master SOM and the cloud cover anomalies, such as nodes 7 and 8, have very different LWD anomaly patterns; while the positive cloud cover anomaly in node 7 corresponds with only a weak positive LWD anomaly, the positive cloud cover anomaly in node 8 is associated with strong positive LWD anomalies. The same pattern occurs with node 13 and node 14. This is likely since positive 3-m temperature anomalies are present in both nodes 8 and 14, over the same regions where strong positive LWD anomalies are seen. Nodes 7 and 13 lack these areas of positive 3-m temperature anomalies. Difference in cloud types/height and or atmospheric moisture transport into the interior of the ice sheet, may also play a role.

In contrast to the LWD anomalies, upward or outgoing longwave radiation (LWU) anomalies, seen in Figure 4.15, are more spatially homogeneous. As LWU is directly proportional to surface temperature via the Stefan-Boltzmann law, LWU can be thought of as a proxy of sorts for surface temperature. Indeed, the spatial pattern of LWU anomalies strongly resembles that of surface temperature anomalies, both in magnitude and sign (not shown). Nodes dominated by negative 500 hPa geopotential height anomalies (troughing), such as nodes 1–3, show strong negative LWU anomalies, while those dominated by positive 500 hPa geopotential height anomalies (ridging), such as nodes 22–24, show strong positive anomalies. These anomalies are easily explained by

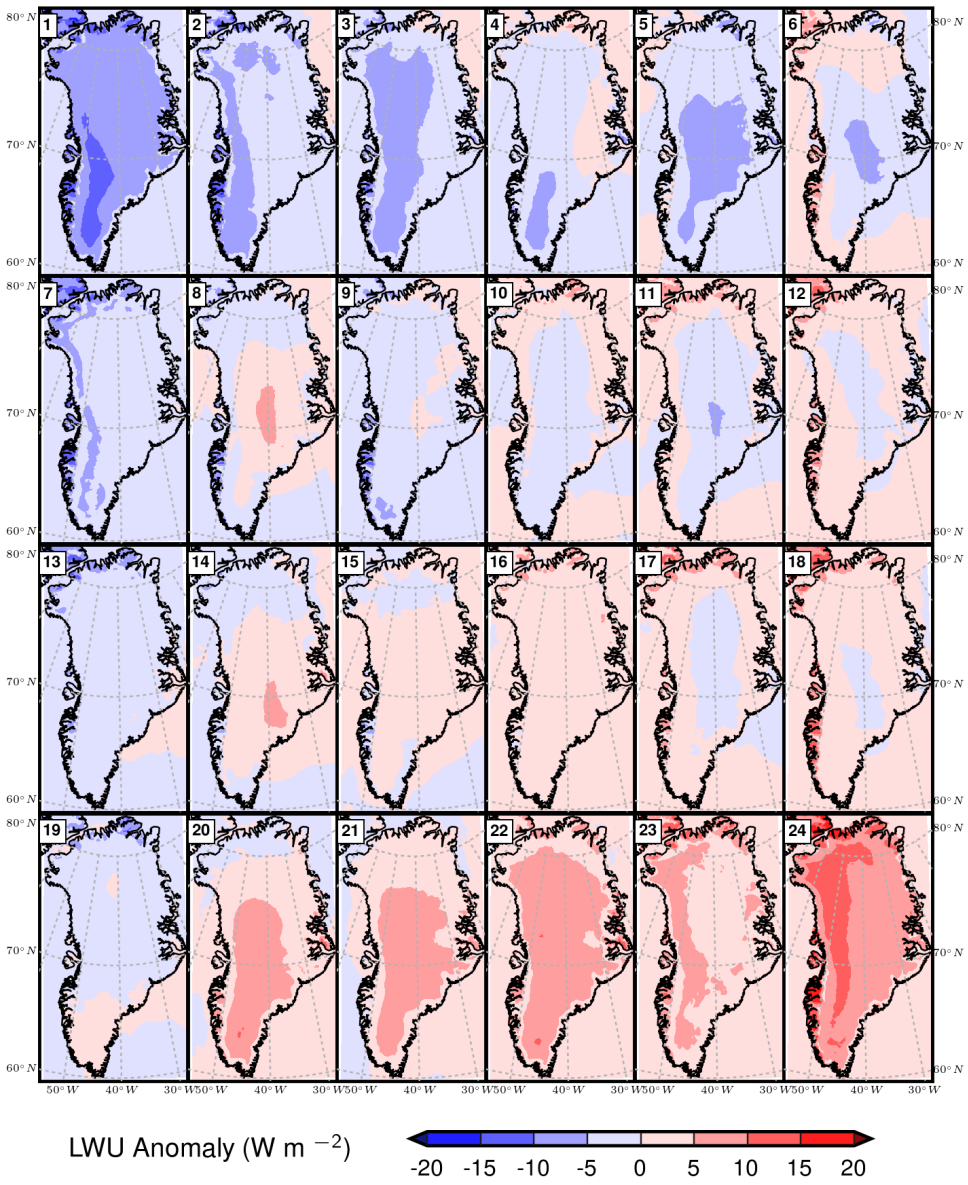

Figure 4.15. Composite upward longwave radiation (LWU) anomalies from MAR for dates mapped to each node.

the fact that troughs bring cold air from high latitudes equatorward, whereas ridges bring warmer air from lower latitudes poleward. Nodes in the interior of the map, characteristic of less amplified circulation show much weaker LWU anomalies, and are associated with weaker temperature anomalies. The strong negative LWU anomaly in node 1 and strong

positive LWU anomaly in node 24 may also play a role in the sign of the LWD anomaly in these nodes, with less (more) outgoing longwave radiation emitted by the surface, atmospheric temperatures are lower (higher), atmospheric emission is reduced(increased), and there is less (more) outgoing longwave radiation to be absorbed and radiated.

4.3.3 Net Radiation

To examine the net effect of both shortwave and longwave radiative fluxes, the net radiation at the surface is calculated as the sum of net shortwave and net longwave radiation. Results of this calculation for each node are shown in Figure 4.16. Across the clear majority of nodes, the anomalies over the GrIS sheet are very weak; only in the more extreme nodes (such as nodes 1–3, 22–24) are stronger anomalies seen, but only along coastal regions of southern Greenland. Nodes 1–3 see net losses of radiation along the southwestern coast, with net gains are seen in nodes 22–24. Of note is that the net radiation anomalies are stronger in magnitude over the adjacent ocean waters than over the GrIS; the vast difference in albedo between the ice sheet and seawater results in greater net shortwave radiation over water and thus a higher net radiation value.

4.3.4 Non-Radiative Fluxes

Non-radiative fluxes, specifically sensible and latent heat fluxes, were also analyzed. These fluxes transfer energy across a vertical gradient of temperature (sensible heat) or humidity (latent heat) via turbulent air motion [*Hartmann*, 1994]. These fluxes also play an important role in surface energy balance, and thus the potential for surface mass loss, and under certain conditions, may be even more important than radiative

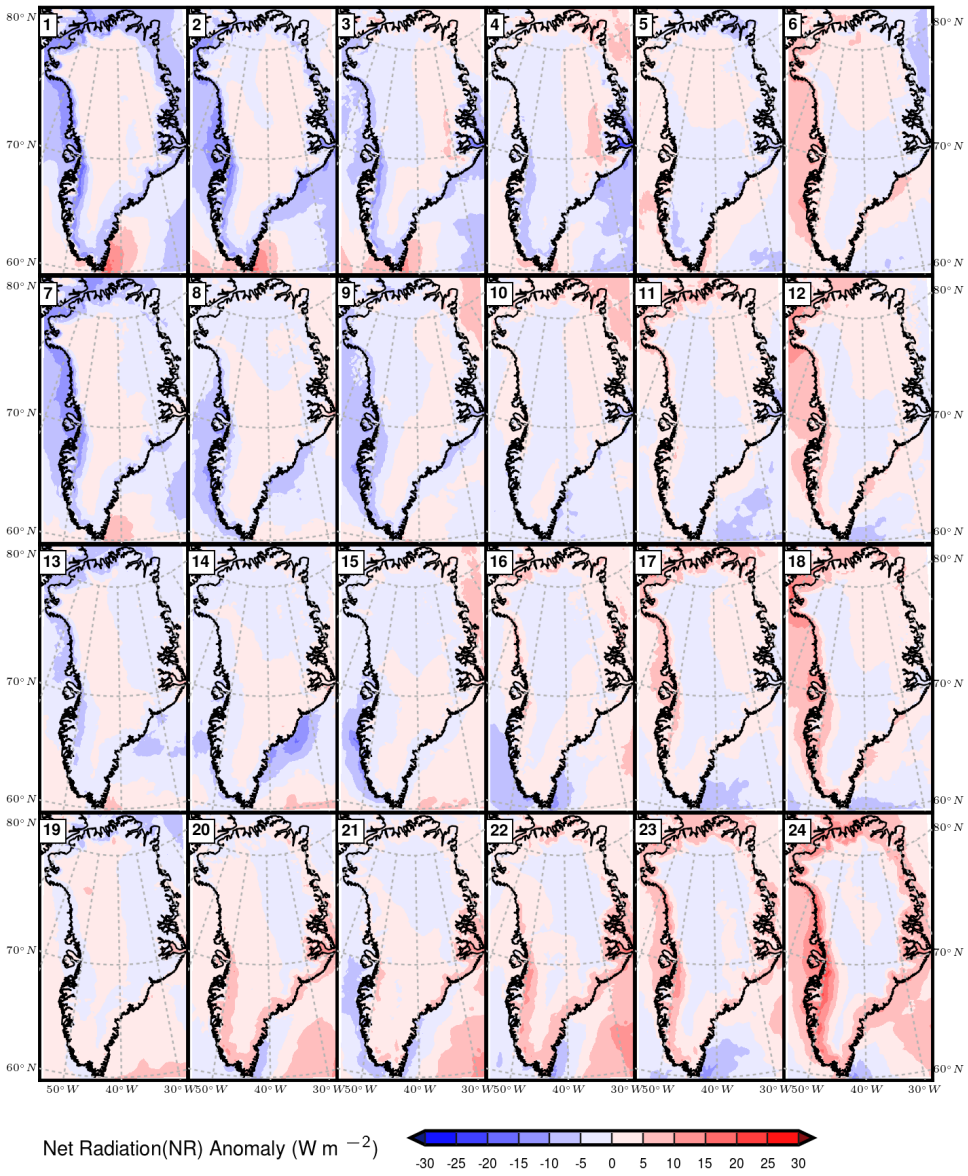

Figure 4.16. Composite net radiation (NR) anomalies, derived from SWD, AL, LWD, and LWU data from MAR, for dates mapped to each node.

fluxes, as demonstrated by *Fausto et al.* [2016]. The results for sensible heat flux can be seen in Figure 4.17. Like the net radiation anomalies, sensible heat flux anomalies are fairly weak over the interior of the ice sheet, with most of the stronger anomalies found in coastal regions. Nodes in the first row with negative net radiation anomalies along the southwestern coast have positive sensible heat flux anomalies, indicative of heat transfer

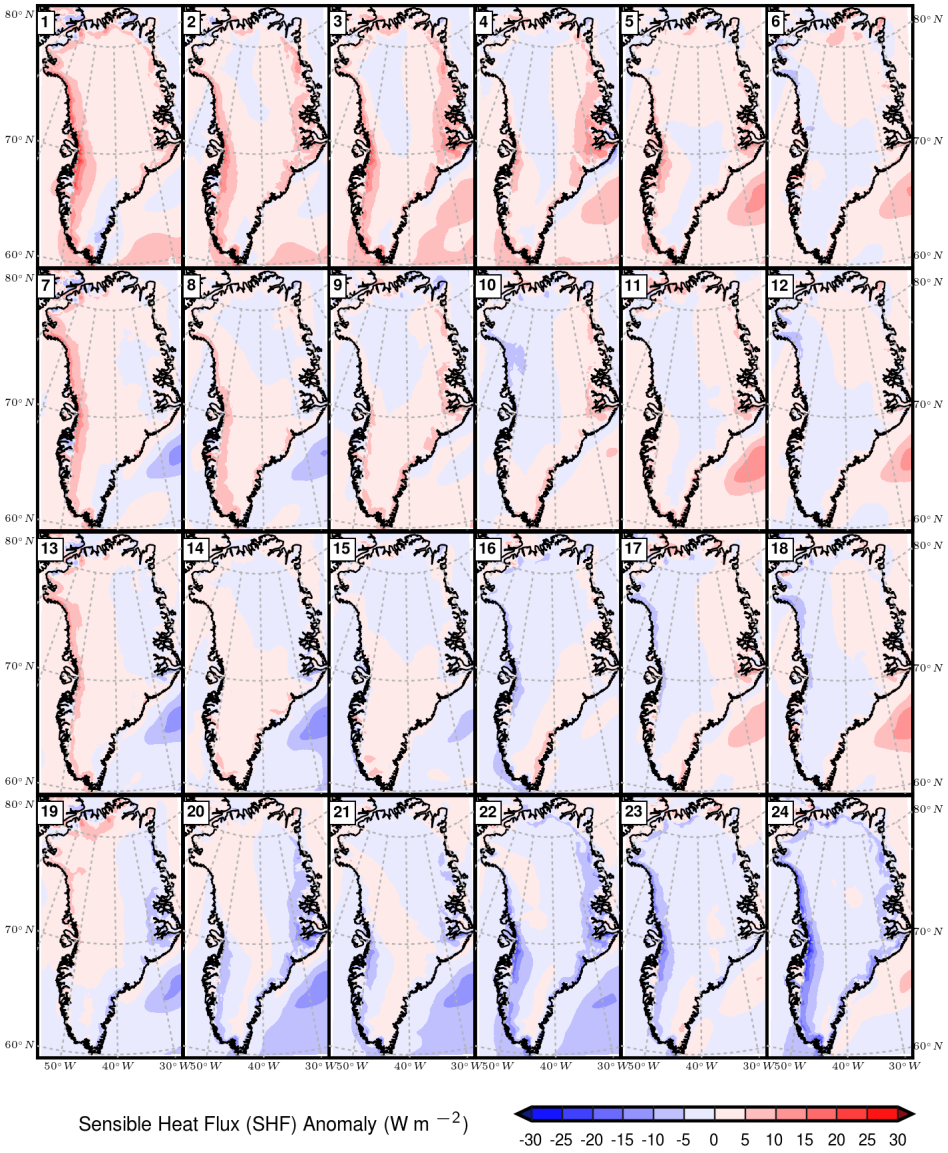

Figure 4.17. Composite sensible heat flux (SHF) anomalies from MAR for dates mapped to each node. Positive values indicate an upward flux.

from the surface upwards, likely due to a cold air advection over warmer ground. In contrast, nodes along the bottom row with positive net radiation anomalies in coastal regions see negative sensible heat anomalies, indicative of heat transfer into the surface from a warm air mass above. Also of note are the generally stronger sensible heat flux anomalies offshore of southeastern Greenland, near the Denmark Strait; these anomalies

are generally negative when ridging is present, but positive in the presence of troughing. This is likely due to the same processes seen over ice; the direction and magnitude of the flux is dependent on the temperature contrast present at the interface between the air and the surface.

Latent heat flux anomalies, seen in Figure 4.18, are generally extremely weak over Greenland, with magnitudes generally not exceeding ±5 W m^{-2}. The only exception is the coast of southeastern Greenland in node 1, where a much stronger positive LHF anomaly is present. This is likely due to sublimation occurring during a possible tip jet event, as discussed further in section 4.4.4. In general, nodes with strong negative 500 hPa geopotential height anomalies (e.g., nodes 1–5) show mainly positive latent heat flux anomalies over the ice sheet, as well as stronger anomalies over offshore waters. As these nodes are associated with troughing, the colder air moving into in the domain on these days is likely lower in specific humidity than the air it is replacing, resulting in upward (positive) flux of latent heat. Nodes with strong positive 500 hPa geopotential height anomalies (e.g., nodes 20–24) show the opposite pattern, with mainly negative latent heat flux anomalies over both land and water. These nodes are characterized by ridging, and poleward flux of warmer air (see Figure 4.5), likely resulting in warmer, higher specific humidity air passing over a drier boundary layer, and thus a negative latent heat flux. Larger latent heat fluxes are likely seen over water due to the much bigger difference in specific humidity between the surface of the ocean and the air above, as compared to the surface of the ice sheet and the air above. For both latent and sensible heat flux anomalies, the larger magnitude of the anomalies may also be due to the

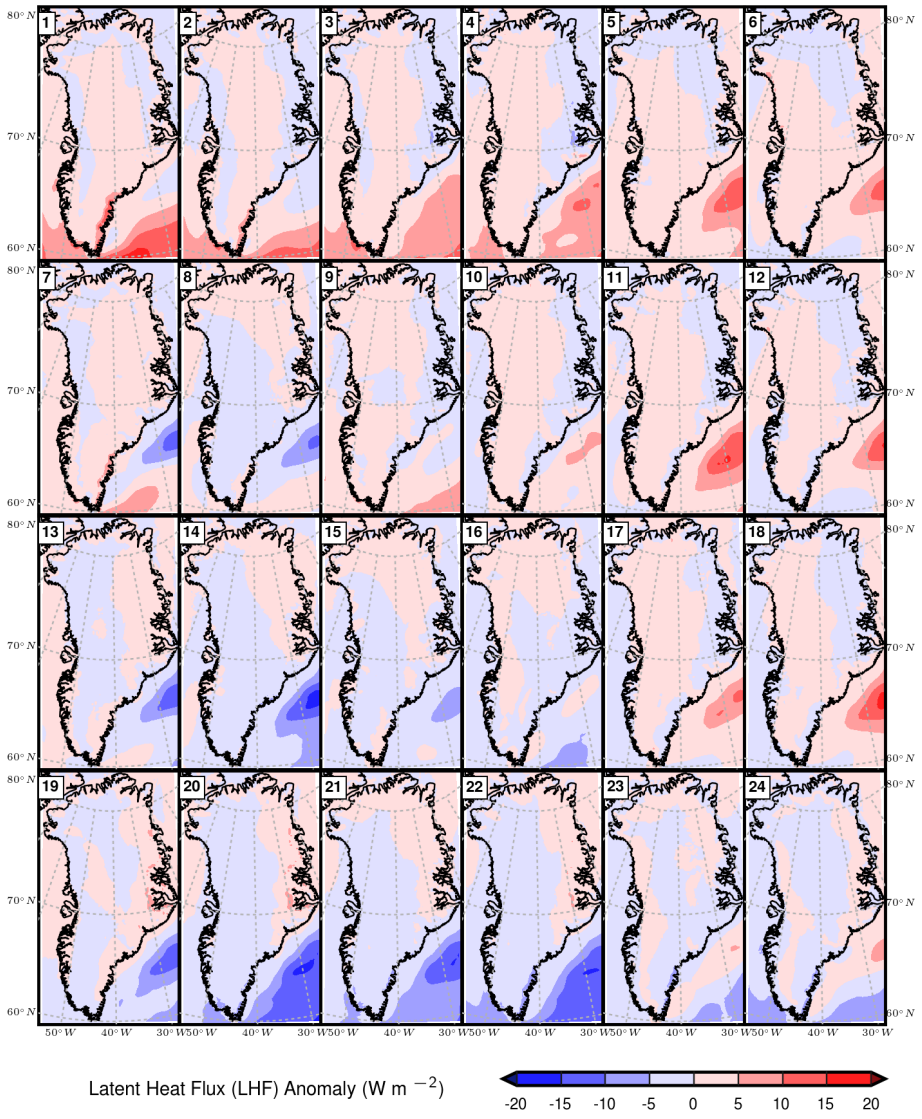

Figure 4.18. Composite latent heat flux (LHF) anomalies from MAR for dates mapped to each node. Positive values indicate an upward flux.

stronger net radiation anomalies present over water, resulting in a greater surplus of energy available for removal by turbulent fluxes (positive net radiation anomaly), or a greater deficit of energy for turbulent fluxes, allowing for energy to be added by turbulent fluxes (negative net radiation anomaly).

4.3.5 Summary

In summary, the surface energy balance analysis has shown the following:

- The sign of the cloud cover anomalies seen across the nodes are dependent on the sign of the 500 hPa geopotential height anomaly and associated vertical motion; positive (negative) 500 hPa geopotential height anomalies are associated with downward(upward) motion and negative(positive) cloud cover anomalies.
- SWD anomalies are dependent on cloud cover; positive (negative) cloud cover anomalies lead to negative (positive) SWD anomalies. Albedo anomalies are weak in most places, except in coastal Greenland, strong positive (negative) 500 hPa geopotential height anomalies result in strong negative (positive) albedo anomalies. The positive anomalies likely result from short-term processes (snowfall), while the negative anomalies are likely due to the short-term process of snow/ice melt, as well as a decreasing trend in ice sheet albedo and an increasing frequency of strong positive 500 hPa geopotential height anomalies. SWU anomalies are generally of the same sign as the corresponding SWD anomalies, although a weak SWD anomaly and a strong albedo anomaly may result in SWU and SWD having opposite signs.
- LWD anomalies are dependent on both cloud cover and air temperature. In general, positive (negative) cloud cover anomalies lead to positive (negative) LWD anomalies. However, this is not true in nodes with strong air temperature anomalies; in these cases, positive (negative) air temperature anomalies result in positive (negative) LWD anomalies. In contrast, LWU anomalies are generally spatially homogeneous and directly proportional to surface temperature. Net

radiation anomalies are generally weak, except in coastal areas of nodes 1–3 and 22–24.

- SHF anomalies are generally weak in the interior of Greenland and stronger along the coasts. Strong positive (negative) 500 hPa geopotential height anomalies are associated with negative (positive) sensible heat fluxes in these regions. LHF anomalies are generally very weak, except over water where the specific humidity gradient is larger.

4.4 Surface Mass Balance Analysis

In addition to conducting a surface energy balance analysis, a surface mass balance analysis was also conducted. Anomalies of meltwater production, runoff, and refreezing are examined first, followed by snowfall, rainfall, and sublimation. Meltwater production is the volume of meltwater (mmWE) produced on a given day (the temporal resolution of the MAR data) for a given model gridpoint. Importantly, meltwater production is not equivalent to runoff, as meltwater may refreeze in glacial firn or snow [*Machguth et al.*, 2016]. Instead, runoff is highly dependent on factors such as local topography, elevation and firn saturation [*Rennermalm et al.*, 2013]. Meltwater produced in the lower elevation ablation zone is more likely to run off compared to meltwater produced in the higher elevation percolation zone, which is more likely to be retained and/or refrozen in the snowpack or in glacial firn [*Rennermalm et al.*, 2013]. While meltwater retention and refreezing serves as a buffer against GrIS surface mass loss [*Box*, 2013; *Rennermalm et al.*, 2013; *van den Broeke et al.*, 2016], the refreezing process is

also important to the surface energy balance due to the release of latent heat into the snowpack during phase change [*van den Broeke et al.*, 2016].

4.4.1 Meltwater Production (ME) Anomalies

Meltwater production anomalies for each node of the master SOM can be seen in Figure 4.19. Nodes with anomalously low meltwater production, such as nodes 1–5 and 7–9, are also those dominated by negative 500 hPa geopotential height anomalies over much of Greenland. This corresponds well with the surface energy balance analysis, which shows positive albedo anomalies (suggestive of freshly fallen snow), negative LWU anomalies (indicating a colder surface), negative net radiation anomalies coincident with the strongest meltwater production anomalies, along with positive SHF anomalies and weakly positive LHF anomalies, likely indicating the transfer of heat away from the surface.

In contrast, nodes with anomalously high meltwater production, such as nodes 20–24 are dominated by positive 500 hPa geopotential height anomalies over much of Greenland. Like the nodes with anomalously low meltwater production, nodes with anomalously high meltwater production also correspond well with the surface energy balance analysis. Areas of anomalously high meltwater production are co-incident with negative albedo anomalies, positive LWU anomalies (indicating a warmer surface), positive LWD anomalies, and positive NR anomalies, all resulting in more energy available at the surface for melt. The negative SHF anomalies co-incident with the positive meltwater production anomalies suggest transfer of heat toward the ground

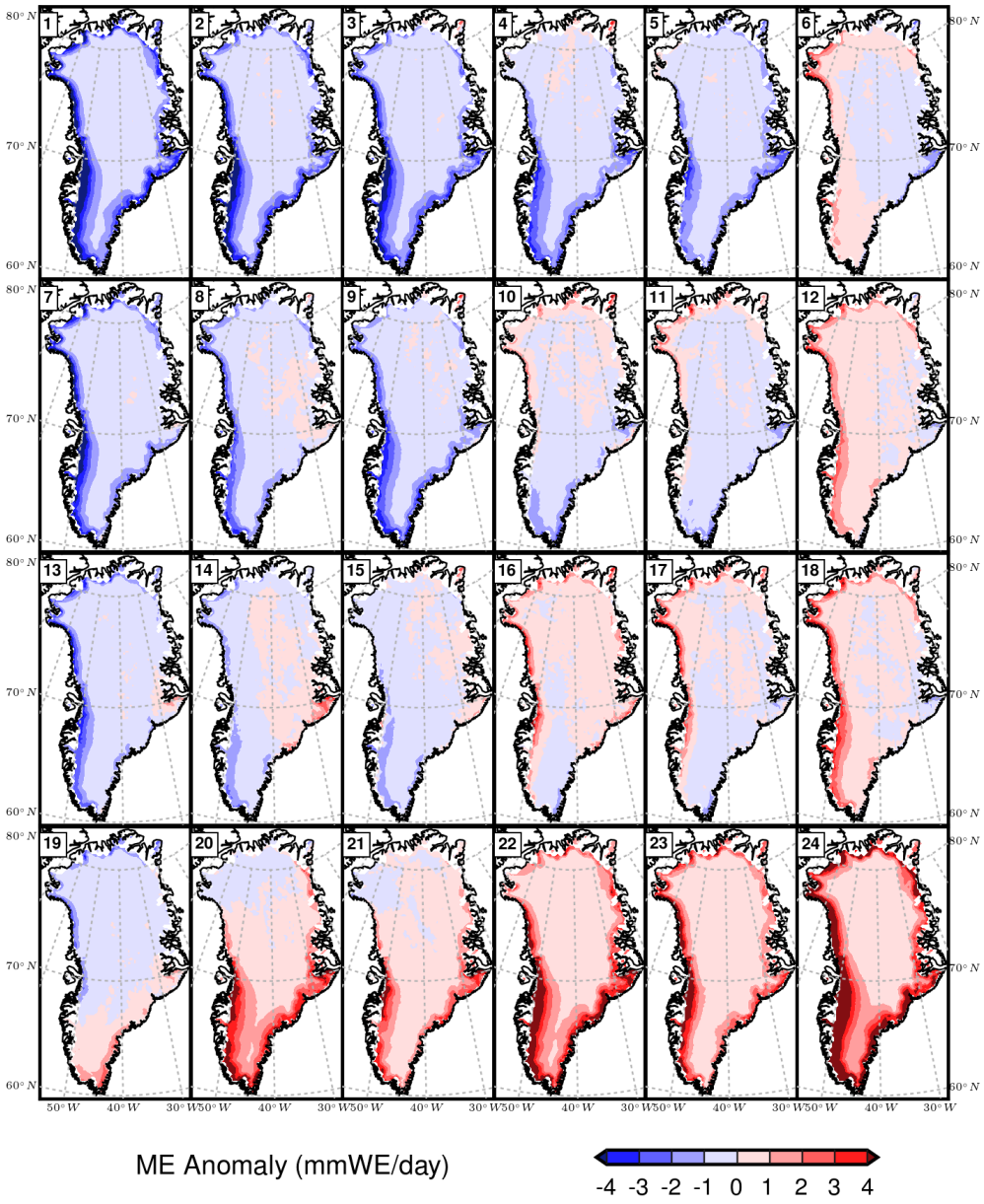

Figure 4.19. Composite meltwater production (ME) anomalies from MAR for dates mapped to each node.

Comparing the results of this analysis with those of *Mioduszewski et al.* [2016], very similar results are seen across multiple variables. In both analyses, high melt nodes are characterized by positive SWD anomalies and negative cloud cover anomalies over most of the ice sheet; the signs of these anomalies are reversed for low melt nodes.

Interestingly, both analyses show that extreme southern Greenland experiences conditions that are often very different from the rest of the island during certain low melt nodes. Node 1 days in extreme southern Greenland are characterized by negative cloud cover anomalies, positive SWD anomalies, positive SWU anomalies, strongly negative LWD anomalies, and strong positive latent heat flux anomalies along the southeastern coast. In contrast, most of Greenland experiences positive cloud cover anomalies, negative SWD anomalies, negative SWU anomalies (except in coastal areas where snow has likely fallen), weakly negative LWD anomalies, and weakly positive latent heat flux anomalies. Similar contrast can be seen in the comparison by *Mioduszewski et al.* [2016] of anomalies between high and low melt nodes (their Figure 6). Given the strong westerly winds extending off the southern tip of Greenland at both the 500 hPa level (Figure 4.6) and the $\sigma = 0.995$ level (Figure 4.7), this may be indicative of a possible westerly tip jet event. These "short-lived, shallow and narrow high speed wind events" [*Serreze and Barry*, 2014] can result in acceleration of air down the lee side of a mountain barrier [*Serreze and Barry*, 2014]; perhaps it is this descending air that results in the clearer conditions seen in extreme southern Greenland in Node 1 as compared to the rest of Greenland. Given that most prior research on Greenland tip jets focuses on the winter season, further exploration of these summer events is needed.

4.4.2 Runoff (RU) Anomalies

Turning from meltwater production to runoff, the spatial pattern of runoff anomalies is like that of the meltwater production anomalies; stronger magnitude anomalies are found near coasts with weaker anomalies inland. It is very important to

note that the magnitude of the runoff anomalies is less than those of the corresponding meltwater production anomaly, signifying that not all meltwater runs off. Selected nodes with strong runoff anomalies are shown in Figure 4.20. While strong meltwater production anomalies (both positive and negative) are found in both the ablation zone and the percolation zone, the runoff anomalies are found only in the ablation zone, as cooler conditions in the higher elevation percolation zone likely result in meltwater refreezing in-situ. Where both strong meltwater production anomalies and runoff anomalies are found, they agree in sign; anomalously low meltwater production leads to anomalously low runoff (such as nodes 1 and 2), and vice versa (nodes 22–24).

4.4.3 Refreezing (RZ) Anomalies

As previously described in section 4.4.2, a portion of the meltwater produced on the GrIS does not run off, but instead refreezes, providing a buffer against surface mass loss [*Box*, 2013; *Rennermalm et al.*, 2013; *van den Broeke et al.*, 2016]. Meltwater refreezing anomalies associated with selected nodes are shown in Figure 4.21. Low melt nodes 1–3 show a positive refreezing anomaly close to the southwestern coast of Greenland, with a negative refreezing anomaly further inland. As these nodes are characterized by anomalously cold conditions (see LWU anomalies, Figure 4.15), with negative meltwater production anomalies (Figure 4.19) the meltwater that is produced under these conditions likely refreezes in-situ, whereas warmer conditions would likely lead to greater meltwater production and runoff, hence the observed positive refreezing anomaly. While negative meltwater production anomalies are also seen further inland in nodes 1–3, the refreezing anomalies here are of opposite sign to those on the coast.

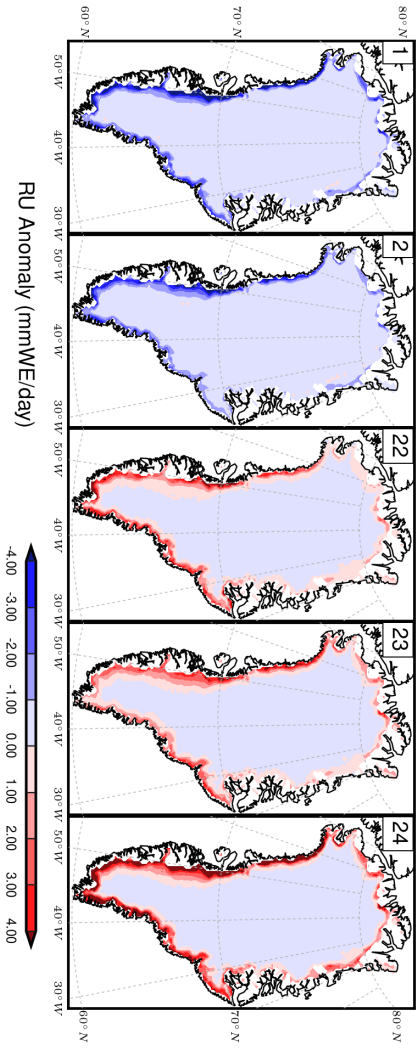

Figure 4.20. Composite runoff (RU) anomalies from MAR for dates mapping to selected nodes.

At these higher elevations, a significant fraction of meltwater produced may be retained and refrozen, and with less meltwater produced in nodes 1–3, thus reducing the amount of meltwater available to refreeze, resulting in the observed negative refreezing anomaly. The high melt nodes 22–24 show the opposite pattern, especially node 24. These nodes are characterized by anomalously warm conditions (see LWU anomalies, Figure 4.15) with positive meltwater production anomalies (Figure 4.19). Refreezing anomalies

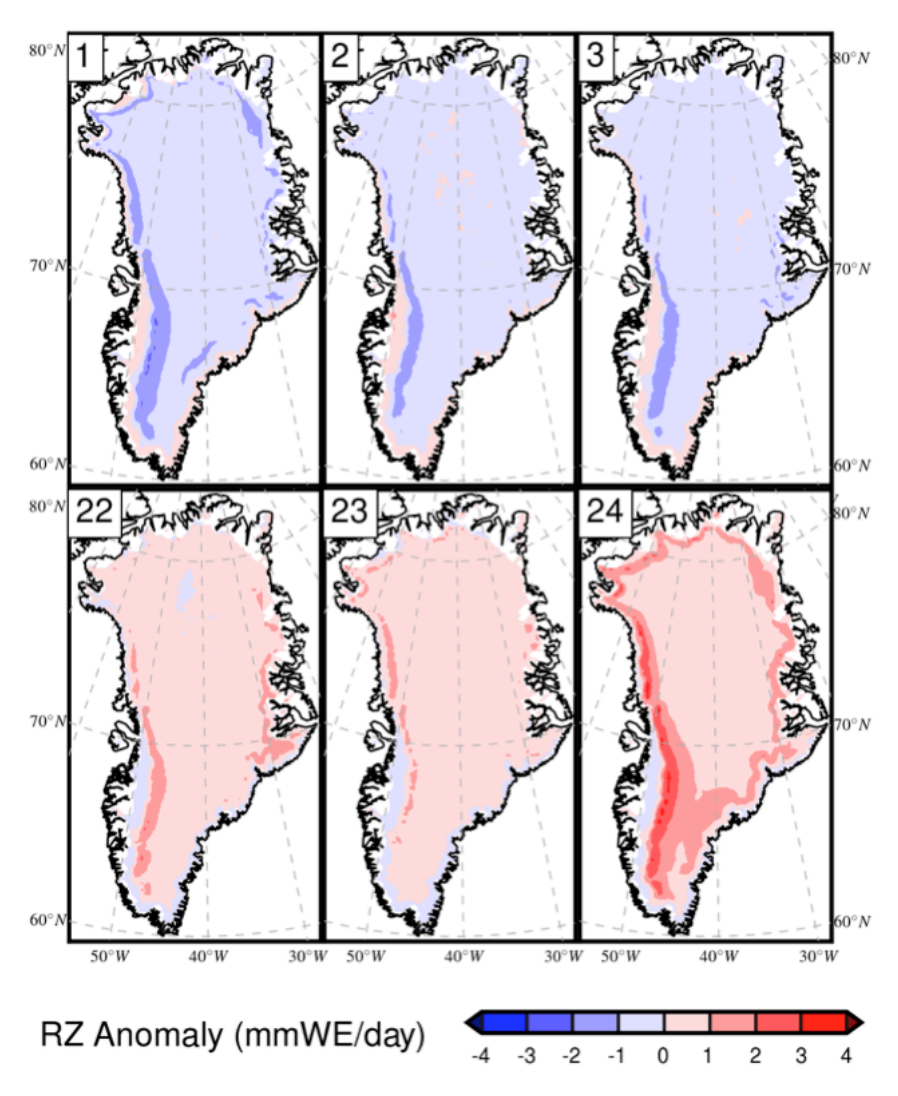

Figure 4.21. Composite refreezing (RZ) anomalies from MAR for dates mapping to selected nodes.

near the southwestern coast are negative; while runoff anomalies are also positive, indicating that the warm conditions in these nodes favor reduced retention and refreezing, hence the negative refreezing anomalies observed at lower elevation areas near the coast. Further inland, the magnitude of the positive runoff anomalies is much smaller. The reduced runoff here compared to locations near the coast suggests increased meltwater

retention. With a larger volume of meltwater being produced and retained, refreezing anomalies are positive.

4.4.4 Sublimation (SU) Anomalies

While the main mechanism for GrIS surface mass loss is runoff, sublimation (SU) also contributes to mass loss, albeit on a much smaller scale; the values of the sublimation anomalies are an order of magnitude lower than the runoff anomalies. Every node displays very weak anomalies (± 0.2 mm/WE day) across the entire ice sheet, except for Node 1 (depicted in Figure 4.22), which shows a stronger positive anomaly along the southeastern coast. As previously described in section 4.3.1, this area of Greenland is characterized by negative cloud cover anomalies and positive SWD anomalies during node 1 and node 2 days. It also displays some of the strongest positive LHF anomalies (see Figure 4.18), which suggest drier air above the surface. In addition, node 1 is characterized by strong westerly winds (see Figure 4.7); together, this suggests a relatively cloud-free, windy and dry environment conducive to snowpack sublimation.

4.4.5 Snowfall (SF) and Rainfall (RF) Anomalies

While examining the synoptic climatology of processes that remove mass from the GrIS (runoff, sublimation) is important, it is equally important to understand the additive term in the GrIS SMB, precipitation. GrIS SF anomalies associated with each node are presented in Figure 4.23. The anomalies are generally weak in magnitude, although there are several nodes with strong positive anomalies. These positive anomalies are generally found along the southeastern coast, a region which receives more annual

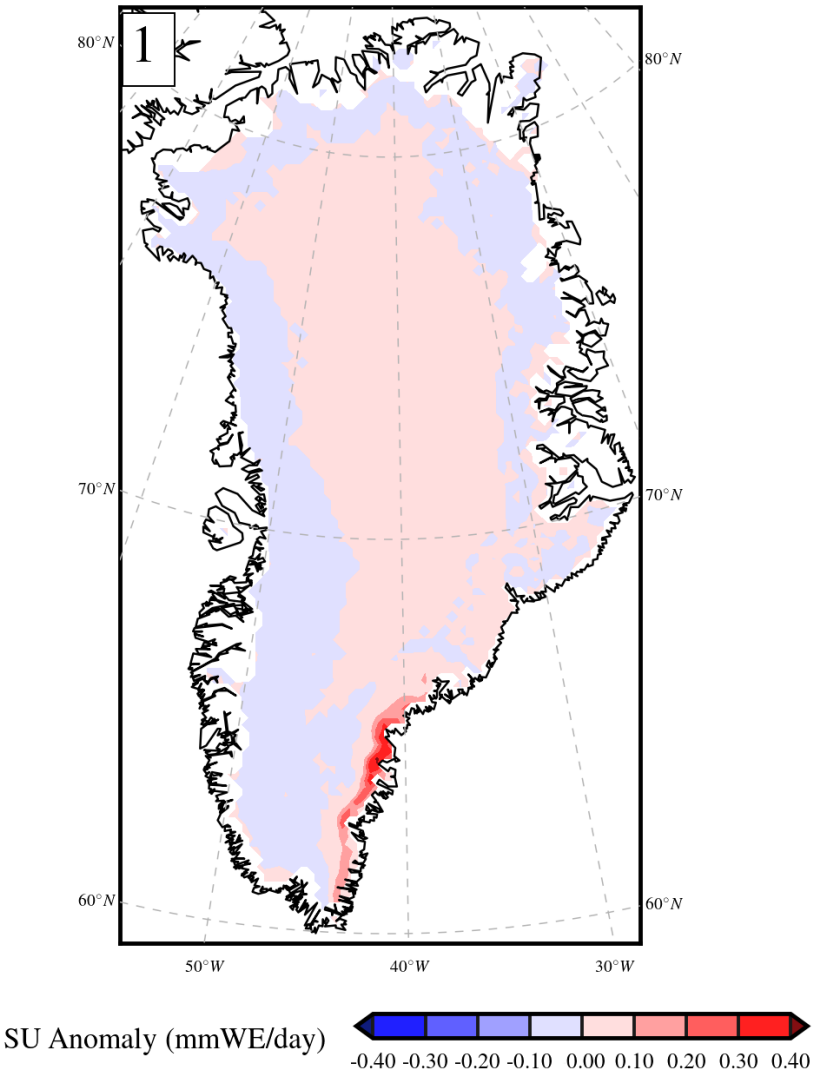

Figure 4.22. Composite sublimation (SU) anomalies from MAR for dates mapping to node 1.

precipitation than any other part of Greenland [*Serreze and Barry*, 2014]. Nodes 3 and 4 show a strong positive anomaly along the central portion of Greenland's east coast; this snowfall coincides with an area of negative SWD anomalies, but positive cloud cover, LWD and albedo anomalies. Nodes 8 and 14 also display positive snowfall anomalies along the southeastern coast. As mentioned in section 4.3.2, these nodes exhibit much stronger positive LWD anomalies than nodes 7 and 13 respectively, which

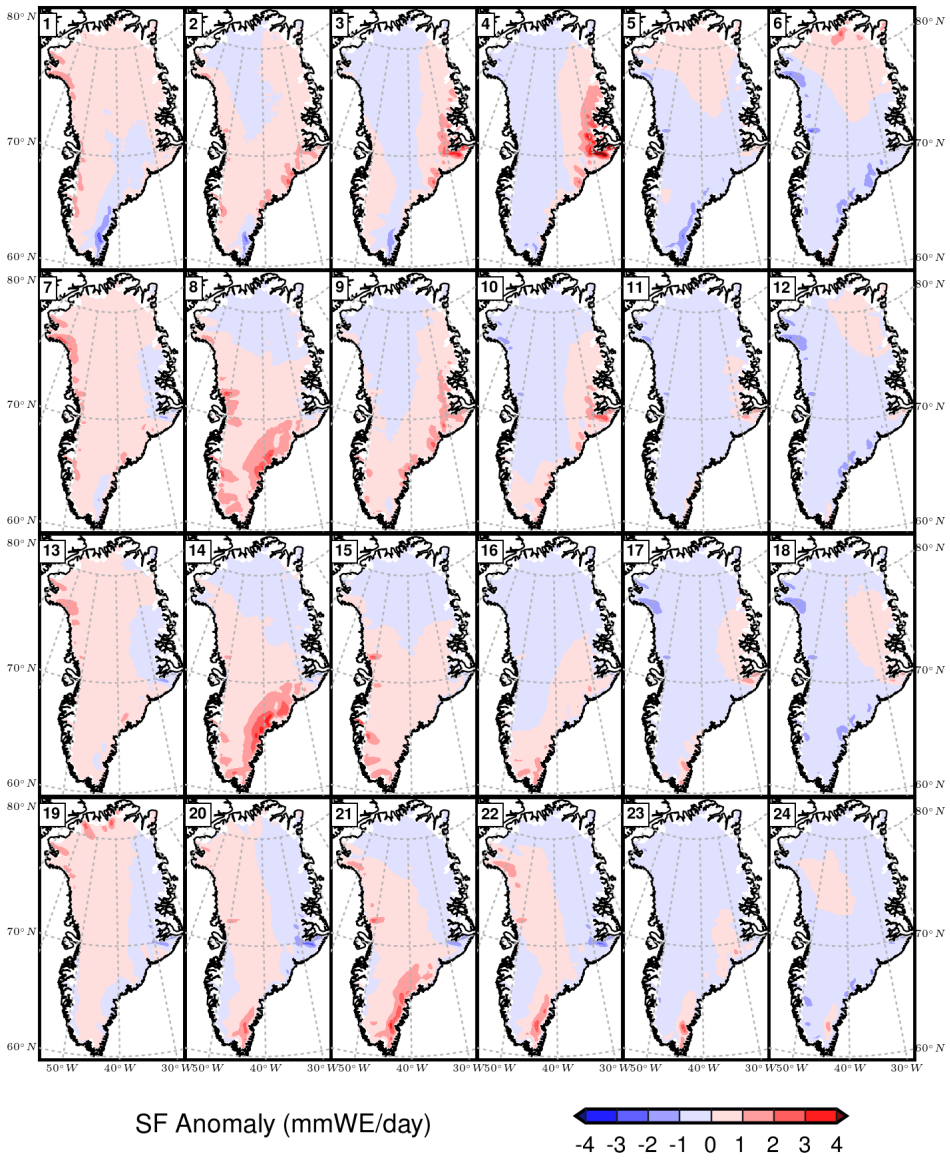

Figure 4.23. Composite snowfall (SF) anomalies from MAR for dates mapped to each node.

appear similar in the master SOM. This is likely due to warmer temperatures and stronger positive cloud cover anomalies associated with a circulation pattern that allow for better onshore moisture transport (see Figures 4.7 and 4.8). Node 6 in far northern Greenland also shows positive snowfall anomalies, which like nodes 8 and 14, is likely due to onshore moisture transport. The low melt nodes (1–3) display negative SF anomalies

along the southeastern coast, compared to the positive anomalies found over much of the GrIS. A similar pattern is seen in the high melt nodes 20–24, albeit with the signs reversed. The enhanced snowfall in these nodes may be due to onshore flow associated with the circulation of the surface high found east of Greenland (see Figure 4.3), as the high moves to a less favorable position for onshore flow (from node 20 towards node 24), the magnitude of the snowfall anomaly diminishes.

While rainfall is rare over most of Greenland, it is serves as a source of energy for snowmelt and thus can have a significant impact on the thermal state of the snowpack [e.g., *Levia and Leathers*, 2011]. Rainfall (RF) anomalies for each of the nodes are seen in Figure 4.24. These anomalies are an order of magnitude lower than the snowfall anomalies, with the strongest anomalies found in the warmer coastal regions; inland regions that rarely receive rain exhibit much weaker anomalies. The low melt nodes (1–3) display negative anomalies for rainfall, like the result for snowfall, and likely for the same reason (negative cloud cover anomalies, sinking air motion). In addition, the strong negative 3-m air temperature anomalies found in these nodes reduce the likelihood that precipitation will fall as rain. High melt nodes along the bottom row of Figure 4.24 (nodes 20–24), which exhibit the strongest positive 3-m air temperature anomalies of all nodes, unsurprisingly show the greatest positive rainfall anomalies. The strongest positive anomalies are located along the southeastern coast, making it highly probable that they are due to the same type of onshore flow seen with the snowfall anomalies. Comparing node 8 to node 7, node 8 displays strong positive anomalies while node 7 displays weak negative anomalies. This is likely due to the same favorable onshore moisture transport mechanism that results in larger positive snowfall anomalies in node 8 versus node 7, as

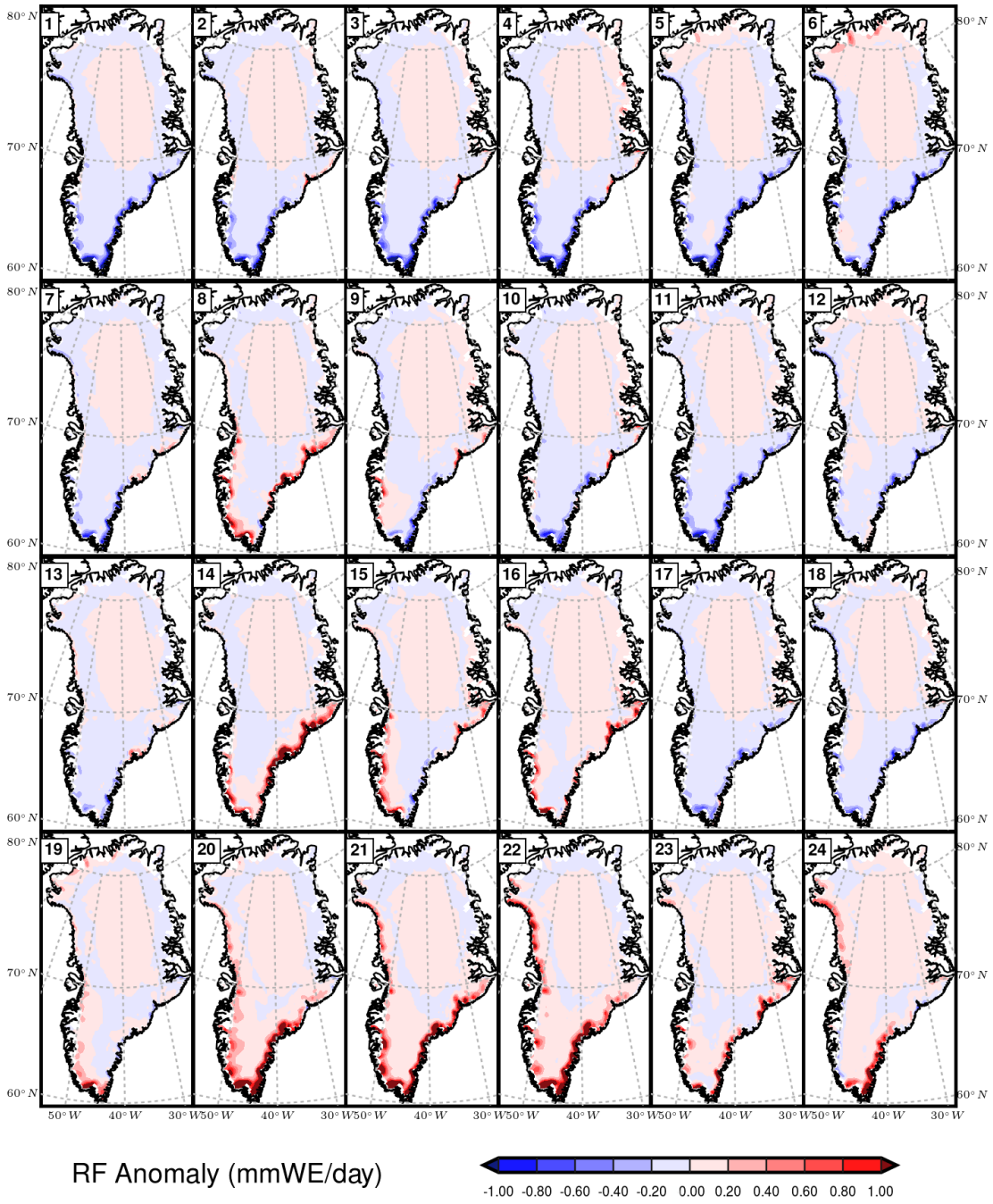

Figure 4.24. Composite rainfall (RF) anomalies from MAR for dates mapped to each node.

well as warmer conditions in node 8 that make rainfall more likely. The differences in rainfall anomalies between nodes 14 and 13 are also explained by this same mechanism.

4.4.6 Surface Mass Balance (SMB) Anomalies

While examining the spatial distribution of anomalies for each surface mass balance component is instructive, it is also important to take a broader view and examine the combined effect of both additive (precipitation) and subtractive (runoff and sublimation) processes on surface mass balance anomalies (SMB) and their spatial distribution. These SMB anomalies are shown in Figure 4.25. The effects of precipitation on mass balance can easily be seen, with positive SMB anomalies for nodes 3, 4, 8, 14 and 20–24 in the same region where positive precipitation anomalies are found. The loss of mass due to sublimation in far southern Greenland is also clear in node 1. As each node's SMB anomaly pattern represents the composite pattern of surface mass change for that particular node over the course of one day, it appears that the greatest change in GrIS SMB over the course of a single day usually comes from precipitation events, as evidenced by the strong positive anomalies found in areas receiving precipitation. Even in the more extreme nodes on the map (found on the top and bottom rows), the SMB anomalies are not uniformly positive in "cold" nodes or negative in "warm" nodes, but instead display a more heterogeneous pattern, with different portions of the GrIS gaining or losing mass depending on which processes are occurring. A particular atmospheric circulation pattern may have very different effects on SMB in different regions of the GrIS. For example, the circulation pattern associated with node 1 result in small positive SMB anomalies over much of the ice sheet, especially in the northwest. In contrast, the southeastern coast sees mass losses associated with sublimation, as described in section 4.4.4. On the other hand, the circulation patterns associated with nodes 3, 4, 8, and 14 demonstrate that substantial gains in mass are also highly regionalized. Thus, the number

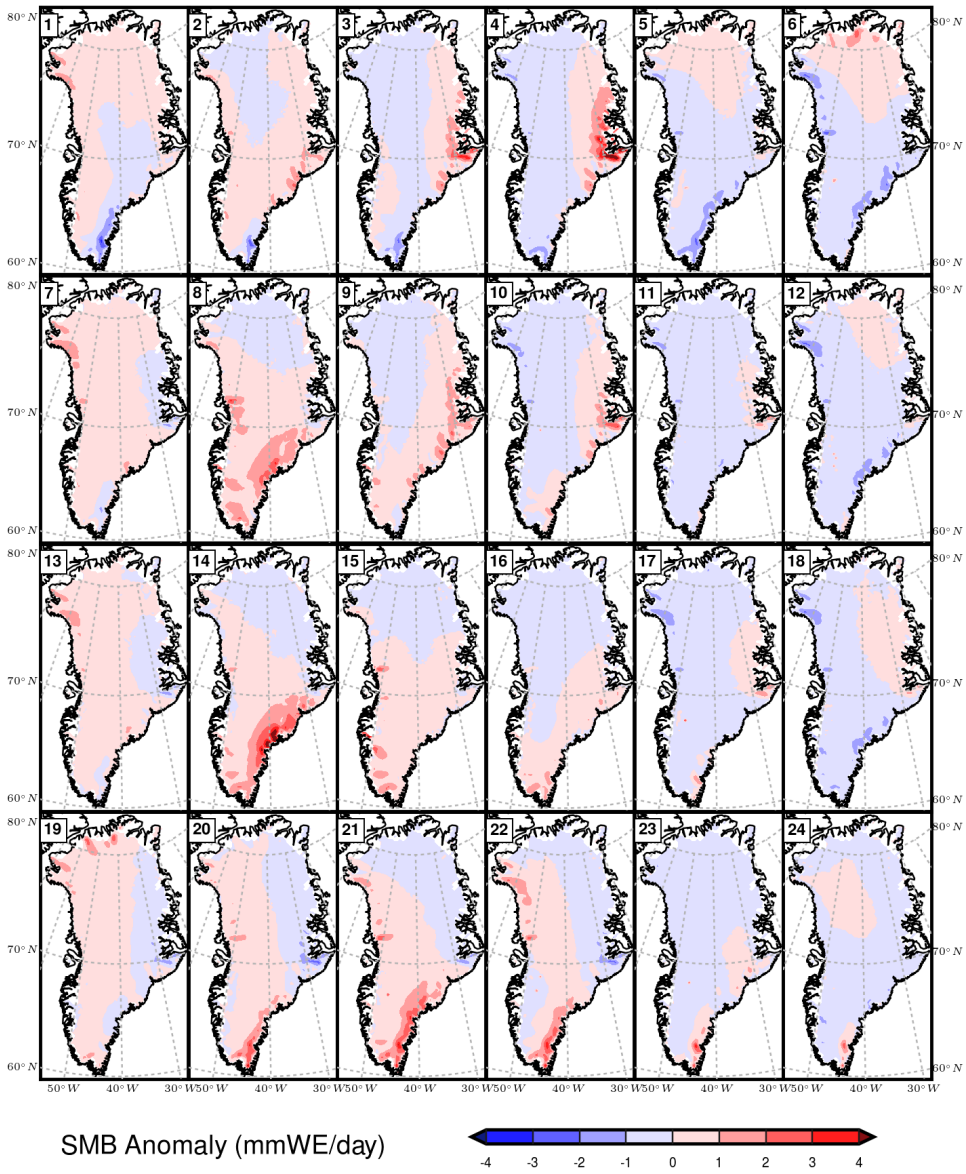

Figure 4.25. Composite surface mass balance (SMB) anomalies from MAR for dates mapped to each node.

and frequency of nodes that occur during a particular summer, as well as how long each particular pattern persists, determine the surface mass change in each region of the ice sheet, as well as the ice sheet as a whole.

4.4.7 Summary

In summary, the surface mass balance analysis has shown the following:

- Nodes dominated by positive (negative) 500 hPa geopotential height anomalies are characterized by strong positive (negative) meltwater production anomalies; these anomalies correspond well with both the radiative and non-radiative fluxes examined in the surface energy balance analysis.
- Runoff anomalies are of the same sign but of much lower magnitude than the meltwater production anomalies, and are generally confined to the lower elevation ablation zone.
- Refreezing anomalies in low (high) melt nodes are positive (negative) near the edges of the ice sheet, but negative (positive) in the higher elevations further inland.
- Sublimation anomalies are an order of magnitude lower than the runoff anomalies; only one node (node 1) displayed strong (positive) anomalies due to negative cloud cover anomalies, positive SWD anomalies, positive LHF anomalies, and strong near-surface winds.
- Snowfall anomalies are generally weak over most of the ice sheet, except for strong positive anomalies along the eastern coast where moisture is being advected onshore by an offshore cyclone.
- Rainfall anomalies are an order of magnitude lower than the snowfall anomalies; strong rainfall anomalies are confined to warmer regions near coasts. The same physical mechanisms (moisture transport and vertical

motion) that govern snowfall anomalies also apply for rainfall, although positive (negative) air temperature anomalies in high (low) melt nodes may also contribute to the positive (negative) rainfall anomalies

- Surface mass balance anomalies are generally weak in magnitude, indicating that a given circulation pattern usually does not result in large surface mass changes (SMB) on daily time scale. However, several nodes exhibit large positive SMB anomalies due to snowfall. SMB anomalies are spatially heterogeneous; a given circulation pattern may see mass losses in one region and mass gains in another.

4.5 Node Persistence, Transition, and Frequency Change Analysis

Additional insight into the temporal evolution of atmospheric circulation comes from determining whether the circulation tends to persist in a particular node for multiple days, or if the node tends to be a transitional state. Given that each node of the master SOM produces a different pattern of mass loss or gain in different regions of the ice sheet, the persistence of a certain node over time may have major effects on SMB both regionally and across the entire ice sheet. While transience and persistence are useful metrics, knowing *which* node the circulation will transition to after residing in a particular node also allows for additional insight on the temporal evolution of the 500 hPa circulation. For a given node, the most frequent "destination" nodes were determined, resulting in a list of characteristic transition patterns and their frequency. Lastly, it is important to not only examine how the atmospheric circulation evolves over the short-term (a period of several days, or the average lifespan of a synoptic-scale weather

system), but also over periods of years to decades. Changes in the frequency of occurrence for each node over the 115-year climatology were examined, as well as the statistical significance of these changes.

4.5.1 Node Persistence and Transition Analysis

Results of the node persistence analysis are shown in Table 4.1. For all occurrences of a particular node, the following percentages were determined: percentage of time that the circulation resided in the same node the next day ("persistent"), percentage of time that the circulation moved to a neighboring node ("neighbor") and the percentage of time that the circulation moved to a non-neighboring node ("non-neighbor"). For most of the nodes in the map, the circulation is transient; the circulation tends to move to another node, neighbor or non-neighbor, more than 50% of the time. However, there is great variation among the nodes in this behavior. Some nodes around the edges of the map, such as 3, 5, 6, and 22 are nearly equally divided between the percentage of time that the circulation persists in the node and the percentage of time that the circulation moves to another node, either neighboring or non-neighboring. The percentage of time that the circulation moves to another node is only slightly greater, with node 6 being almost evenly divided (49.82% persistence, 50.18% moving to another node). In contrast, nodes in the interior of the map tend to be transient. For example, when the 500 hPa height pattern resembles that of nodes 8, 9, 11, 14, or 15, the percentage of time that it resides in these nodes for a second consecutive day is below 30% in all cases. Node 14 has the lowest persistence of all nodes, at only 15.86%. These results are like those of *Schuenemann et al.* [2009], who also found nodes around the

Table 4.1. Results of the node persistence analysis. Nodes in bold are classified as persistent, while all others are classified as transient.

Node	Persistent	Neighbor	Non-Neighbor
1	**67.04%**	**16.70%**	**16.26%**
2	25.64%	65.20%	9.16%
3	47.42%	32.47%	20.10%
4	31.12%	55.29%	13.60%
5	42.86%	23.00%	34.15%
6	49.82%	33.16%	17.02%
7	33.73%	55.02%	11.24%
8	27.76%	58.68%	13.56%
9	27.18%	62.78%	10.03%
10	33.78%	57.03%	9.19%
11	22.07%	69.01%	8.92%
12	34.22%	55.12%	10.66%
13	32.66%	50.23%	17.12%
14	15.86%	74.45%	9.69%
15	28.22%	60.43%	11.35%
16	32.17%	60.29%	7.54%
17	27.06%	63.04%	9.90%
18	37.68%	53.45%	8.87%
19	**51.26%**	**26.80%**	**21.94%**
20	38.95%	34.28%	26.77%
21	30.65%	57.44%	11.90%
22	43.33%	23.52%	33.15%
23	29.33%	59.01%	11.66%
24	**72.61%**	**15.92%**	**11.47%**

edges of the map to be more persistent. Comparing the frequencies of neighbor to non-neighbor transitions, all nodes, except for nodes 5 and 22, shows a higher frequency of neighbor transitions than non-neighbor transitions. That is, for the clear majority of nodes on the map, if the circulation moves out of that particular node after one day, it is more likely to move into a neighboring node than a non-neighboring node. Nodes in the interior of the map show the lowest rate of non-neighbor transitions, at least in part because they have a greater number of neighbors than nodes along the map edges, which have fewer neighbors. The greater frequency of neighbor-to-neighbor transitions is

intuitive in that the circulation pattern does not often change so drastically over one day that the new best matching unit is not bordering the previous day's best matching unit.

The most persistent nodes are found in the corners of the map. In these nodes (1, 19 and 24) the circulation pattern is more likely to stay in the same node the next day than to move to another node. Node 6, while a corner node, is slightly more transient than persistent, but by only a small margin, as mentioned previously. Node 24, on the other hand is the most persistent node of all, with the circulation pattern tending to stay in this node for a second consecutive day 72.61% of the time. This may explain why the corner nodes (1, 6, 19, 24) are also among the most frequently occurring (ranked 1st, 2nd, 3rd, and 6th in frequency, respectively).

The results of this node transition analysis are shown in Figure 4.26. Starting in one of the edge nodes, it is possible to trace a path through the map to examine a possible scenario for how the circulation may evolve over time. For example, beginning in node 24, if the circulation changes between days and moves to another node, it is most likely to move into node 18, with weakening of the large positive 500 hPa geopotential height anomaly over Greenland. From node 18, the most likely path is upwards towards node 12, followed by node 6 and then node 5, with the result being positive 500 hPa geopotential height anomalies giving way to a large area of negative 500 hPa geopotential height anomalies centered between Iceland and Scotland. In the top row, the circulation will most likely move right (negative 500 hPa geopotential height anomalies moving from Greenland towards Europe) or left (strong negative 500 hPa geopotential heights centered over Greenland) rather into the interior nodes. In the leftmost column, the circulation is likely to move down the column (negative 500 hPa geopotential height

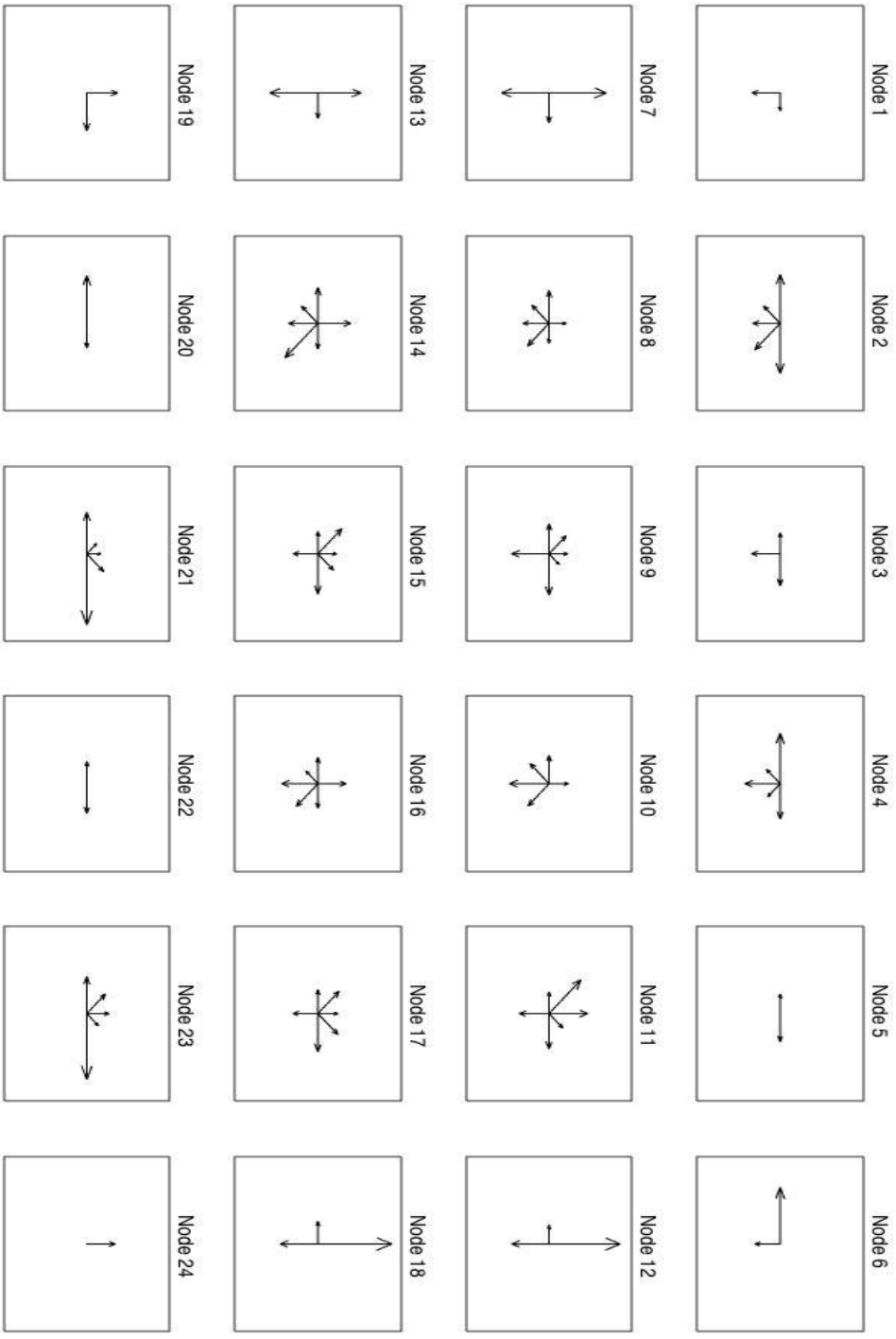

Figure 4.26. Results of the node transition analysis. Size of the vector is proportional to the percentage of days that transition from the node of origin to the node indicated. For clarity, only neighbor to neighbor transitions with a frequency of 5% or greater are shown.

anomalies lift north into Arctic Ocean) or up the column (negative 500 hPa geopotential height anomalies move south towards Greenland). Along the bottom row, the circulation will most likely move right towards node 24 (strong 500 hPa geopotential height anomalies build over Greenland) or move left towards node 19 (strong 500 hPa geopotential height anomalies move east from Greenland towards Europe).

Thus, for most of the nodes around the outer edge of the map, a transition to another "edge" node is most likely, while a trajectory towards the interior is less common. In contrast, the interior nodes display a great variety of possible trajectories, either to another interior node or to one of the outer edges. However, this may simply be due to the map topology, as the interior nodes have a greater number of neighbors, and hence a greater number of possible trajectories.

4.5.2 Node Frequency Analysis

Results of the node frequency analysis are shown in Figure 4.27. Nodes 1 and 24, which have, respectively, the strongest positive and negative 500 hPa geopotential height anomalies on the master SOM, occur more frequently than other all other nodes, with frequencies of occurrence between 8% and 9% over the course of the 1900–2014 climatology. The fact that these are also the two most persistent nodes in the map likely accounts for these high frequencies; once a highly amplified pattern is in place over Greenland, it tends to remain in place rather than quickly transition to another pattern. As suspected, the edge nodes tend to occur more frequently than those in the interior of the map, with a frequency of occurrence of 2.85% for interior nodes and 4.83% for edge nodes. This is probably due more to the map topology than a meaningful physical

[1] 8.49%	[2] 2.58%	[3] 5.50%	[4] 3.13%	[5] 5.43%	[6] 5.33%
[7] 3.95%	[8] 3.00%	[9] 2.92%	[10] 3.51%	[11] 2.01%	[12] 4.61%
[13] 4.20%	[14] 2.15%	[15] 3.08%	[16] 3.26%	[17] 2.86%	[18] 3.84%
[19] 5.64%	[20] 4.66%	[21] 3.18%	[22] 5.10%	[23] 2.67%	[24] 8.90%

Figure 4.27. Frequency of occurrence of each node during the 1900–2014 climatology. Light blue nodes occur at a rate of 3.00% or less, blue nodes 3.01–6.00%, and dark blue nodes 6.01% or more.

process, a given circulation pattern is more likely to map to an edge node as there are twice as many edge nodes (16) as interior nodes (8).

Changes in the frequency of occurrence of a given node over the period of the climatology were also examined, providing useful information about how Greenland climate has changed over the course of the 20th and early 21st centuries. Plots of node frequency changes for nodes 1–24 is shown in Figure 4.28. Inspecting the time series for the nodes, several interesting trends can be seen. The frequency of nodes 1 and 2 rises sharply after 1920 and 1910, respectively, before dropping sharply around the year 1930. Node 3 also experiences a similar decline in frequency after the late 1920s. Nodes 1–3 are all nodes characterized by both negative temperature and meltwater production

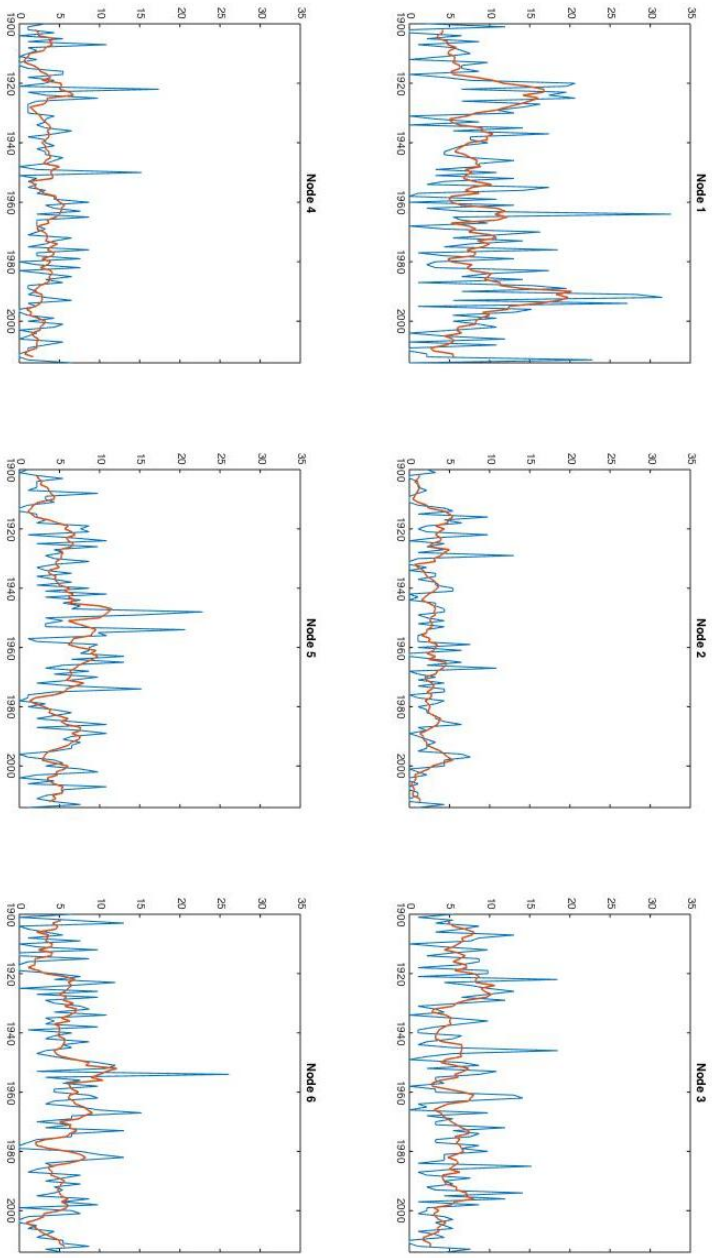

Figure 4.28. Change in the annual frequency of occurrence of each node, 1900–2014. Blue lines are raw data; red lines are a five-year running mean.

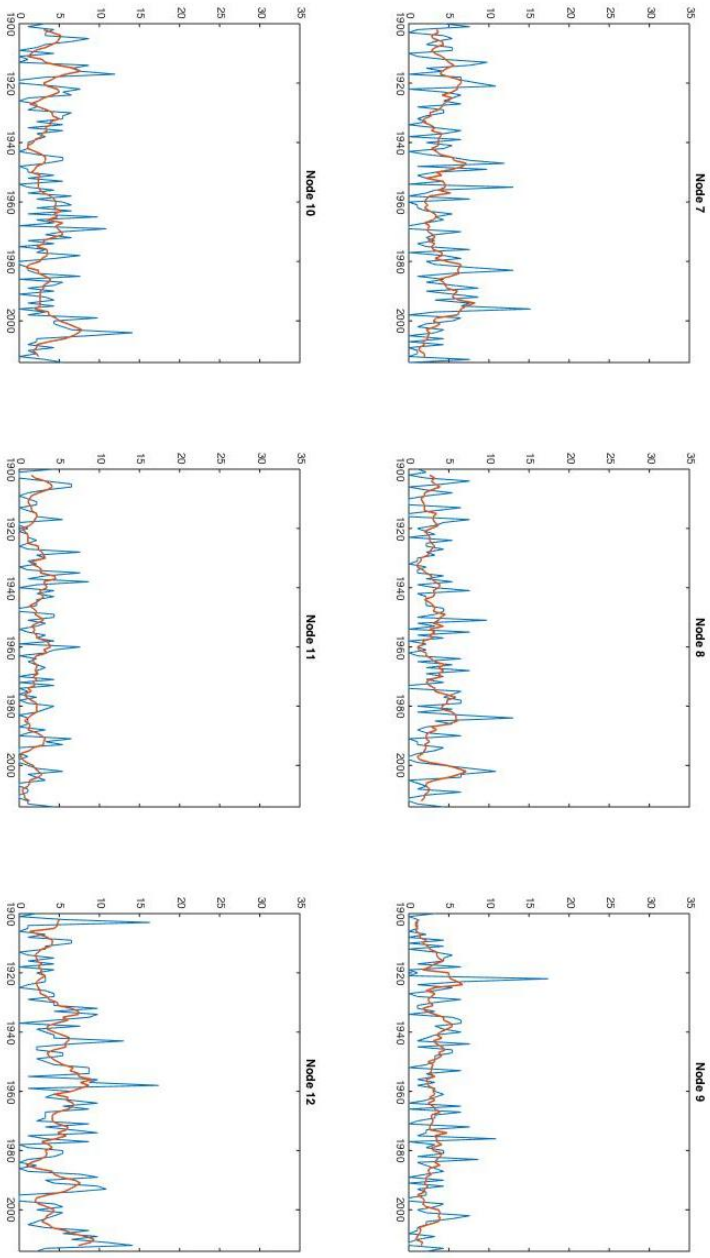

Figure 4.28. Continued.

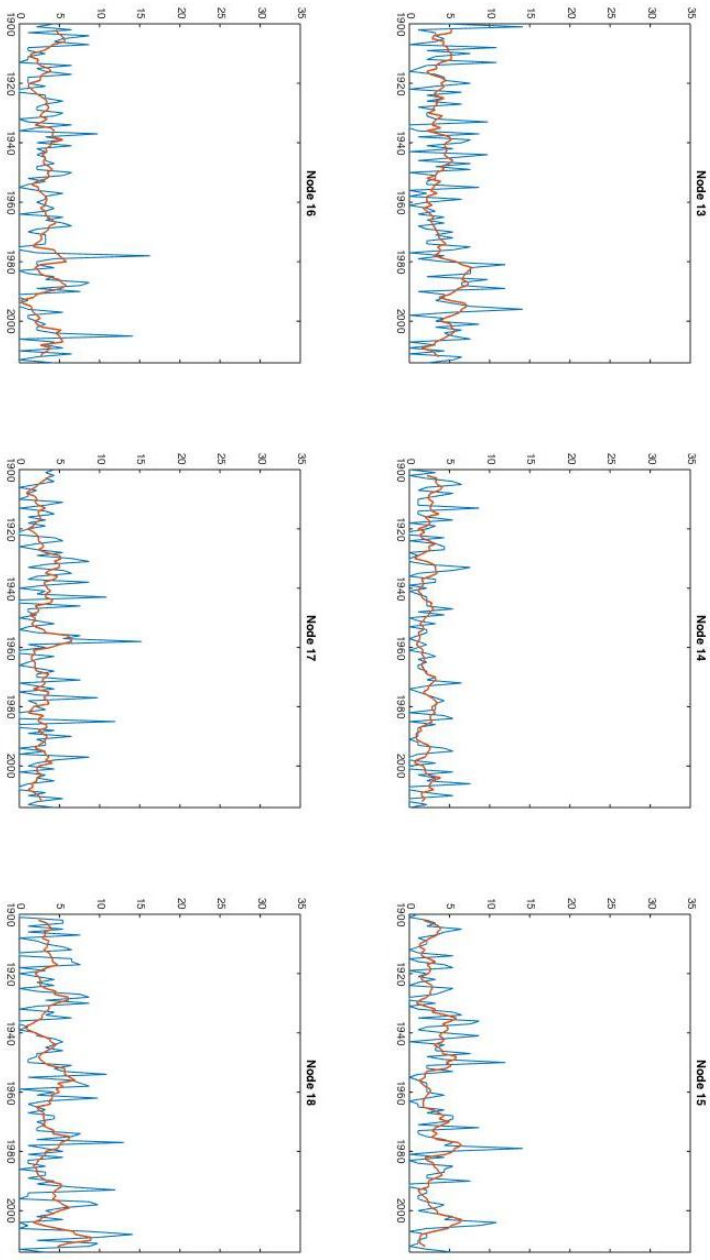

Figure 4.28. Continued.

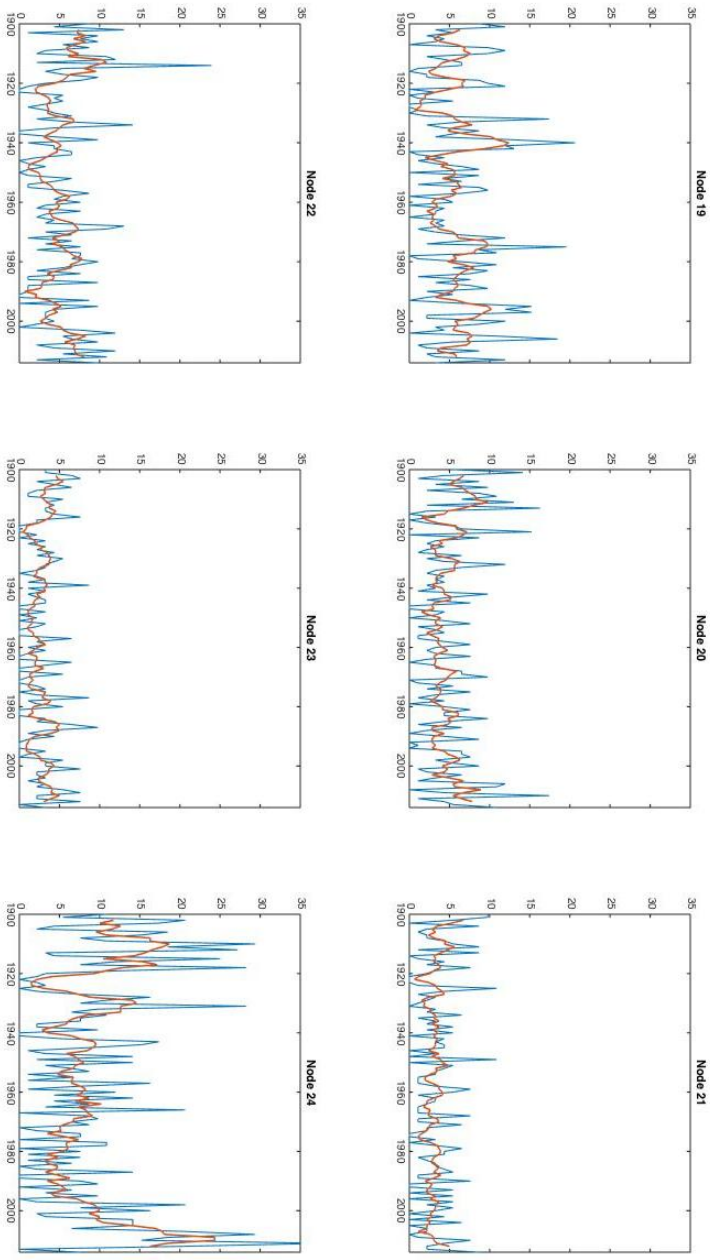

Figure 4.28. Continued.

anomalies; the decline in the frequency of these nodes may be indicative of changing atmospheric circulation patterns associated with the early 20th Century warm period. The frequency of nodes 22 and 24, nodes characterized by positive temperature and positive meltwater production anomalies declines sharply around 1920, near the beginning of a brief cooling period before the sharp increase in temperatures associated with the early 20th Century warm period. In more recent years, the frequency of node 1 rose sharply in the early 1980s, before entering a steep decline from 1990 to 2014. Nodes 2 and 7 also show similar declines in frequency after the year 2000. In contrast, node 24 shows a dramatic increase in frequency during the 21st Century. This pattern of node frequency changes agrees with the increasing temperatures and meltwater production observed during the 21st Century.

The more frequent occurrence of low runoff, high accumulation circulation patterns like nodes 1, 2, and 3 prior to the early 20th Century warm period concurs well with the *Hanna et al.* [2011] surface mass balance reconstruction, which shows higher values of SMB due to low runoff and higher snow accumulation during these years. *Hanna et al.* [2011] also show a reversal in this trend from the mid 1920s to the mid 1930s, as warmer temperatures brought lower values of SMB. This trend is reflected in this work as well, with the rise in frequency of the higher runoff circulation patterns, such as that seen in node 24. In addition, *Hanna et al.* [2016] find a sharp drop in normalized summer GBI values from about 1916–1921 (see Figure 2.5), followed by a sharp rise after the mid-1920s. This rise and fall of GBI are consistent with the results of this analysis, which shows nodes dominated by negative 500 hPa geopotential height

anomalies becoming less frequent as those dominated by positive 500 hPa geopotential height anomalies become more frequent, thus resulting in higher GBI values.

To test the statistical significance of these changes in node frequency, the binomial distribution method of *Cassano et al.* [2007] and *Mioduszewski et al.* [2016] was used. Results of this analysis can be found in Tables 4.2-5. Comparing the 20th Century (1900–2000) node frequencies to the 21st Century (2001–2014) node frequencies, five nodes (1, 2, 3, 6, 7) show statistically significant decreases in frequency, ranging from -2.0% to -3.2%, while node 24 shows a much larger, statistically significant, increase in frequency (+6.5%). The early decades of the 20th Century also show statistically significant changes; comparing the periods 1910–1919 vs. 1920–1929, nodes 1, 5, and 6 show increases in frequency by as much as +9.7% (node 1), while nodes 22 and 24 show decreases in frequency by as much as -12.1% (node 24). These trends reverse when comparing 1920–1929 to 1930–1939, with nodes 1 and 3 decreasing in frequency (-7.5% and -5.1%, respectively) while node 24 increases in frequency (+4.5%). Comparing 1930–1939 to 1940–1949, only node 5 has statistically significant change in frequency, increasing by +4.7%.

4.5.3 Summary

In summary, the node persistence, transition, and frequency change analysis has shown the following:

- Most nodes in the master SOM are transient in nature, with the circulation likely to map to a different node on the following day. Nodes around the edges of the master SOM show higher rates of persistence (circulation

Table 4.2. Changes in node frequency between 1900–2000 and 2000–2014. Statistically significant ($\alpha = 0.05$) frequency changes are in bold.

Node	1	2	3	4	5	6	7	8	9	10	11	12
1900–2000	0.089	0.028	0.058	0.033	0.055	0.056	0.042	0.029	0.030	0.034	0.021	0.045
2001–2014	0.057	0.009	0.033	0.023	0.047	0.036	0.021	0.036	0.023	0.043	0.016	0.057
% Change	**-0.032**	**-0.020**	**-0.026**	-0.010	-0.009	**-0.020**	**-0.021**	0.007	-0.007	0.010	-0.004	0.013

Node	13	14	15	16	17	18	19	20	21	22	23	24
1900–2000	0.042	0.022	0.030	0.032	0.029	0.037	0.056	0.045	0.032	0.049	0.026	0.081
2001–2014	0.041	0.021	0.035	0.037	0.023	0.050	0.060	0.057	0.030	0.064	0.036	0.146
% Change	-0.001	-0.001	0.005	0.005	-0.006	0.013	0.004	0.012	-0.003	0.015	0.010	**0.065**

Table 4.3. Changes in node frequency between 1910–1919 and 1920–1929. Statistically significant ($\alpha = 0.05$) frequency changes are in bold.

Node	1	2	3	4	5	6	7	8	9	10	11	12
1910–1919	0.055	0.035	0.057	0.021	0.027	0.022	0.042	0.025	0.029	0.043	0.016	0.028
1920–1929	0.152	0.041	0.092	0.040	0.060	0.060	0.052	0.026	0.042	0.030	0.017	0.026
% Change	**0.097**	0.007	0.036	0.020	**0.033**	**0.038**	0.010	0.001	0.013	-0.013	0.001	-0.002

Node	13	14	15	16	17	18	19	20	21	22	23	24
1910–1919	0.039	0.025	0.021	0.026	0.025	0.039	0.043	0.051	0.042	0.083	0.036	0.168
1920–1929	0.037	0.020	0.021	0.024	0.023	0.035	0.033	0.050	0.025	0.027	0.018	0.048
% Change	-0.002	-0.005	0.000	-0.002	-0.002	-0.004	-0.011	-0.001	-0.017	**-0.055**	-0.017	**-0.121**

Table 4.4. Changes in node frequency between 1920–1929 and 1930–1939. Statistically significant ($\alpha = 0.05$) frequency changes are in bold.

Node	1	2	3	4	5	6	7	8	9	10	11	12
1920–1929	0.152	0.041	0.092	0.040	0.060	0.060	0.052	0.026	0.042	0.030	0.017	0.026
1930–1939	0.077	0.017	0.041	0.033	0.045	0.058	0.030	0.020	0.035	0.039	0.030	0.055
% Change	**-0.075**	-0.024	**-0.051**	-0.008	-0.015	-0.002	-0.022	-0.007	-0.008	0.009	0.013	0.029

Node	13	14	15	16	17	18	19	20	21	22	23	24
1920–1929	0.037	0.020	0.021	0.024	0.023	0.035	0.033	0.050	0.025	0.027	0.018	0.048
1930–1939	0.036	0.023	0.037	0.038	0.047	0.026	0.063	0.045	0.027	0.052	0.034	0.092
% Change	-0.001	0.003	0.016	0.014	0.024	-0.009	0.030	-0.005	0.002	0.025	0.015	**0.045**

Table 4.5. Changes in node frequency between 1930–1939 and 1940–1949. Statistically significant ($\alpha = 0.05$) frequency changes are in bold.

Node	1	2	3	4	5	6	7	8	9	10	11	12
1930–1939	0.077	0.017	0.041	0.033	0.045	0.058	0.030	0.020	0.035	0.039	0.030	0.055
1940–1949	0.072	0.028	0.048	0.032	0.091	0.051	0.050	0.033	0.039	0.021	0.022	0.049
% Change	-0.005	0.011	0.007	-0.001	**0.047**	-0.007	0.020	0.013	0.004	-0.018	-0.009	-0.007

Node	13	14	15	16	17	18	19	20	21	22	23	24
1930–1939	0.036	0.023	0.037	0.038	0.047	0.026	0.063	0.045	0.027	0.052	0.034	0.092
1940–1949	0.049	0.023	0.042	0.032	0.028	0.033	0.071	0.037	0.036	0.030	0.017	0.067
% Change	0.013	0.000	0.005	-0.007	-0.018	0.007	0.008	-0.008	0.009	-0.022	-0.016	-0.025

maps to same node on the following day); corner nodes generally had the highest persistence of all nodes on the map.

- Edge nodes are most likely to transition to other edge nodes than into the interior of the master SOM; nodes in the interior exhibit a more varied set of transition patterns, while those on the edge tend to be dominated by one or two most frequent patterns. This may be a consequence of map topology, as the interior nodes have more neighbors and hence more possible trajectories.
- Comparing changes in node frequency between 1900–2000 and 2001–2014, statistically significant declines in several negative meltwater production anomaly nodes are seen, with a statistically significant increase in node 24, which has the strongest positive meltwater production anomaly of any node. Examining node frequency changes between 1910–1919 and 1920–1929, statistically significant declines are seen in several positive meltwater production anomaly nodes, with statistically significant

increases in negative meltwater production anomaly nodes. Lastly, this trend reverses when comparing 1920–1929 to 1930–1939, signaling the onset of the early 20th Century warm period.

CHAPTER 5

CONCLUSIONS

This study sought to build on previous synoptic climatological research in Greenland, especially the work of *Belleflamme et al.* [2015] and *Mioduszewski et al.* [2016], by using the 20CRv2c reanalysis, combined with output from regional climate model MAR (forced by 20CRv2c), to examine the linkage between atmospheric circulation and both surface energy balance and surface mass balance during the summer season (JJA) for the period 1900–2014. The self-organizing maps technique was used to identify 24 representative synoptic types, using 500 hPa geopotential height as the variable of interest. For each of the identified types, the effect of the atmospheric circulation on the surface energy balance of the GrIS was examined for both radiative and non-radiative fluxes. The effects of the atmospheric circulation on meltwater production and components of the surface mass balance was also investigated. Additional insight on the temporal evolution of the 500 hPa JJA atmospheric circulation was obtained by examining, for each node, whether the atmospheric circulation is more likely to stay in that particular node for a second consecutive day, or move to another node; the most common transition patterns for each node were also identified. Lastly, changes in the frequency of occurrence of each node during the 1900–2014 study period were examined, and tested for statistical significance.

5.1 Summary of Results

The synoptic climatology of 500 hPa geopotential height anomalies produced in this study depicts the continuum of summer (JJA) mid-tropospheric circulation patterns over Greenland and surrounding offshore waters for the years 1900–2014. The synoptic types depicted for each node range from strong positive 500 hPa geopotential height anomalies, indicative of ridging, to transitional patterns featuring weaker magnitude 500 hPa geopotential height anomalies, to strong negative 500 hPa geopotential height anomalies, indicative of troughing. The 500 hPa geopotential height patterns characteristic of each node correspond strongly, in both magnitude and sign, with anomalies in the mean sea level pressure field.

Examining the 500 hPa wind field, nodes dominated by strong positive 500 hPa geopotential height anomalies are characterized by strong negative zonal wind anomalies across the north Atlantic south of Greenland, with strong positive meridional wind anomalies to the west of Greenland, and strong negative meridional wind anomalies to the east of Greenland. For nodes dominated by strong negative 500 hPa geopotential height anomalies, the opposite pattern is seen, with strong positive zonal wind anomalies across the north Atlantic south of Greenland, strong negative meridional wind anomalies to the west of Greenland, and strong positive meridional wind anomalies to the east of Greenland. These same patterns are also seen closer to the surface, for winds at the $\sigma = 0.995$ model level, although the meridional wind anomalies are much weaker than at the 500 hPa level. The resultant wind 500 hPa wind anomalies reveals the circulation around the troughing and ridging patterns seen in the master SOM.

The surface energy balance revealed that a given circulation pattern can produce very different conditions across the GrIS. While positive (negative) 500 hPa geopotential height anomalies generally lead to negative (positive) cloud cover anomalies, these patterns are not uniform; localized onshore wind, for example, may lead to cloudier skies in one portion of the GrIS while fewer clouds are seen elsewhere. As cloud cover is the main determinant of SWD anomalies, the SWD anomalies seen are also quite variable, but fewer (more) clouds leads to positive (negative) SWD anomalies. Albedo anomalies are also quite spatially heterogeneous, with strong positive anomalies found in areas receiving fresh snowfall, and strong negative anomalies in areas with high meltwater production, likely causing exposure of older snow and/or bare ice, although the strong negative albedo anomalies observed in these nodes may also be due to a downward trend in average JJA GrIS albedo. While SWU anomalies are generally of the same sign as the corresponding SWD anomalies, areas with large albedo changes (such as freshly fallen snow) and weak SWD anomalies can sometimes have SWD and SWU anomalies with opposing signs. LWD anomalies are also quite variable among nodes, with variations in cloud cover and air temperature determining the magnitude of the downward flux. In contrast, LWU anomalies are more spatially homogeneous and are strongly related to surface temperature. Anomalies in net radiation are very weak in most cases, except for coastal areas in nodes with very strong 500 hPa geopotential height anomalies; positive (negative) 500 hPa geopotential height anomalies lead to positive (negative) net radiation anomalies. Both sensible and latent heat flux anomalies are generally opposite in sign to the corresponding 500 hPa geopotential height anomalies over much of the GrIS, but the

magnitudes of the latent heat flux anomalies are generally quite weak compared to the sensible heat flux anomalies.

Turning to the surface mass balance analysis, the spatial heterogeneity seen with the surface energy balance variables produces similarly spatially heterogeneous results with many of the surface mass balance variables. The warmer conditions seen across most of the GrIS in nodes dominated by positive 500 hPa geopotential height anomalies leads to positive meltwater production anomalies, with negative 500 hPa geopotential height anomalies having the opposite effect. While the runoff anomalies have the same sign as the meltwater production anomalies, they are generally weaker in magnitude and confined to regions near the coast, due to meltwater retention and refreezing in the higher elevations of the ablation zone as well as the lower portions of the percolation zone. While refreezing anomalies are generally of the same sign as the meltwater production anomalies, interesting exceptions include portions of the southwestern GrIS. When strong negative geopotential height anomalies are present here, meltwater forming at low elevations that would normally run off or remain liquid refreezes, resulting a positive refreezing anomaly, while at higher elevations, reduced meltwater production results in a negative refreezing anomaly. The signs of the refreezing anomalies are reversed if when strong positive 500 hPa geopotential anomalies are present. Positive 500 hPa geopotential height anomalies have the opposite effect on areas further inland where meltwater would normally refreeze, suggesting that the warmer weather leads to meltwater remaining liquid and/or running off. Strong snowfall anomalies are seen in nodes that depict onshore flow due to an offshore cyclone; the magnitude of the anomaly is likely dependent on the orientation of the onshore flow relative to local topography. Rainfall

anomalies are an order of magnitude weaker than the snowfall anomalies, but the same mechanisms that produce snowfall can lead to rainfall in coastal regions if temperatures are warm enough. Overall, the daily SMB anomalies are fairly weak in magnitude; however, several nodes exhibit localized, strong positive anomalies due to snowfall. Gains or losses in the ice sheet's surface mass are dependent on the frequency of occurrence of each node over the course of the entire summer season.

The analysis of node persistence vs. transience (whether the circulation is more likely to move to another node vs. staying in the same node for a second consecutive day showed that while most nodes are transient, nodes with higher magnitude 500 hPa geopotential height anomalies (nodes 1, 19, 24) are more persistent, with the circulation more likely to stay in the same node for a second consecutive day than move to another node, which may explain their higher frequency of occurrence of these nodes during the period of the climatology. The transition analysis found that as the circulation moves from node to another, a path around the outer edges of the map is most likely.

Examining node frequency changes across the entire climatology, the 500 hPa circulation in the 21st Century (2001–2014) shows an increasing frequency of a pattern with strong positive 500 hPa geopotential height anomalies centered over Greenland (node 24), while three negative 500 hPa geopotential height anomaly patterns decrease in frequency (nodes 1–3). The early 20th Century also shows statistically significant changes in node frequency, with one negative 500 hPa geopotential height anomaly node becoming more frequent (node 1) and two positive 500 hPa geopotential height anomaly nodes (nodes 22 and 24) becoming less frequent during the 1920s than the 1910s. The trend reverses when comparing the 1920s and 1930s, as two negative 500 hPa

geopotential height anomaly nodes (nodes 1 and 3) become less frequent and one positive 500 hPa geopotential height node (node 24) becomes more frequent. The differences between the 1930s and 1940s are minimal, with an increase in one node (node 5) that features positive 500 hPa geopotential height anomalies to the west of Greenland, with negative 500 hPa geopotential height anomalies to the east.

5.2 Results in Context of Prior Research

The significant increase in the frequency of strong positive 500 hPa geopotential height anomalies between the 20th Century and 21st Century found in this study is in line with previous work by *Fettweis et al.* [2011a, 2013], as well as *Mioduszewski et al.* [2016]. Although these prior studies use data only from 1958–2009 *[Fettweis et al.*, 2011a], 1958–2012 [*Fettweis et al.*, 2013] and 1979–2014 [*Mioduszewski et al.*, 2016], all show shifts towards increased frequencies of anticyclonic circulations in the 21st Century compared to the 20th Century. Node 24, which most strongly resembles a high GBI pattern, shows a strong increase in frequency during the 2001–2014 period. This corresponds well with the increasing frequency of extreme "Greenland Blocking Events" found by *McLeod and Mote* [2016] during the early 21st Century, as well as the rising summer values of GBI within the last decade, described by *Hanna et al.* [2016].

The work of *Belleflamme et al.* [2015], which examined the early 20th Century warm period using the 20CRv2 reanalysis, ERA-20C reanalysis and a circulation type classification, found that changes in circulation type frequency could only explain the warm period of 1923-1931 when using SLP data from ERA-20C; no trends in type frequency were seen with SLP data from 20CRv2c, and neither reanalysis produced

significant trends using 500hPa data. These results differ somewhat from the results of this study, which showed significant increases in the frequency of one positive 500 hPa geopotential height anomaly node, and significant decreases in the frequency of two negative 500 hPa geopotential height anomaly nodes, from 1920-1929 to 1930-1939. However, given the differences in the time frames being compared, reanalysis versions (20CRv2 vs. 20CRv2c), study methodologies, and spatial domains, it is somewhat difficult to make a direct comparison. Indeed, different reanalysis products covering the same period can produce very different results; *Fettweis et al.* [in press] found that MAR forced by the 20CRv2c reanalysis showed decreasing GrIS runoff from 1900–1920, with runoff subsequently increasing from 1920–1930; when ERA-20C is used for forcing, runoff increases continuously from 1900 to 1930. While the high levels of variability in the early years of the 20CRv2c may call into question its reliability, especially in sparsely observed regions like the Arctic, useful conclusions can still be drawn from the data, given that this uncertainty is taken into consideration.

The increased frequency of positive 500 hPa geopotential height anomalies during the 1930s and 1940s compared to the 1920s may help explain the warm Greenland temperatures of the 1930s and 1940s described by *Hanna et al.* [2007] and *Box* [2013]. The decreasing temperatures of the 1920s relative to the 1910s, and the sudden increase in temperatures from the 1920s into the 1930s, found by *Hanna et al.* [2011], correspond well with the changing node frequencies in this study, suggesting that the changes in atmospheric circulation may have played some part in the temperature changes. While a broader study, focusing on a larger region of the Arctic and an extended time period (all seasons, instead of summer only) would be needed to investigate this hypothesis further,

the strong correspondence between temperature changes and circulation shifts suggests a causal relationship. An enhanced meridional circulation as a possible contributing factor to the early Arctic warm period has been suggested before; *Wood and Overland* [2010], in their review of early work done on the Arctic warm period, discuss the work of *Pettersson* [1949], who compared the periods 1900–1919 and 1920–1939, and found that "the overall change in the Atlantic-European region is characterized by a development from a high index to a low index" [*Pettersson*, 1949], indicating a shift away from primarily zonal flow towards a more amplified circulation regime with increased meridional flow.

In the present century, a similar shift in meridional circulation may be occurring; *Francis and Vavrus* [2012], in their study of Arctic Amplification, discuss the effects of a reduced latitudinal temperature gradient: a weaker zonal wind and increased Rossby wave amplitude, resulting in slower wave progression and more persistent weather patterns. The results of this study strongly support these conclusions; in comparing the 20th and 21st centuries, this study found a 6.5% increase in frequency for node 24, the strongest positive 500 hPa geopotential height anomaly in the master SOM. This node features the strongest negative zonal wind anomaly of all nodes (Figure 4.4), with meridional wind anomalies that suggest a highly amplified circulation (Figure 4.5). This node is also the most persistent node on the master SOM, as described in Chapter 4. Interestingly, the negative zonal wind anomalies, new maximum latitude of the 5700 m isohypse, and persistent cut-off high over northern Greenland during the 2015 melt season, described by *Tedesco et al*. [2016a], are also suggestive of a possible Arctic Amplification.

If node 24 continues to become more frequent, the ramifications for Greenland surface mass balance are considerable, as this node has the largest positive net radiation anomalies of all, leading to a substantial negative (directed downward) sensible heat flux, resulting in the largest meltwater production anomalies and runoff anomalies of all nodes. Continued increases in meltwater production may be reducing the ability of firn to serve as a buffer against surface mass loss [*Machguth et al.*, 2016].

5.3 Directions for Future Research

While examining 500 hPa geopotential height anomalies for the summer season has yielded much valuable information, including other seasons or all seasons would be a natural starting point for future research. While the clear majority of melt on the GrIS occurs during the summer season (JJA), other seasons have an important role to play as well. *Mattingly et al.* [2016] suggest, based on previous work by *Park et al.* [2015] with Arctic sea ice, that moisture transport into the Arctic during the winter, with accompanying LWD anomalies, may "precondition" the ice sheet for melt once temperatures rise in the spring. Extensive moisture transport into the Arctic during the winter of 2009–2010 may have "preconditioned" the ice sheet for melt, which in combination with the highest GBI values on record for winter (December, January, February or DJF, year of January is the year of winter) and spring (March, April, May or MAM) of 2010 [*Hanna et al.*, 2016], may have helped create the conditions for the second–largest melt extent on record [*Box et al.*, 2011]. In addition, *Box's* [2013] temperature reconstruction shows that the greatest positive temperature anomalies during the early 20th Century warm period (compared to the 1951–1980 base period) were found

during the spring (MAM). Given the marked seasonal differences in Arctic atmospheric circulation, it would be interesting to investigate how the circulation patterns associated with winter, spring, and autumn have changed over the course of the 20th and early 21st centuries, as was done here for summer.

Other possible future directions include separating GrIS mass loss into a thermodynamic, dynamic, and combination term, as done by *Mioduszewski et al.* [2016], that study showed much of the changes in GrIS mass loss (75.0%) were due to thermodynamic rather than dynamic factors. In addition, use of hourly resolution data for turbulent heat fluxes may yield more information; *Mioduszewski et al.* [2016] notes that use of daily resolution data may result in "averaging out" of changes in the sign of the latent heat fluxes in the ablation zone as ice melts and refreezes during a 24-hr period. Variations in temperature during a 24-hr period may result in a similar effect on sensible heat fluxes. Future studies using hourly resolution data would provide additional valuable information about how different atmospheric circulation patterns affect the surface energy balance over the course of a single day.

REFERENCES

Andersen, M. L., L. Stenseng, H. Skourup, W. Colgan, S. A. Khan, S. S. Kristensen, S. B. Andersen, J. E. Box, A. P. Ahlstrøm, and R. Forsberg (2015), Basin-scale partitioning of Greenland ice sheet mass balance components (2007–2011), *Earth Planet. Sci. Lett.*, 409, 89–95, doi:10.1016/j.epsl.2014.10.015.

Bamber, J. L., J. A. Griggs, R. T. W. L. Hurkmans, J. A. Dowdeswell, S. P. Gogineni, I. Howat, J. Mouginot, J. Paden, S. Palmer, E. Rignot, and D. Steinhage (2013), A new bed elevation dataset for Greenland, *Cryosphere*, 7(2), 499–510, doi:10.5194/tc-7-499-2013.

Belleflamme, A., X. Fettweis, and M. Erpicum (2015), Recent summer Arctic atmospheric circulation anomalies in a historical perspective, *Cryosphere*, 9(1), 53–64, doi:10.5194/tc-9-53-2015.

Bengtsson, L., V. A. Semenov, and O. M. Johannessen (2004), The Early Twentieth-Century Warming in the Arctic-A Possible Mechanism, *J. Clim*, 17(20), 4045–4057, doi:10.1175/1520-0442(2004)017%3C4045:TETWIT%3E2.0.CO;2.

Bennartz, R., M. D. Shupe, D. D. Turner, V. P. Walden, K. Steffen, C. J. Cox, M. S. Kulie, N. B. Miller, and C. Pettersen (2013), July 2012 Greenland melt extent enhanced by low-level liquid clouds, *Nature*, 496(7443), 83–86, doi: 10.1038/nature12002.

Bezeau, P., M. Sharp, and G. Gascon (2015), Variability in summer anticyclonic circulation over the Canadian Arctic Archipelago and west Greenland in the late 20th/early 21st centuries and its effect on glacier mass balance, *Int. J. Climatol*, 35(4), 540–557, doi:10.1002/joc.4000.

Box, J. E. (2002), Survey of Greenland instrumental temperature records: 1873–2001, *Int. J. of Climatol.*, 22(15), 1829–1847, doi:10.1002/joc.852.

Box, J. E. (2013), Greenland Ice Sheet Mass Balance Reconstruction. Part II: Surface Mass Balance (1840–2010), *J. Clim.* 26(18), 6974–6989, doi: 10.1175/JCLI-D-12-00518.1.

Box, J. E. and W. Colgan (2013), Greenland ice sheet mass balance reconstruction. Part III: Marine Ice Loss and Total Mass Balance (1840–2010), *J. Clim.*, 26(18), 6990–7002, doi:10.1175/JCLI-D-12-00546.1.

Box, J. E., L. Yang, D. H. Bromwich, and L.S. Bai (2009), Greenland Ice Sheet Surface Air Temperature Variability: 1840–2007, *J. Clim.*, 22(14), 4029–4049, doi:10.1175/2009JCLI2816.1.

Box, J. E., A. Ahlstrøm, J. Cappelen, X. Fettweis, D. Decker, T. Mote, D. van As, R. S. W. van de Wal, and B. Vinther (2011), The Arctic: Greenland, in *State of The Climate 2010*, *Bull. Am. Meteorol. Soc.*, 92(6), S156–S160, doi:10.1175/1520-0477-92.6.S1.

Box, J. E., X. Fettweis, J. C. Stroeve, M. Tedesco, D. K. Hall, and K. Steffen (2012), Greenland ice sheet albedo feedback: thermodynamics and atmospheric drivers, *Cryosphere*, 6(4), 821–829, doi:10.5194/tc-6-821-2012.

Box, J. E., N. Cressie, D. H. Bromwich, J. H. Jung, M. Van Den Broeke, J. H. Van Angelen, R. B. Forster, C. Miège, E. Mosley-Thompson, B. Vinther, and J. R. McConnell (2013), Greenland Ice Sheet Mass Balance Reconstruction. Part I: Net Snow Accumulation (1600–2009), *J. Clim.*, 26(11), 3919–3934, doi:10.1175/jcli-d-12-00373.1.

Brun, E., P. David, M. Sudul, and G. Brunot (1992), A numerical model to simulate snow-cover stratigraphy for operational avalanche forecasting, *J. Glaciol.*, 38(128), 13–22, doi:10.3198/1992JoG38-128-13-22.

Cassano, J. J., P. Uotila, A. H. Lynch, and E. N. Cassano (2007), Predicted changes in synoptic forcing of net precipitation in large Arctic river basins during the 21st century, *J. Geophys. Res.: Biogeosci.*, 112, G04S49, doi:10.1029/2006JG000332.

Chu, V. W. (2014), Greenland ice sheet hydrology: A review, *Prog. Phys. Geog.*, 38(1), 19-54, doi: 10.1177/0309133313507075.

Compo, G. P., J. S. Whitaker, P. D. Sardeshmukh, N. Matsui, R. J. Allan, X. Yin, B. E. Gleason, Jr., R. S. Vose, G. Rutledge, P. Bessemoulin, S. Brönnimann, M. Brunet, R. I. Crouthamel, A. N. Grant, P. Y. Groisman, P. D. Jones, M. C. Kruk, A. C. Kruger, G. J. Marshall, M. Maugeri, H. Y. Mok, Ø. Nordli, T. F. Ross, R. M. Trigo, X. L. Wang, S. D. Woodruff, and S. J. Worley (2011), The Twentieth Century Reanalysis Project, *Q. J. R. Meteorol. Soc.*, 137(654), 1–28, doi:10.1002/qj.776.

Compo, G. P., J. S. Whitaker, P. D. Sardeshmukh, B. Giese, and P. Brohan (2015), Intercomparison of an improved 20th Century reanalysis version “2c” (1851–2007), paper presented at 95th Annual Meeting, Am. Meteorol. Soc., Phoenix, AZ.

Csatho, B. M., A. F. Schenk, C. J. van der Veen, G. Babonis, K. Duncan, S. Rezvanbehbahani, M. R. van den Broeke, S. B. Simonsen, S. Nagarajan, and J. H. van Angelen (2014), Laser altimetry reveals complex pattern of Greenland Ice Sheet dynamics, *Proc. Natl. Acad. Sci. U. S. A.*, 111(52), 8478–18483, doi: 10.1073/pnas.1411680112.

Dee, D. P., S. M. Uppala, A. J. Simmons, P. Berrisford, P. Poli, S. Kobayashi, U. Andrae, M. A. Balmaseda, G. Balsamo, P. Bauer, P. Bechtold, A. C. M. Beljaars, L. van de Berg, J. Bidlot, N. Bormann, C. Delsol, R. Dragani, M. Fuentes, A. J. Geer, L. Haimberger, S. B. Healy, H. Hersbach, E. V. Hólm, L. Isaksen, P. Kållberg, M. Köhler, M. Matricardi, A. P. McNally, B. M. Monge-Sanz, J.-J. Morcrette, B.-K. Park, C. Peubey, P. de Rosnay, C. Tavolato, J.-N. Thépaut, and F. Vitart (2011), The ERA-Interim reanalysis: configuration and performance of the data assimilation system, *Q. J. Roy. Meteorol. Soc.*, 137(656), 553–597, doi:10.1002/qj.828.

De Ridder, K. and H. Gallée (1998), Land Surface-Induced Regional Climate Change in Southern Israel, *J. Appl. Meteorol.*, 37(11), 1470–1485, doi: 10.1175/1520-0450(1998)037<1470:LSIRCC>2.0.CO%3B2.

Enderlin, E. M., I. M. Howat, S. Jeong, M. J. Noh, J. H. van Angelen, and M. R. van den Broeke (2014), An improved mass budget for the Greenland ice sheet, *Geophys. Res. Lett.*, 41(3), 866–872. doi:10.1002/2013GL059010.

Fausto, R. S., D. van As, J. E. Box, W. Colgan, P. L. Langen, and R. H. Mottram (2016), The implication of non-radiative energy fluxes dominating Greenland ice sheet exceptional ablation area surface melt in 2012, *Geophys. Res. Lett.*, 43(6), 2649–2658, doi: 10.1002/2016GL067720.

Fettweis, X. (2007), Reconstruction of the 1979–2006 Greenland ice sheet surface mass balance using the regional climate model MAR, *Cryosphere*, 1(1), 21–40, doi: 10.5194/tc-1-21-2007.

Fettweis, X., G. Mabille, M. Erpicum, S. Nicolay, and M. van den Broeke (2011a), The 1958–2009 Greenland ice sheet surface melt and the mid-tropospheric atmospheric circulation, *Clim. Dyn.*, 36(1), 139–159, doi: 10.1007/s00382-010-0772-8.

Fettweis, X., M. Tedesco, M. van den Broeke, and J. Ettema (2011b), Melting trends over the Greenland ice sheet (1958–2009) from spaceborne microwave data and regional climate models, *Cryosphere*, 5(2), 359–375, doi:10.5194/tc-5-359-2011.

Fettweis, X., E. Hanna, C. Lang, A. Belleflamme, M. Erpicum, M., and H. Gallée (2013), Important role of the mid-tropospheric atmospheric circulation in the recent surface melt increase over the Greenland ice sheet, *Cryosphere*, 7(1), 241–248, doi:10.5194/tc-7-241-2013.

Fettweis, X., J. E. Box, C. Agosta, C. Amory, C. Kittel, and H. Gallée (in press), Reconstructions of the 1900–2015 Greenland ice sheet surface mass balance using the regional climate MAR model, *Cryosphere Discuss.*, 1–32, doi:10.5194/tc-2016-268.

Francis, J. A., and S. J. Vavrus (2012), Evidence linking Arctic amplification to extreme weather in mid-latitudes, *Geophys. Res. Lett.*, 39, L06801, doi:10.1029/2012GL051000.

Gallée, H. and G. Schayes (1994), Development of a Three-Dimensional Meso-γ Primitive Equation Model: Katabatic Winds Simulation in the Area of Terra Nova Bay, Antarctica, *Mon. Weather Rev.*,122(4), 671–685, doi: 10.1175/1520-0493(1994)122<0671:DOATDM>2.0.CO;2.

Hanna, E., P. Huybrechts, I. Janssens, J. Cappelen, K. Steffen, and A. Stephens (2005), Runoff and mass balance of the Greenland ice sheet: 1958–2003, *J. Geophys. Res.: Atmos.*, 110, D13108, doi:10.1029/2004JD005641.

Hanna, E., P. Huybrechts, K. Steffen, J. Cappelen, R. Huff, R., C. Shuman, T. Irvine-Fynn, S. Wise, and M. Griffiths (2007), Increased Runoff from Melt from the Greenland Ice Sheet: A Response to Global Warming, *J. Clim.*, 21(2), 331–341, doi: 10.1175/2007JCLI1964.1.

Hanna, E., P. Huybrechts, J. Cappelen, K. Steffen, R. C. Bales, E. Burgess, J. R. McConnell, J. P. Steffensen, M. van den Broeke, L. Wake, G. Bigg, M. Griffiths, and D. Savas (2011), Greenland Ice Sheet surface mass balance 1870 to 2010 based on Twentieth Century Reanalysis, and links with global climate forcing, *J. Geophys. Res.: Atmos.*, 116, D24121, doi:10.1029/2011JD016387.

Hanna, E., J. M. Jones, J. Cappelen, S. H. Mernild, L. Wood, K. Steffen, and P. Huybrechts (2013), The influence of North Atlantic atmospheric and oceanic forcing effects on 1900–2010 Greenland summer climate and ice melt/runoff, *Int. J. Climatol.*, 33(4), 862–880, doi:10.1002/joc.3475.

Hanna, E., X. Fettweis, S. H. Mernild, J. Cappelen, M. H. Ribergaard, C. A. Shuman, K. Steffen, L. Wood, and T. L. Mote (2014), Atmospheric and oceanic climate forcing of the exceptional Greenland ice sheet surface melt in summer 2012, *Int. J. of Climatol.*, 34(4), 1022–1037, doi: 10.1002/joc.3743.

Hanna, E., T. E. Cropper, R. J. Hall, and J. Cappelen (2016), Greenland Blocking Index 1851–2015: a regional climate change signal, *Int. J. of Climatol.*, 36(15), 4847–4861, doi: 10.1002/joc.4673

Hartmann, D. L. (1994), *Global Physical Climatology*, Academic Press, San Diego, CA.

Hauer, M. E., J. M. Evans, and D. R. Mishra (2016), Millions projected to be at risk from sea-level rise in the continental United States, *Nat. Clim. Chang.*, doi:10.1038/nclimate2961, in press.

Held, I. M., and B. J. Soden (2006), Robust Responses of the Hydrological Cycle to Global Warming, *J. Clim.*, 19(21), 5686–5699, doi: 10.1175/jcli3990.1.

Hewitson, B. C., and R. G. Crane (2002), Self-organizing maps: applications to synoptic climatology, *Clim. Res.*, 22(1), 13–26, doi: 10.3354/cr022013.

Janssens, I., and P. Huybrechts (2000), The treatment of meltwater retention in mass-balance parameterizations of the Greenland ice sheet, *Ann. Glaciol.*, 31(1), 133–140, doi: 10.3189/172756400781819941.

Kalnay, E., M. Kanamitsu, R. Kistler, W. Collins, D. Deaven, L. Gandin, M. Iredell, S. Saha, G. White, J. Woollen, Y. Zhu, M. Chelliah, W. Ebisuzaki, W. Higgins, J. Janowiak, K. C. Mo, C. Ropelewski, J. Wang, A. Leetmaa, R. Reynolds, R. Jenne, and D. Joseph (1996), The NCEP/NCAR 40-Year Reanalysis Project, *Bull. Am. Meteorol. Soc.*, 77, 437–471, doi:10.1175/1520-0477(1996)077<0437:TNYRP>2.0.CO;2.

Khan, S. A., A. Aschwanden, A. A. Bjørk, J. Wahr, K. K. Kjeldsen, and K. H. Kjær (2015), Greenland ice sheet mass balance: a review, *Rep. Prog. Phys.*, 78(4), 046801, doi: 10.1088/0034-4885/78/4/046801.

Kjeldsen, K. K., N. J. Korsgaard, A. A. Bjørk, S. A. Khan, J. E. Box, S. Funder, N. K. Larsen, J. L. Bamber, W. Colgan, M. van den Broeke, M.L. Siggaard-Andersen, C.Nuth, A. Schomacker, C. S. Andresen E. Willerslev, and K. H. Kjær (2015), Spatial and temporal distribution of mass loss from the Greenland Ice Sheet since AD 1900, *Nature*, 528(7582), 396–400, doi:10.1038/nature16183.

Kohonen, T. (2014), *MATLAB Implementations and Applications of the Self-Organizing Map*, Unigrafia Oy, Helsinki.

Lavers, D. A., F. M. Ralph, D. E. Waliser, A. Gershunov and M. D. Dettinger (2015), Climate change intensification of horizontal water vapor transport in CMIP5, *Geophys. Res. Lett.*, 42(13), 5617-5625, doi:10.1002/2015GL064672.

Levia, D. F., and D. J. Leathers (2011), Rain-induced snowmelt, in *Encyclopedia of Snow, Ice and Glaciers*, *Encyclopedia of Earth Sciences Series*, edited by V. P. Singh et al., pp. 915–917, Springer, Dordrecht, The Netherlands, doi: 10.1007/978-90-481-2642-2.

Liu, Y., R. H. Weisberg, and C. N. K. Mooers (2006), Performance evaluation of the self-organizing map for feature extraction, *J. Geophys. Res.: Oceans*, 111, C05018, doi: 10.1029/2005JC003117.

Liu, Y., and R. H. Weisberg (2011), A Review of Self-Organizing Map Applications in Meteorology and Oceanography, in *Self-Organizing Maps - Applications and Novel Algorithm Design*, edited by J. I. Mwasiagi, pp. 253–272, InTech, Rijeka, Croatia, doi: 10.5772/13146.

Machguth, H., M. MacFerrin, D. van As, C. Charalampidis, W. Colgan, R. S. Fausto, H. A. J. Meijer, E. Mosley-Thompson, and R. S. W. van de Wal (2016). Greenland meltwater storage in firn limited by near-surface ice formation, *Nat. Clim. Chang.*, 6(4), 390–393, doi:10.1038/nclimate2899

Mattingly, K. S., C. A. Ramseyer, J. J. Rosen, T. L. Mote, and R. Muthyala (2016), Increasing water vapor transport to the Greenland Ice Sheet revealed using self-organizing maps, *Geophys. Res. Lett.,* 43(17), 9250–9258, doi:10.1002/2016GL070424.

McLeod, J. T., and T. L Mote (2015), Assessing the role of precursor cyclones on the formation of extreme Greenland blocking episodes and their impact on summer melting across the Greenland ice sheet, *J. Geophys. Res.: Atmos.*, 120(24), 12357–12377, doi:10.1002/2015JD023945.

McLeod, J. T. and T. L. Mote (2016), Linking interannual variability in extreme Greenland blocking episodes to the recent increase in summer melting across the Greenland ice sheet, *Int. J. Climatol.*, 36(3), 1484–1499, doi:10.1002/joc.4440.

Mernild, S. H., T. L. Mote, and G. E. Liston (2011), Greenland ice sheet surface melt extent and trends: 1960–2010, *J. Glaciol.*, 57(204), 621–628, doi: 10.3189/002214311797409712.

Mernild, S. H., E. Hanna, J. C. Yde, J. Cappelen, J., and J. K. Malmros (2014), Coastal Greenland air temperature extremes and trends 1890–2010: annual and monthly analysis, *Int. J. Climatol.*, 34(5), 1472–1487, doi: 10.1002/joc.3777.

Mioduszewski, J. R., Å. K. Rennermalm, A. Hammann, M. Tedesco, E. U. Noble, J. C. Stroeve, *and* T. L. Mote *(2016),* Atmospheric drivers of Greenland surface melt revealed by self-organizing maps, *J. Geophys. Res.: Atmos.,* 121(10), 5095–5114*, doi: 10.1002/2015JD024550.*

Mortin, J., G. Svensson, R. G. Graversen, M.-L. Kapsch, J. C. Stroeve, and L. N. Boisvert (2016), Melt onset over Arctic sea ice controlled by atmospheric moisture transport, *, Geophys. Res. Lett., 43(12), 6636-6642, doi: 10.1002/2016GL069330.*

Mote, T. L. (1998a), Mid-tropospheric circulation and surface melt on the Greenland Ice Sheet. Part I: Atmospheric Teleconnections, *Int. J. Climatol.*, 18(2), 111–129, doi: 10.1002/(SICI)1097-0088(199802)18:2<111::AID-JOC227>3.0.CO;2-X.

Mote, T. L. (1998b), Mid-tropospheric circulation and surface melt on the Greenland Ice Sheet. Part II: Synoptic Climatology, *Int. J. Climatol.*, 18(2), 131–145, doi: 10.1002/(SICI)1097-0088(199802)18:2<131::AID-JOC228>3.0.CO;2-S.

Mote, T. L. (2007), Greenland surface melt trends 1973–2007: Evidence of a large increase in 2007, *Geophys. Res. Lett.*, 34(22), L22507, doi:10.1029/ 2007GL03197.

Neff, W., G. P. Compo, F. M. Ralph, and M. D. Shupe (2014), Continental heat anomalies and the extreme melting of the Greenland ice surface in 2012 and 1889, *J. Geophys. Res.: Atmos.*, 119(11), 6520–6536, doi: 10.1002/2014JD021470.

Nghiem, S. V., D. K. Hall, T. L. Mote, M. Tedesco, M. R. Albert, K. Keegan, C. A. Shuman, N. E. DiGirolamo, and G. Neumann (2012), The extreme melt across the Greenland ice sheet in 2012, *Geophys. Res. Lett.*, 39(20), L20502, doi:10.1029/ 2012GL053611.

Oke, T. R. (1987), *Boundary Layer Climates*, Routledge, London.

Park, H.-S., S. Lee, Y. Kosaka, S.-W. Son, and S.-W. Kim (2015), The Impact of Arctic Winter Infrared Radiation on Early Summer Sea Ice, *J. Clim.*, 28(15), 6281–6296, doi:10.1175/JCLI-D-14-00773.1.

Petterssen, S. (1949), Changes in the general circulation associated with the recent climatic variation, *Geogr. Ann.*, 31, 212–221, doi:10.2307/520365.

Poli P., H. Hersbach, D. P. Dee, P. Berrisford, A. J. Simmons, F. Vitart, P. Laloyaux, D. G. H. Tan, C. Peubey, J.-N. Thépaut, Y. Trémolet, E. V. Hólm, M. Bonavita, L. Isaksen, M. Fisher (2016), ERA-20C: An Atmospheric Reanalysis of the Twentieth Century, *J. Clim*., 29(11), 4083–4097, doi: 10.1175/JCLI-D-15-0556.1.

Rennermalm, Å. K., S. E. Moustafa, J. Mioduszewski, V. W. Chu, R. R. Forster, B. Hagedorn, J. T. Harper, T. L. Mote, D. A. Robinson, C. A. Shuman, L. C. Smith, and M. Tedesco (2013), Understanding Greenland ice sheet hydrology using an integrated multi-scale approach, Environmental Research Letters, 8(1), 015017, doi: 10.1088/1748-9326/8/1/015017.

Reusch, D. B., R. B. Alley, and B. C. Hewitson (2005), Relative performance of self-organizing maps and principal component analysis in pattern extraction from synthetic climatological data, *Polar Geogr.*, 29(3), 188–212, doi: 10.1080/789610199.

Rienecker M. M., M. J. Suarez, R. Gelaro, R. Todling, J. Bacmeister, E. Liu, M. G. Bosilovich, S. D. Schubert, L. Takacs, G.-K.Kim, S. Bloom, J. Chen, D. Collins, A. Conaty, A. Da Silva, W. Gu, J. Joiner, R. D. Koster, R. Lucchesi, A. Molod, T. Owens, S. Pawson, P. Pegion, C. R. Redder, R. Reichle, F. R. Robertson, A. G. Ruddick, M. Sienkiewicz, and J. Woollen (2011), MERRA: NASA's Modern-Era Retrospective Analysis for Research and Applications, *J. Clim.*, 24(14), 3624–3648, doi: 10.1175/JCLI-D-11-00015.1.

Rignot, E., I. Velicogna, M. R. van den Broeke, A. Monaghan, and J. T. M. Lenaerts, (2011), Acceleration of the contribution of the Greenland and Antarctic ice sheets to sea level rise, *Geophys. Res. Lett.*, 38(5), L05503, doi:10.1029/2011GL046583.

Schuenemann, K. C., and J. J Cassano (2009), Changes in synoptic weather patterns and Greenland precipitation in the 20th and 21st centuries: 1. Evaluation of late 20th century simulations from IPCC models, *J. Geophys. Res.: Atmos.*, 114(D20), D20113, doi: 10.1029/2009JD011705.

Schuenemann, K. C., and J. J. Cassano (2010), Changes in synoptic weather patterns and Greenland precipitation in the 20th and 21st centuries: 2. Analysis of 21st century atmospheric changes using self-organizing maps, *J. Geophys. Res.: Atmos.*, 115(D5), D05108, doi: 10.1029/2009JD011706.

Schuenemann, K. C., J. J. Cassano, and J. Finnis (2009), Synoptic Forcing of Precipitation over Greenland: Climatology for 1961-99, *J. of Hydrometeorol.*, 10(1), 60–78, doi: 10.1175/2008JHM1014.1.

Serreze, M. C. and R. G. Barry (2014), *The Arctic Climate System*, *Cambridge Atmospheric and Space Science Series*, Cambridge University Press, New York.

Shepherd, A., E. R. Ivins, G. A, V. R. Barletta, M. J. Bentley, S. Bettadpur, K. H. Briggs, D. H. Bromwich, R. Forsberg, N. Galin, M. Horwath, S. Jacobs, I. Joughin, M. A. King, J. T. M. Lenaerts, J Li, S. R. M. Ligtenberg, A. Luckman, S. B. Luthcke, M. McMillan, R. Meister, G. Milne, J. Mouginot, A. Muir, J. P. Nicolas, J. Paden, A. J. Payne, H. Pritchard, E. Rignot, H. Rott, L. S. Sørensen, T. A. Scambos, B. Scheuchl, E. J. O. Schrama, B. Smith, A. V. Sundal, J. H. van Angelen, W. J. van de Berg, M. R. van den Broeke, D. G. Vaughan, I. Velicogna, J. Wahr, P. L. Whitehouse, D. J. Wingham, D. Yi, D. Young, and H. J. Zwally (2012), A reconciled estimate of ice-sheet mass balance, *Science*, 338(6111), 1183–1189, doi: 10.1126/science.1228102.

Sheridan, S. C., and C. C. Lee (2011), The self-organizing map in synoptic climatological research, *Prog. Phys. Geog.*, 35(1), 109–119, doi: 10.1177/0309133310397582.

Skific, N., and J. Francis (2012), Self-Organizing Maps: A Powerful Tool for the Atmospheric Sciences, in *Applications of Self-Organizing Maps*, edited by M. Johnsson, pp. 251–268, InTech, Rijeka, Croatia, doi:10.5772/54299.

Skific, N., J. A. Francis, and J. J. Cassano (2009), Attribution of Projected Changes in Atmospheric Moisture Transport in the Arctic: A Self-Organizing Map Perspective, *J. Clim.*, *22*(15), 4135–4153, doi: 10.1175/2009JCLI2645.1.

Tedesco, M., X. Fettweis, T. Mote, J. Wahr, P. Alexander, J. Box, and B. Wouters, (2013), Evidence and analysis of 2012 Greenland records from spaceborne observations, a regional climate model and reanalysis data, *Cryosphere*, 7(2), 615–630, doi:10.5194/tc-7-615-2013.

Tedesco, M., T. Mote, X. Fettweis, E. Hanna, J. Jeyaratnam, J.F. Booth, R. Datta and K. Briggs (2016a), Arctic cut-off high drives the poleward shift of a new Greenland melting record, *Nat. Commun.*, 7, 11723, doi: 10.1038/ncomms11723.

Tedesco, M., J. E. Box, J. Cappelen, X. Fettweis, K. Hansen, T. Mote, C. J. P. P. Smeets, D. van As, R. S. W. van de Wal, I. Velicogna, and J. Wahr (2016b), The Arctic: Greenland Ice Sheet, in *State of The Climate 2015*, *Bull. Am. Meteorol. Soc.*, 97(8), S140–S142, doi: 10.1175/2016BAMSStateoftheClimate.1

Uppala, S. M., P. W. Kållberg, A. J. Simmons, U. Andrae, V. Da Costa Bechtold, M. Fiorino, J. K. Gibson, J. Haseler, A. Hernandez, G. A. Kelly, X. Li, K. Onogi, S. Saarinen, N. Sokka, R. P. Allan, E. Andersson, K. Arpe, M. A. Balmaseda, A. C. M. Beljaara, L. van de Berg, J. Bidlot, N. Bormann, S. Caires, F. Chevallier, A. Dethof, M. Dragosavac, M. Fisher, M. Fuentes, S. Hagemann, E. Hólm, B. J. Hoskins, L. Isaksen, P. A. E. M. Janssen, R. Jenne, A. P. McNally, J.-F. Mahfouf, J.-J. Morcrette, N. A. Rayner, R. W. Saunders, P. Simon, A. Sterl, K. E. Trenberth, A. Untch, D. Vasiljevic, P. Viterbo, and J. Woollen (2005), The ERA-40 re-analysis, *Q.J.R. Meteorol. Soc.*, 131(612), 2961–3012, doi:10.1256/qj.04.176.

van den Broeke, M., J. Bamber, J. Ettema, E. Rignot, E. Schrama, W. J. van de Berg, E. van Meijgaard, I. Velicogna, and B. Wouters (2009), Partitioning Recent Greenland Mass Loss, *Science*, 326(5955), 984–986, doi: 10.1126/science.1178176.

van den Broeke, M. R., E. M. Enderlin, I. M. Howat, and B. P. Noël (2016), On the recent contribution of the Greenland ice sheet to sea level change, *Cryosphere*, 10(5), 1933–1946, doi: 10.5194/tc-10-1933-2016.

Vatanen, T., M. Osmala, T. Raiko, K. Lagus, M. Sysi-Aho, M. Orešič, T. Honkela, and H. Lähdesmäki (2015), Self-organization and missing values in SOM and GTM, *Neurocomputing*, 147, 60–70, doi: 10.1016/j.neucom.2014.02.061.

Vernon, C. L., J. L. Bamber, J. E. Box, M. R. van den Broeke, X. Fettweis, E. Hanna, and P. Huybrechts (2013), Surface mass balance model intercomparison for the Greenland ice sheet, *Cryosphere*, 7(2), 599–614, doi: 10.5194/tc-7-599-2013.

Vesanto, J., J. Himberg, E. Alhoniemi, and J. Parhankangas (2000), SOM Toolbox for Matlab 5, *Rep. A57*, Helsinki University of Technology, Espoo, Finland.

Wood, K. R., and J. E. Overland (2010), Early 20th century Arctic warming in retrospect, *Int. J. Climatol.*, 30(9), 1269–1279, doi:10.1002/joc.1973.

Yarnal, B. (1993), *Synoptic climatology in environmental analysis: A primer*, Belhaven Press, London.

Zwally, H. J., W. Abdalati, T. Herring, K. Larson, J. Saba, and K. Steffen (2002), Surface Melt-Induced Acceleration of Greenland Ice-Sheet Flow, *Science*, 297(5579), 218–222, doi: 10.1126/science.1072708.